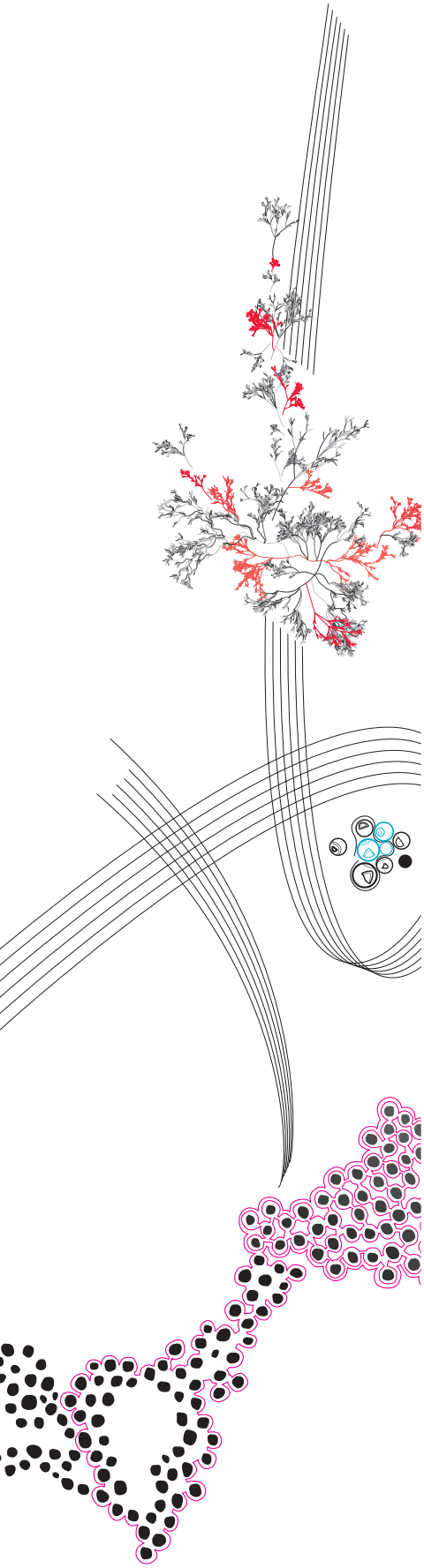

Optical Coherence Tomography for Capturing the Characteristics of a Melt Pool in Laser Cladding

University of Twente
Mechanical Engineering
Chair of Laser Processing

Author
J.R.M. Tiemessen

Date
16-12-2024

Graduation committee
Chairman - Prof.dr.ir. G.R.B.E. Römer
Supervisor - Dr.ir. H. Mustafa
External member - Dr. D.T.A. Matthews

Preface

This report presents the findings of my MSc thesis project, conducted within the Chair of Laser Processing at the University of Twente. The research involved testing and analysis of an Optical Coherence Tomography system that has been integrated into a laser cladding setup.

I extend my gratitude to my supervisor, Dr. ir. Hasib Mustafa, for his valuable insights, assistance with the experimental setup, and overall very supportive guidance. I also wish to thank Prof. dr. ir. Gert-Willem Römer and M.L. Stok - van Houwelingen for their contributions.

Joris Tiemessen
December 2024

List of Abbreviations

Nd:YAG	Neodymium-doped Yttrium Aluminum Garnet
Yb:YAG	Ytterbium-doped Yttrium Aluminum Garnet
NLPM	Normal Liters per Minute
SLED	Superluminescent Light Emitting Diode
OCT	Optical Coherence Tomography
ICI	Inline Coherence Interferometry
LMD	Laser Material Deposition
LMD-w	Laser Material Deposition with co-axial wire feeding
L-PBF	Laser Powder Bed Fusion
SLM	Selective Laser Melting
FD-OCT	Fourier-Domain Optical Coherence Tomography
SD-OCT	Spectral-Domain Optical Coherence Tomography
SS-OCT	Swept-Source Optical Coherence Tomography
TIG	Tungsten Inert Gas (welding)
PTA	Plasma-Transferred Arc (welding)
SLD	Superluminescent Diode
TCP	Tool Center Point
BPP	Beam Parameter Product
SOR	Statistical Outlier Removal
ROR	Radius Outlier Removal
SNR	Signal to Noise Ratio
RMSE	Root Mean Square Error
HAZ	Heat-Affected Zone
RGB	Red, Green, Blue

Nomenclature

P	Laser power [W]
v_c	Cladding speed [mm/s]
$\dot{m}$	Powder feed rate [g/min]
d_C	Dilution ratio of clad [-]
η	Powder efficiency [%]
λ	Wavelength [nm]
$\Delta\lambda$	Spectral bandwidth [nm]
k	Wavenumber [1/m]
Δk	Spectral bandwidth [1/m]
k_0	Central wavenumber of spectrum [1/m]
l_c	Coherence length [m^2]
θ	Beam divergence [radians]
M^2	Beam quality factor [-]
g	Gravity field [m/s^2]
A_1	Area of the clad layer above the substrate [m^2]
A_2	Mixing area of the substrate and clad [m^2]
θ'	Root angle of clad [°]
ζ	Aspect ratio [-]
W_c	Clad track width [mm]
h_c	Clad track height [mm]
$wt.\%$	Weight percent [%]
T	Temperature [K]
ρ	Density [kg/m^3]
c_p	Thermal capacity [$J/kg \cdot K$]
K	Thermal conductivity [$W/m \cdot K$]
Q	Heat sources and sinks in the material [W/m^3]
U	Cladding speed vector [m/s]
μ	Viscosity [$kg/s \cdot m$]
n	Normal vector of the surface [-]
h_c	Heat convection coefficient [$W/(m^2 \cdot K)$]
Ω	Workpiece surfaces [m^2]
Γ	Surface area irradiated by the laser beam [m^2]
T_0	Ambient temperature [K]
z_{Sn}	Depth of reflection 'Sn' within sample [m]
R_{Sn}	Reflectivity of reflection 'Sn' [-]
z_R	Position of the reference arm mirror [m]
R_R	Reflectivity of the reference arm mirror [-]
$I_D(k)$	Detector current as a function of wavenumber [-]
ρ_d	Responsivity [A/W]
$S(k)$	Optical power density as a function of wavenumber [-]
γ	Coherence function [-]
G	Thermal gradient at the solidification front [K/cm]
R	Solidification rate [cm/s]

Abstract

Laser cladding is a laser material process in which powder is injected into a focused laser beam using an inert gas, forming a deposit referred to as a clad track. When cladded tracks are laid down next to each other, they form a continuous coating on a substrate material. The size and morphology of the solidified microstructure of the cladded tracks are closely linked to the size and shape of the laser-induced melt pool during the process.

In this research, an Optical Coherence Tomography (OCT) system is introduced to a laser cladding setup to investigate its ability to capture the geometrical characteristics of the melt pool. OCT is a non-invasive measurement technique that utilizes low-coherence light to create interference patterns. The interference pattern is used to obtain depth-resolved images. The effectiveness of the OCT sensor, both ex-situ and in-situ, was evaluated by benchmarking it against confocal microscopy and thermal imagery, respectively.

From the ex-situ findings, it was observed that the OCT system exhibits reduced performance on steep edges due to the large spot size of the OCT measurement beam relative to the geometry that is captured. Most importantly, the study revealed that in-situ OCT measurements highlight different zones with a distinct boundary, which is suggested to represent the liquid-solid phase transition from the melt pool to the solidified track.

Contents

1 Introduction

1.1 Background

Laser Cladding

Coatings play a crucial role in enhancing the durability and properties of materials. This is achieved by adding a small layer on top of a substrate material. Coatings in the form of a steel alloy, including elements like carbon, chromium and tungsten, are specifically applied to components to improve material properties, such as toughness, strength and resistance to corrosion and wear [1]. This effectively extends the lifespan of these components. Coatings are a widely adopted strategy where numerous application techniques have emerged, such as thermal spraying, electroplating, and chemical vapor deposition [2]. Around the 1970's, techniques such as tungsten inert gas (TIG) welding and plasma-transferred arc (PTA) welding were utilized for coating applications [3]. However, these methods were constrained by significant challenges, including high dilution of the substrate into the coating and distortions due to the high heat input. The use of lasers, introduced only a few years earlier, was thought to be solution to aforementioned problem. In 1974, the concept of laser cladding was patented [4]. Laser cladding (with powder feed) is a process where powder is fed into a laser beam, melting (part of) the substrate and the powder to form a coating on the substrate, as depicted in figure 1. This new technique offered several distinct advantages: reduced dilution of the substrate in to the coating and a decreased total heat input. Additionally, the process allowed for very precise deposition together with real-time process control. Other material feeding techniques, either using pre-placed powder beds or wire feeding were developed as well [5, 6].

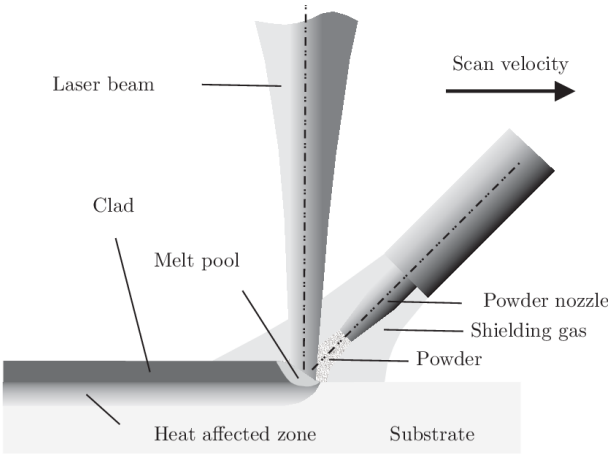

Figure 1: Schematic overview of an off-axis powder supply laser cladding setup [7]

The foundations of the industrially applied laser cladding process were established [8] in the 1980's. The use of CO_2 lasers was a big step towards wider utilization in industrial environments as the available laser power enabled the application of coatings on larger areas in one single process step [9]. At the same time, a lot of different materials were tested for their potential to be used in a laser cladding process [10].

Over time, various laser sources have been integrated into the laser cladding process, as soon as the power and efficiency of different commercially used laser types was large enough [6]. Today, Yb:YAG fiber lasers and disk lasers, both solid-state lasers, are the most used laser sources for laser cladding applications [11,12]. Simultaneous to the development and introduction of different laser sources in to the laser cladding process, the development of optical heads, equipment for powder supply and process control gained momentum as well [3, 13]. Advancements in the hardware components and the increased cost-effectiveness [14] as well as strategies for decreased processing times [15] have yielded more applications of the laser cladding process.

Optical Coherence Tomography

Back in the 1970's a concept that would later be referred to as Optical Coherence Tomography (OCT) was beginning to take shape as an innovative imaging technique that would be able to produce an optical 'biopsy' [16]. The ability to retrieve depth-resolved images in a non-invasive manner was proven to have great potential in ophthalmology, where it was shown that the imaging technique was capable of visualizing various retinal diseases [17]. The working principle of the technique has similarities with ultrasound imaging, which uses returning sound waves to visualize internal structures. OCT utilizes reflected light of a sample measured by a Michelson interferometer, which relies on the interference between the reflected light beam and a reference light beam, to obtain a depth-resolved image [18]. OCT systems at this point were later all recognized as Time Domain OCT (TD-OCT) systems.

It was only in 1995 when Fourier Domain OCT was first presented, in the works of Fercher et al. [19]. In this work, a spectrometer was used to capture the wavelength dependent interference. It was found that this new strategy was capable of acquiring depth-resolved images at incredibly greater speeds than TD-OCT systems. As the system made use of a spectrometer, this system was categorized as Spectral Domain OCT (SD-OCT). Two years later, the research group of Chinn et al. introduced a different Fourier Domain OCT technique, that is now known as Swept Source OCT (SS-OCT) [20]. Both Fourier Domain techniques are still in use and continue to undergo advancements [21].

Ophthalmology has been the primary field for OCT's development, driving significant improvements in technology. Only recently, OCT has also made its introduction into laser material processing, where it has been repeatedly showcased in laser welding processes [22].

1.2 Problem Definition

Laser cladding with a powder feed involves depositing single or consecutive tracks to form a coating by introducing powder into a laser beam that strikes a substrate. It is a process in which the existence and dynamic behaviour of a melt pool is inherent. The dynamics of this melt pool are highly complex. For example, momentum is added due to the powder feed and there are fluid flows existent within the melt pool because of the surface tension gradient [23]. Also, a solidification process occurs within the process. Ultimately, the size and shape of the melt pool are critical determinants of the final microstructure of the cladded track.

While thermal cameras [24] and high-speed cameras [25] have previously been used to measure the melt pool's temperature and size, a different method is needed to capture its geometry. Accurately capturing the melt pool's geometry is essential because, once measurable, it becomes possible to control it. This control can manifest in adjusting process parameters of the laser cladding process while processing, according to the needs of manufacturing. This can lead to an improved process with reduced deformations and inaccuracies, resulting in a more reliable and consistent laser cladding process.

This research studies the integration of an OCT system into the laser cladding setup to assess its ability to measure the melt pool's geometry. Prior to implementation in experiments where a melt pool is existent, the OCT system undergoes an evaluation in terms of its measurement accuracy when capturing the clad track's geometry after processing. This is done by comparison to an established surface profiling technique. That is, confocal microscopy. For experiments carried out during processing, it will be researched how the OCT system responds to the influence of an intersecting powder stream and shielding gas. Ultimately, by benchmarking OCT's ability to capture the melt pool against thermal imagery, the study aims to finally determine the effectiveness of OCT in terms of its potential as a tool for capturing and monitoring the geometry of a melt pool in a laser cladding setup.

1.3 Research Objectives

The research in this thesis will focus on the following areas, phrased as questions:

1. Given that the OCT sensor is integrated into the laser cladding environment, what is the optimal strategy for measurement and analysis to characterize the system?
2. How is the performance of the OCT system characterized in a laser cladding environment when process parameters are varied, leading to changes in clad track dimensions?
3. How effective is the OCT sensor in capturing the geometric characteristics of the melt pool formed during laser cladding?

1.4 Thesis Structure

In the first chapter, the report introduces the research topic, defines the problem, and sets the research objectives. It outlines the motivation, challenges in laser cladding, and goals for integrating and evaluating an OCT system.

In the second chapter, the state of the art is reviewed. This chapter includes the fundamentals of laser cladding, the working principles of OCT, and its application in other laser processes, highlighting its performance and limitations.

In the third chapter, the experimental setup and methodology are detailed. This chapter covers the integration of the OCT sensor into the laser cladding system, the measurement process, and how data is captured, processed, and analyzed.

In the fourth chapter, the experimental results are analyzed, distinguishing between measurements taken after the cladding process (ex-situ) and those taken during processing (in-situ). The results are compared against confocal microscopy and thermal imagery to evaluate their effectiveness, respectively.

In the fifth chapter, a discussion of the results is posed where the focus will be on connecting the outcomes from the different experiments to illustrate their interrelations and overall contributions to the research.

In the sixth chapter, the report concludes with key findings and recommendations. It answers the research questions posed in the first chapter and it summarizes the conclusions drawn from the results. It suggests improvements and areas for future research.

2 State-of-the-Art

2.1 Fundamentals of Laser Cladding

Laser cladding refers to the deposit of a desired material on a substrate material by means of a laser. This is the case when applying coatings, where a material or metal with enhanced properties is added as a layer on top of a substrate that is often a cheaper bulk material with less desirable characteristics. This process protects the substrate and extends its lifespan. A similar deposition approach, still referred to as laser cladding, is also used in additive manufacturing [26]. The process involves introducing the desired material into a melt pool induced by the laser beam, which melts the material to form a deposit referred to as a clad or cladded track. The laser creates a melt pool on the substrate material, into which the supplied material is simultaneously introduced. While the material may absorb some radiation as it travels to the melt pool, the actual melting occurs within the melt pool [27]. Because part of the substrate material also melts, solidification results in a metallurgical bond between the deposit and the substrate. The use of the laser allows for precise deposition of the cladded track where the surrounding material is almost not affected. This is referred to as a small heat-affected zone (HAZ). The material can be supplied in either the form of powder or in the form of a wire. When using powder, there are different configurations that can be used. One approach is the use of a pre-placed powder bed. Another, is referred to as powder injection or co-deposition. The latter can be implemented using different methods, such as an off-axial (lateral or leading) powder feed or a coaxial powder feed. The coaxial powder feed system offers the advantage of enabling greater maneuverability in all directions [28].

2.1.1 Clad Track Characteristics

The cladded track that is deposited in a laser cladding process, possesses distinct characteristics, as shown in figure 2. This section introduces these characteristics and how these are subject to the main processing parameters of laser cladding.

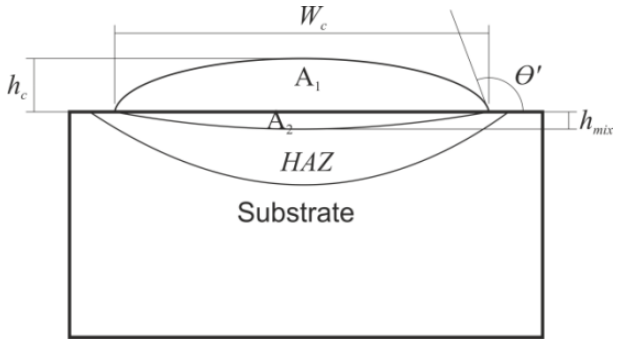

Figure 2: Schematic diagram of a cross-section of a cladded track [29]. W_c and h_c represent the width and height of the track respectively. A_1 represents the area of the clad layer above the substrate. A_2 represents the mixing area. The root angle of the clad track and heat affected zone are represented as θ' and HAZ respectively.

The aspect ratio, ζ assesses the horizontal dimension of the deposited clad W_c in relation to its height h_c [30]. A higher ζ is achieved with increasing width of the cladded track and with decreasing height of the cladded track, and vice versa. The aspect ratio is defined in equation 1.

$$\zeta = W_c/h_c \tag{1}$$

Another characteristic of the cladded track, is its approximated dilution level d_c [31]. That is, a measure for the level of dilution of the cladded track by the substrate material. It is calculated by the ratio of the cross-sectional area of the cladded track above the substrate level and the total cross-sectional area of what has previously been molten, as shown in equation 2.

$$d_C = A_2/(A_1 + A_2) \tag{2}$$

It is strived for to minimize the dilution level as to obtain a surface layer with minimal dilution by the substrate material. However, a too low dilution level carries the risk of insufficient bonding between the cladded track and the substrate material. Hence, a dilution range of 2% to 8% is deemed favorable [7]. The size of the areas that are considered for the approximated dilution level are dependent on the height and width of the cladded track. Hence, the aspect ratio is typically a good indicator of the dilution level as well. A lower aspect ratio typically yields a lower dilution level. The specific dilution level is e.g. dependent on the laser power, the scan speed and the intensity distribution of the laser as these all have an effect on the width and height and subsequently the different areas that are used for calculating the level of dilution.

As seen in figure 2, another characteristic is introduced that is referred to as the root angle of the clad track. Although seemingly an independent characteristic, this angle θ' can be approximated in terms of the width and height of the cladded track [32], as shown in equation 3.

$$\theta' = 180 - 2arctan(\frac{2h_c}{W_c}) \tag{3}$$

Finally, also a theoretical powder efficiency η can be calculated using equation 4.

$$\eta = \frac{A_1 \rho_c v_c}{\dot{m}} \tag{4}$$

Here, ρ_c [kg/m^3] is the density of the material deposited, v_c [mm/s] is the lateral speed of the laser beam as its traveling over the substrate material and $\dot{m}$ [g/min] is the powder feed rate.

2.1.2 Process Parameters

The operational window for laser cladding is typically characterized by laser power P, speed v_c, and powder feeding rate $\dot{m}$, as these are considered the most important processing parameters [27]. Nevertheless, numerous other process parameters, including laser beam spot size, the intensity distribution of the laser beam, shielding and carrier gas quantity and type, as well as the size, speed, and feeding angle and mass distribution of powder particles, also play a significant role.

Erfanmanesh et al. showed in their research the reliance of the clad track width and height as function of the abovementioned three crucial processing parameters, laser power P, scanning speed v_c and powder feed rate $\dot{m}$ [33]. In their study this is referred to as P, V and F. This was done for a laser cladding setup with a coaxial powder supply. In their results, the clad height was found proportional to $P^2V^{-2}F^{1/4}$. The clad width was found proportional to $P^1V^{-1/2}$. The root angle was found to be proportional to $V^{-1}F^1$.

In the work of Onwubolu et al. Diam alloy 2002 was clad onto a DIN steel substrate using a coaxial powder feed [34]. Experiments were carried out using a variety of laser powers, speeds and powder feed rates. In general, clad track height, width were found to increase, whereas root angle was found to decrease, with increased laser power, slower speeds and higher feed rates. A decreased root angle means the inclination of the clad along the edge is more steep.

In the study of Behera et al. an off-axial lateral powder feed was used [35]. A similar trend, as for the co-axial powder feeds was observed. Clad height and width and the cross-sectional area of the clad above the substrate level demonstrated a decrease with increasing scan speed. This while the dilution exhibited an upward trend. Also, the root angle increased. Furthermore, the study observed that a uniform clad track was achieved when powder deposition occurred either behind or in front of the melt pool. However, when the powder was fed from behind, the powder efficiency was lower as compared to feeding from the front, thereby also leading to an increased dilution.

2.1.3 Influence of the Melt Pool Shape on the Clad's Microstructure

In the work of Lee et al. it was found that upon solidification, the temperature gradient G and the solidification rate R are parameters that strongly influence the size and morphology of the dendrites that are developed in a cladded track [23]. Hence, the resulting properties of the cladded track are governed by the values of G and R. The temperature gradient G is defined as a vector that is normal to the solid liquid interface of the melt pool in three dimensions and thus composed out of three temperature gradient

vectors, as shown in equation 5. The value of R is defined by the cladding speed, here R_b, and the angle between the solidification boundary and the cladding direction, θ, as shown in equation 6.

$$|G| = G = \sqrt{G_x^2 + G_y^2 + G_z^2} \tag{5}$$

$$|R| = R = R_b \cos\theta \tag{6}$$

Again, both the values of G and R have a dependency on the shape of the melt pool. Generally, the ratio of G/R determines the morphology of the dendrite structures. That is, the shape and type of dendrites that are formed.

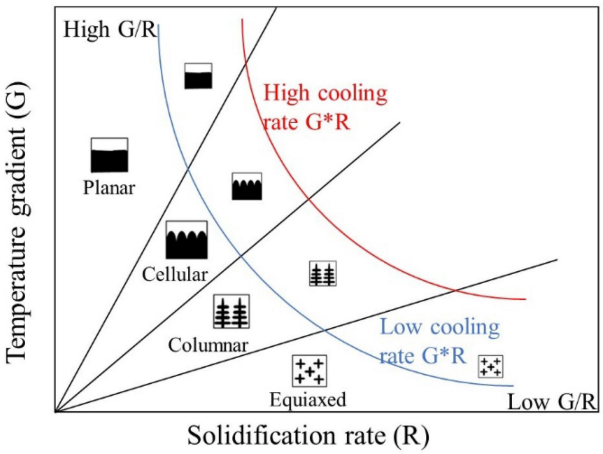

Figure 3: Effect of the temperature gradient G and solidification rate R on size and morphology of dendrite structures [36].

The morphology of the dendrite structures can be categorized into four types, as visualized in figure 3, based on the ratio of thermal gradient G to solidification rate R. Planar dendrites are formed at high G/R ratios, these are developed in a single plane and no branching occurs. Cellular dendrites show some surface perturbations but still no distinct branching occurs. Columnar dendrites are characterized by their elongation in a single direction and with branching in the other direction. At last, equiaxed dendrites are characterized by growth of branched arms equally in all directions. The different types of dendrites have a large influence on properties as strength, toughness, hardness and isotropy.

The product of G and R controls the size of the dendrite structures. Higher values produce finer dendritic structures, while lower values lead to coarser structures. Enhanced mechanical properties are typically found to correspond with finer dendritic structures.

The shape of the melt pool, and hence the related values of G and R, are influenced by the temperature distribution in the melt pool [23, 37, 38]. Within a liquid phase, higher temperature areas exhibit lower surface tension than lower temperature areas. This surface tension gradient drives Marangoni flows. This causes the flow of liquid material from regions of lower surface tension to regions of higher surface tension. These flows affect the shape of the melt pool and ultimately influence the final shape of the cladded track.

2.1.4 Process Physics

The following descriptions of the laser cladding process are adapted from the work of Toyserkani et al. [27]. Upon the laser beam reaching the substrate, a portion of its energy is absorbed by the substrate, whilst also a fraction is absorbed by the powder particles. The absorbed energy by the substrate initiates the formation of a melt pool. This part of the process is exclusively governed by the heat conduction equation. Right after, the powder particles are introduced into the melt pool.

As powder is introduced in the melt pool, momentum is added into the system. Simultaneously, a surface tension gradient arises due to the temperature gradient. This gives rise to fluid flows within the melt pool. This flow, known as Marangoni flow, causes fluid flow from regions of lower surface tension to regions of higher surface tension (as covered in section 2.1.3). Consequently, the energy transfer is now

a function of heat conduction as well as mass convection. Now, describing the laser cladding process involves incorporating the momentum, heat transfer, and continuity equations.

Fundamental Equations

In the laser cladding process a temperature distribution is induced by the intensity distribution of the laser beam striking the substrate. When considering a moving laser beam, as shown in figure 4, the evolving temperature distribution, denoted as $T(x, y, z, t)$, arises from the three-dimensional heat conduction equation in the substrate, as shown in equation 7.

$$\frac{\partial(\rho c_p T)}{\partial t} + \nabla \cdot (\rho c_p \mathbf{U} T) - \nabla \cdot (\mathbf{K} \nabla T) = Q \tag{7}$$

where $T(x, y, z, t)$ is the temperature [K] relative to the ambient temperature T_0 at coordinates (x,y,z) and time (t), ρ is the density of the material [kg/m^3], c_p is the thermal capacity [J/kg $\cdot$ K], K is the thermal conductivity [W/m $\cdot$ K], Q is generated power [W/m^3] and U is the cladding speed [m/s].

The momentum equation is essentially Newton's second law in the context of fluid dynamics. This formulation results in a vector equation and as represented in equation 8, reads,

$$\frac{\partial(\rho \mathbf{U})}{\partial t} + (\rho \mathbf{U} \nabla)\mathbf{U} = \rho \mathbf{g} - \nabla p + \mu \nabla \cdot (\nabla \mathbf{U}) \tag{8}$$

Here, μ is the viscosity [kg/s $\cdot$ m], and $\mathbf{g}$ is the gravity field [m/s^2].

Finally, the continuity equation, which is essentially expressing the principle of mass conservation in the context of fluid dynamics. As shown in equation 9, it reads,

$$\nabla \cdot \mathbf{U} = 0 \tag{9}$$

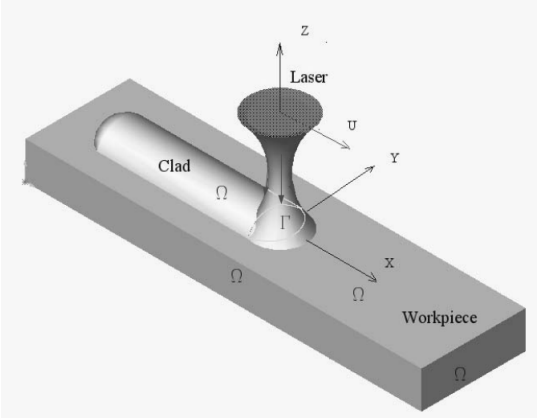

Figure 4: Schematic diagram of the physical domains in a laser cladding process [27].

2.2 Working Principles of Optical Coherence Tomography

This section delves into the theory of OCT, where different types are to be distinguished: Time Domain OCT (TD-OCT) and Fourier domain OCT (FD-OCT). FD-OCT can be subdivided in to Spectral Domain OCT (SD-OCT) and Swept Source OCT (SS-OCT).

The goal of this section is to gain an understanding of FD-OCT imaging that accurately describes its system components and its signal processing. Throughout literature it has become evident that FD-OCT offers superior measuring speeds and resolution as opposed to TD-OCT [39–42]. As for the experimental purposes of this research a FD-OCT system is used, a detailed exploration of a TD-OCT system will not be given. Consequently, the upcoming section entails an explanation of, and only applies to, an FD-OCT system.

In interferometry, light emitted from a low-coherence light source is guided by an optical fiber towards a beamsplitter. Here the beam is split into a so-called "sample arm" and a "reference arm". Light in the reference arm travels a known and fixed optical path length before being reflected by the reference arm mirror. The light from the reference arm is reflected back to the beamsplitter [39].

Light in the sample arm reaches optical components. Here, the beam is scanned (using Galvano mirrors) and upon passing through the focusing lens, focused onto a sample. Following this, the beam interacts with the sample. Thereafter, a portion of the incident sample arm beam is reflected, or backscattered, through the optical components, back to the beamsplitter, as shown in figure 5.

Thus, both the light in the sample arm and in the reference arm return to the beamsplitter. Upon passing the beamsplitter, the waves recombine and the light from both arms interfere. That is, the amplitudes in electromagnetic field from the returning waves either constructively reinforce each other or they destructively cancel each other out, or any combination that lies in between [40].

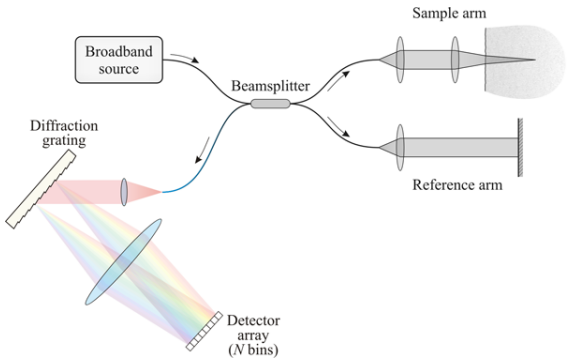

Figure 5: Schematic overview of a SD-OCT system [43].

In SD-OCT, the recombined beams ultimately reach a spectrometer that uses a diffractive element, such as a diffraction grating, that is able to spatially separate the different wavelengths that occur within the interference pattern into on to pixels of the line camera. The scan rate of the camera, determines the rate at which the OCT system is able to perform a single A-scan. That is, because all the pixels in the line camera together constitute the spectral interferogram from which an A-scan is retrieved.

Now consider a scenario, as adapted from the work of Aumann et al. [39], where the sample beam is directed upon a surface that yields a single reflection, belonging to a single depth position, z_1, and a corresponding reflectivity R_1. The resulting spectral interferogram is shown in figure 6(a). The dotted black line is the original Gaussian spectral distribution of the broadband source. The solid blue line, representing the reading from the line camera, shows alternating conditions of both constructive and destructive interference as a function of the wavenumber $k = 2\pi/\lambda$. These so called interference fringes are characterized by their modulation frequency, that is, the frequency of fringe spacing, and is uniquely coupled to the depth position z, where the distance between consecutive peaks is represented by $k = \pi/z$.

Figure 6(b) shows the interferogram of a reflecting surface that is positioned further away, at depth position z_2, where $z_2 > z_1$. With increasing depth, or essentially with increasing path length difference, the fringes becomes narrower and hence the modulation frequency becomes higher.

To illustrate why this happens, consider a scenario where the path length difference between reference arm and sample arm is exactly ten wavelengths, so 8400 nm. In that case, in the resulting interference spectrum, constructive interference will occur at 840 nm. This is because the path length difference is an integer multiple of this wavelength. The same for a wavelength of 933 nm, as then the path length difference is exactly nine wavelengths and also for 764 nm as in that case exactly eleven wavelengths fit in the path length difference. This means that constructive interference peaks occur every 93 nm with this path length difference. Now consider a scenario where the path length difference is exactly 100 wavelengths, so 84000 nm. In that case, again 840 nm will constructively interfere. The next peak in the interference spectrum is observed at a wavelength of 848.5 nm as in that case exactly 99 wavelengths fit in the pathlength difference. Also a peak at 831.7 nm will be observed, as in that case 101 wavelengths fit in the path length difference. The spacing of the peaks in the interference spectrum is less than 9 nm. This illustrates how the modulation frequency is affected by the pathlength difference. Again, the key take here is that constructive interference only occurs when the path length difference is an integer multiple of the wavelength. The corresponding modulation amplitude is proportional to $\sqrt{R_r R_s}$. In which case, R_r is the reflectivity of the reference mirror, and R_s is the reflective of the sample surface.

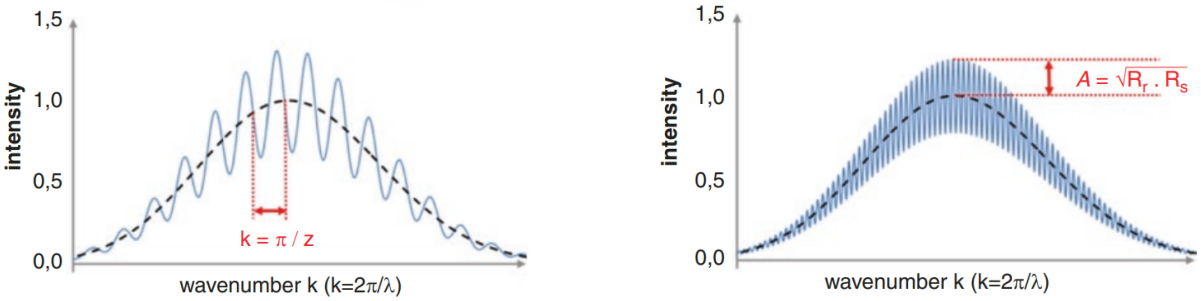

(a) (b)

Figure 6: Spectral interferograms of (a) a reflection at distance $z_1 = 50$ µm, with reflectivity R_1 and (b) a reflection at distance $z_2 = 300$ µm, with reflectivity R_2 [39].

Now consider the scenario where the light in the sample arm penetrates and reflects off of both reflective surfaces. Initially, the sample beam reflects upon reaching the surface of the sample at depth position z_1 with reflectivity R_1. Meanwhile, some part of the sample arm beam penetrates deeper into the material. The light that penetrates deeper reaches another interface where light is reflected. Here, at depth position z_2 with reflectivity R_2. The spectral interferogram corresponding to this scenario is illustrated in figure 7. It can be seen that interferogram is not composed out of a singular modulation frequency. Instead, when dealing with a sample featuring multiple reflections within the penetrable depth of the light source, a superposition of the individual interferograms is seen. Where each reflection yields its own frequency and amplitude within this signal. In this scenario, an inverse Fourier Transform of the spectral interferogram is required to be able to distinguish between the different modulation frequencies and amplitudes that are visible in the combined interference pattern. In the combined interferogram shown in figure 7, it can be seen that that the amplitude of the lower modulation frequency is greater than the amplitude of the higher frequency that is present in the superposition. From this, it can be stated that the surface at z_1 must have yielded a greater intensity reflection than the the interface at z_2.

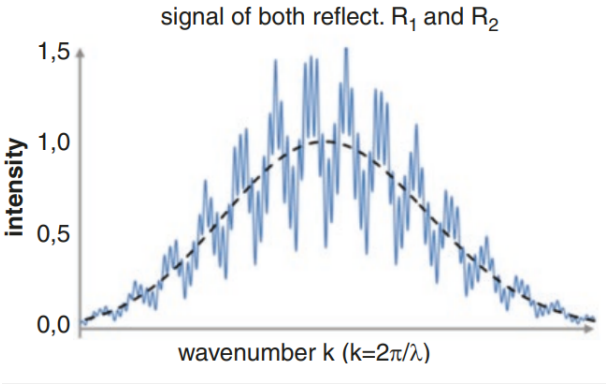

Figure 7: Spectral interferogram of two reflecting surfaces at distances z_1, z_2 with corresponding reflectivities R_1, R_2 [39].

The axial resolution for an SD-OCT system is defined by the coherence length of the light source [44]. This is dependent on the spectral distribution of the light emitted from this source. The coherence length is defined in equation 10.

$$l_c = \frac{2\ln 2}{\pi}\frac{\lambda^2}{\Delta\lambda} \tag{10}$$

A low coherence light source is composed of a broad range of wavelengths and thus, has a broad spectral bandwidth. In contrast, nearly monochromatic light almost solely consists of a single wavelength and thus, has a very narrow spectral bandwidth. This means that wave trains emitted from a nearly monochromatic source exhibit a stable phase relationship for a much larger distance. That is, such a light source has a long coherence length. To obtain a high axial resolution in an SD-OCT, the light source must have a broad spectral distribution in order to have a short coherence length. Hence, a SLD is used [45].

2.3 Signal formation in OCT

Insights were retrieved in the mathematical representation of the signal in OCT. The mathematical descriptions are adapted from the work of J.A. Izatt and M.A. Choma [44]. This starts with a mathematical description of the current as captured by the different pixels on the spectrometer $I_D(k)$ as a function of wavenumber, as shown in equation 11. Here, $S(k)$ represents the normalized spectral distribution of the light source as a function of wavenumber k. This representation also considers multiple reflections at different depths within a sample, z_{S1}, z_{S2}, ..., z_{Sn} with corresponding power reflectivities of R_{S1}, R_{S2}, ..., R_{Sn}. Also, z_R and R_R refer to the position and power reflectivity of the reference arm mirror, respectively. ρ_d is the responsivity.

$$\begin{aligned} I_D(k) = &\frac{\rho_d}{4}\left[S(k)(R_R + R_{S1} + R_{S2} + \ldots)\right] \\ &+ \frac{\rho_d}{2}\left[S(k)\sum_{n=1}^{N}\sqrt{R_R R_{Sn}}(\cos\left[2k(z_R - z_{S_n})\right]\right] \\ &+ \frac{\rho_d}{4}\left[S(k)\sum_{m=1,n\neq m}^{N}\sqrt{R_{Sn}R_{Sm}}(\cos\left[2k(z_{Sn} - z_{Sm})\right])\right]. \end{aligned} \tag{11}$$

To obtain the A-scan from the spectral interferogram, an inverse Fourier Transform is required. The resulting mathematical description of the A-scan as obtained from performing the inverse Fourier Transform on the spectral interferogram in equation 11 is shown in equation 12,

$$
\begin{aligned}
i_D(z) = \frac{\rho_d}{8}\left[\gamma(z)\left(R_R + \sum_{n=1}^{N} R_{S_n} + \sum_{n=1}^{N} R_{S_n} + \ldots\right)\right] \\
+ \frac{\rho_d}{4}\sum_{n=1}^{N}\sqrt{R_R R_{S_n}}\left[\gamma[2(z_R - z_{S_n})] + \gamma[-2(z_R - z_{S_n})]\right] \\
+ \frac{\rho_d}{8}\sum_{n\neq m=1}^{N}\sqrt{R_{S_n} R_{S_m}}\left[\gamma[2(z_{S_n} - z_{S_m})] + \gamma[-2(z_{S_n} - z_{S_m})]\right]
\end{aligned} \tag{12}
$$

Here, the so-called "coherence function" $\gamma(z)$ is the result of performing the inverse Fourier transform on the spectral distribution $S(k)$. In the case of SD-OCT where often an SLD is used, $S(k)$ is representative of a Gaussian function. The Gaussian function, represented by its central wave number k_0 and its spectral bandwidth Δk, and the result from its inverse Fourier Transform are shown in equation 13. Performing the inverse Fourier Transform, yields the so-called "coherence function" $\gamma(z)$.

$$
\gamma(z) = e^{-z^2\Delta k^2} \overset{\mathscr{F}}{\longleftrightarrow} S(k) = \frac{1}{\Delta k\sqrt{\pi}} e^{-\frac{(k-k_0)^2}{\Delta k^2}} \tag{13}
$$

The A-scan that is obtained from performing the inverse Fourier Transform on the spectral interferogram of figure 7 is shown in figure 8. It shows two distinct peaks corresponding to the depth positions of the reflections. Also, an additional very small third peak is observed. The occurrence of this additional peak is covered in section 2.4.1.

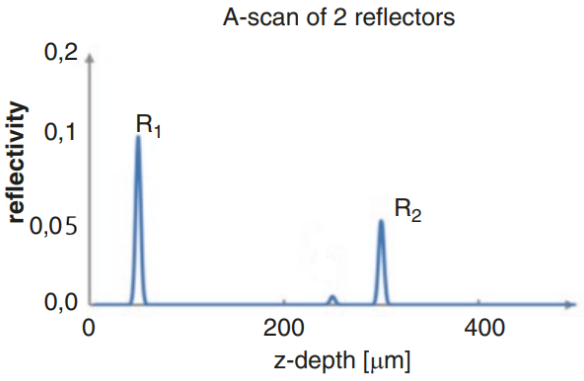

Figure 8: A-scan obtained after applying an inverse Fourier Transform on the spectral interferogram of figure 7 [39].

Distinct Components and Interpretation

The resulting description of the interferogram in equation 12 contains three distinct components, formatted on three different lines. An interpretation of these different components that together constitute the A-scan, again as adapted from [44], is given. An example A-scan where there components are all clearly visible in is shown in figure 9.

The first contribution is referred to as the "DC Term", it becomes the predominant factor in the A-scan when the reflectivity of the reference mirror is greater than the reflectivity of the sample that is being measured. It does not contain any depth information. It is essentially the signal that would still be present in the A-scan even if the sample arm were to be blocked and no interference occurs.

The succeeding component is referred to as "Cross-correlation Term" and is calculated for each reflection within the sample. This term is the component that is important for OCT imaging and yields a peak in intensity in the A-scan at the depth positions that corresponding to the reflection. To achieve that this term is yields a greater intensity in the A-scan than the DC term, the intensity of the reflection of the sample should be greater than the reference arm. This can be achieved by an unequal division of power

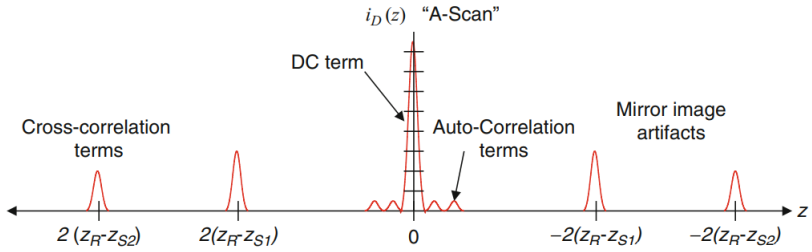

Figure 9: Different components in the A-scan of a sample yielding two reflections at depths z_{S1} and z_{S2} [44].

in the beamsplitter that splits the beam into the reference beam and the sample beam.

The last component referred to as the "Autocorrelation Term" is representative of the interference that occurs between different reflections occurring at different depths within the sample, and are thus of no particular interest.

To consider the impact of variations in the number of reflections within a sample, different scenario's are now considered. In the case of a single reflection occurring at a certain depth within the sample, the A-scan includes only the DC term and a singular Cross-correlation term. In the case of multiple reflections within the sample, the are multiple Cross-correlation terms corresponding to these different reflections. Each term has its own (modulation) frequency and amplitude. Moreover, in cases where there is more than one reflection within the sample, the additional Autocorrelation term emerges. This can also be seen in figure 8, where there is a very small peak visible in between the two larger peaks, as mentioned earlier. For the autocorrelation terms, a similar relation holds regarding the modulation frequency. The greater the reflections are spaced apart, the greater is the resulting modulation frequency of the interference stemming from both reflections.

The OCT system has no way of verifying whether the path length difference between the reference arm and the sample arm is positive or negative, as essentially they produce the same interference pattern. As shown in figure 9, this creates "mirror image artifacts" in the resulting signal. In FD-OCT, this is called the complex conjugate artifact [44]. When the system converts the interferogram from the frequency domain to the depth domain using an inverse Fourier Transform, the result is symmetrically mirrored. This symmetry means that a peak in the A-scan is observed at both a positive and negative depth positions. Thus, the A-scan ends up showing a copy of the depth information.

Also, in figure 9, each reflection in the sample appears to be displaced in the A-scan by a factor of two. This effect stems from the measurement of the round-trip distance to each reflective surface and thus not directly the relative height.

2.4 Laser Material Processing with OCT

In laser material processing, the utilization of OCT has been comparatively limited, unlike its application in e.g. health technology, specifically retinal diagnostics. However, over the past decade and a half, OCT systems have gained increasingly more attention in various laser material processing techniques. A chronological overview of these applications is presented in table 1. Notably, OCT's most recognized or most proposed application within laser material processing is within the laser welding domain. Here, OCT is used in seam tracking, which is essentially controlling the robot arm using the OCT. Also, OCT has been used for monitoring keyhole depth [22, 46–49].

More recently, the application of OCT was found in Laser Powder Bed Fusion (L-PBF), where powder beds are selectively melted using a laser source [50–52]. Very limited is the application of OCT in a laser cladding environment, here an OCT system has been tested in a laser cladding process that equips a co-axial wire feed [53].

To ensure laser material processes are running as supposed to, continuous process monitoring is essential. Current in-situ monitoring, as well as control, relies on CCD-camera's or thermal camera's to monitor the process or the size of the melt pool. The application of OCT in laser material processes offers a different metric for monitoring. That is, the geometry of surface can be retrieved.

2.4.1 Laser Welding

In the context of laser welding, the focused laser beam causes partial vaporization and melting directly at the position the laser beam strikes the substrate. This interaction results in the formation of a thin and deep cavity referred to as the "keyhole". The keyhole is filled with metal vapor and surrounded by a slim cone of molten metal. The opening of the keyhole throughout the welding process is maintained by the pressure of the vapor that holds back the surrounding molten metal. OCT provides an effective means to measure the depth of the keyhole. A comparison between in-situ OCT measurements (Lessmüller Lasertechnik OCT) and a destructive method reveals a strong agreement in keyhole depth [22]. This agreement holds true above laser powers of 1.67 kW with a maximum discrepancy of 70 µm.

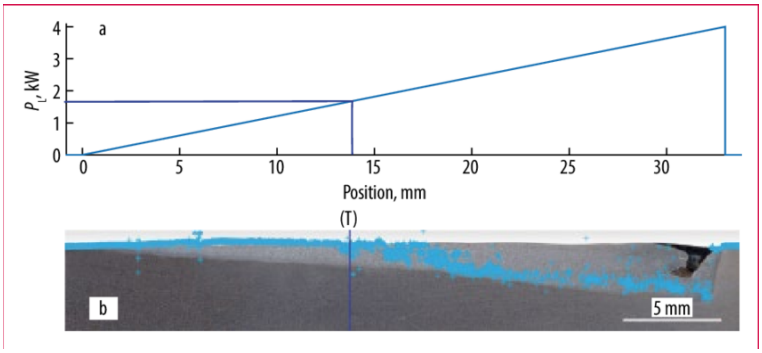

Figure 10: (a) Power-position plot, indicative of the transition from conductive to keyhole welding at 1.67 kW and (b) the measured keyhole depth (blue crosses) overlaid on a bright-field microscopy image cross-section [22].

In the welding experiments depicted in figure 10, a consistent welding velocity of 40 mm/s was maintained, while the laser power was varied. These tests were conducted on a mild steel. The resulting welds were destructively tested. Specifically, the welds were cross-sectioned along their length for subsequent longitudinal bright-field microscopy imaging.

The metallic vapor within the keyhole was found to partially absorb the incident OCT measurement beam. A portion of the reflected light was found to reflect multiple times of the surface of the molten keyhole walls before reflecting back into the sensor. This resulted in the scattering of the captured height using the OCT. There was a consideration that the characteristics of the plasma existent in the keyhole during welding might introduce an inaccuracy as the different refractive index might change the optical path of the reflecting measurement beam. This, in turn, could potentially result in a deeper or shallower keyhole measured. However, within the same study it was shown that the impact of the plasma's refractive index on the OCT measurements is minimal.

The primary finding of the study is that at laser power levels below a threshold laser power of 1.67 kW, there is no keyhole formed in this laser welding configuration. This is referred to as "conduction mode welding". In this scenario, the OCT measurement beam directly reflects of the surface of the laser-induced melt pool. As the laser power increases, surpassing the threshold of 1.67 kW, the substrate undergoes vaporization, leading to the creation of a keyhole. Thus, here it transitions from "conduction mode" to "keyhole mode" laser welding. The OCT proves effective in detecting this transition. The measurements by OCT reveal the increasing penetration depth, which is directly related to the increase in laser power.

2.4.2 Laser Material Deposition with wire (LMD-w)

A study of Stehmar et al. introduced and evaluated a setup that uses a Laser Beam Deposition (LBD) system with co-axial wire feeding, also referred to as Laser Material Deposition - Wire, LMD-w [53]. This system incorporated a SD-OCT for in-situ monitoring of the weld using a circular scan pattern of the OCT measurement beam around the presumed location of the melt pool. Incorporating the OCT system into a LMD-w process was an attempt to eliminate the necessity for post-production quality checks. This was to be achieved by adjusting process parameters in real-time based on the in-situ OCT measurements.

The study limits in-situ measurements to the circular scan pattern, as shown in figure 11(a), and does not utilize the scanning capabilities of the galvo for in-situ monitoring of the melt-pool itself. Instead, a representation of the measured surface, or in this study referred to as 'volume scan', was obtained from the in-situ measurement of points surrounding the presumed location of the melt pool as shown in figure 11(b). That is, points were captured in positions where melting is yet to occur and where solidification presumably has already happened.

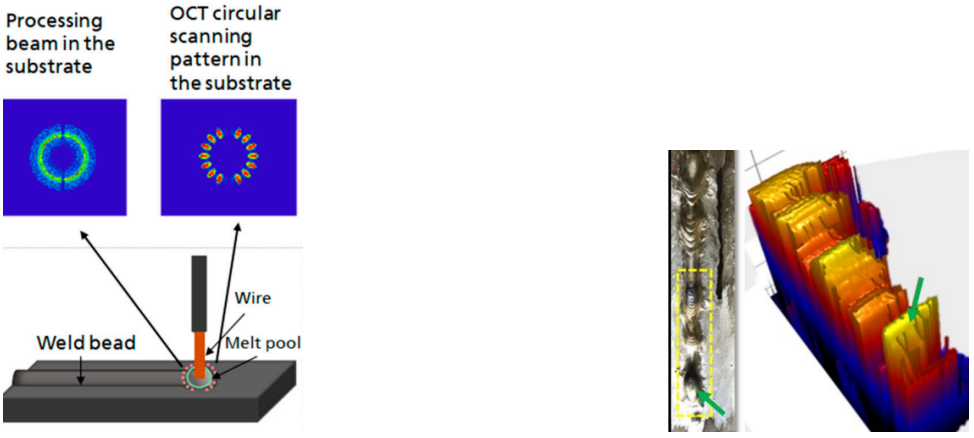

(a) (b)

Figure 11: (a) In-situ OCT scan pattern and (b) resulting 3D surface profile (volume scan) of a clad track deposited using a LMD-w setup [53].

In this experiment, the in-situ measurement follows a circular scan pattern that focuses the OCT measurement beam to positions around the melt pool rather than the melt pool itself. The movement of the processing head facilitates the construction of a volume scan. Consequently, the study does not present results that have captured the melt pool. From this experiment, it can be concluded that the region that is presumably right behind the melt pool, is well measurable using the OCT system, as ultimately a seemingly accurate volume scan is created.

2.4.3 Laser Powder Bed Fusion (L-PBF)

An experiment attempting to capture the characteristics of a laser-induced melt pool using low-coherence interferometry was found in the study of Kanko et al. [50]. This study has integrated an Inline Coherence Interferometry (ICI) system. It is very comparable to OCT as it also makes use of a Michelson interferometer. It is deployed on a Selective Laser Melting (SLM), or Laser - Powder Bed Fusion (L-PBF) system that uses a pre-placed powder bed on top of a substrate that can be moved relatively to the optical head as it rests on an x-y motion stage. A schematic of this setup is given in figure 12(a).

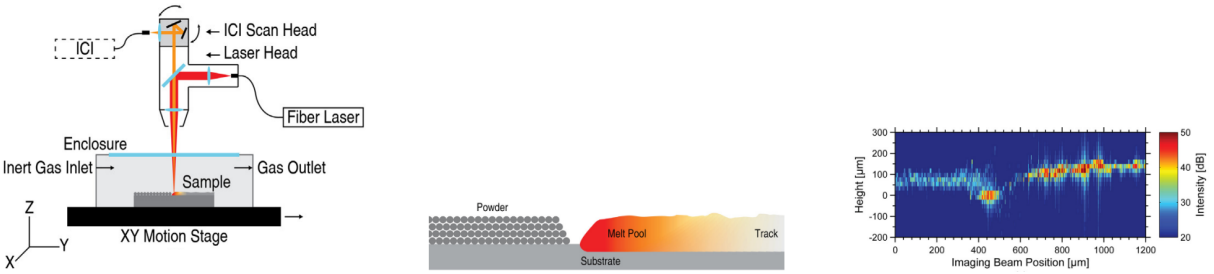

(a) (b) (c)

Figure 12: (a) Schematic overview of experimental setup and (b) the sample during processing (b) and (c) the resulting in-situ OCT measurement [50].

Figure 12(b), (c) illustrate how the melt pool is shaped along its lengthwise direction. It was obtained by longitudinally sweeping the measurement beam along the length of the melt pool during processing. Here, an imaging rate of 200 kHz was used. The coloring in the image is representative of the backscattered intensity at this scan point.

This study reveals visually distinguishable regions along the longitudinal profile of the melt pool, as can be seen in figure 12(c). The regions are distinguishable through the intensity of the reflection per position of the measurement beam. It is observed that in the front-end [0 - 400 µm] the intensity of the signal is comparatively low. In the region behind [400 - 500 µm] it is high. From [500 - 650 µm] the captured intensity is almost completely vanished. From [650 - 1000 µm] it is again high, after which at [1000 - 1200 µm] it is decreased.

This reduced signal density at the front-end area of the melt pool [500 - 650 µm] is explained by specular reflections from liquid stainless steel and the angle of the melt pool relative to the substrate. A substantial portion of the incident imaging light on the front of the melt pool is reflected at angles beyond the numerical aperture of the imaging system. The high signal intensity from [650 - 1000 µm] is mentioned to be caused by the trailing wake of a stable melt pool. Then the transition at [1000 µm] is mentioned to be suggestive of a liquid-solid phase transition, after which light reflects diffusely.

As stated, these distinctive regions are explained by the occurrence of either specular or diffuse reflections of the measurement beam off the surface, as illustrated in figure 13. In the case of a molten surface the incident light is reflected specularly. Upon hitting an inclined surface this results in a reflection beyond the acceptance cone or numerical aperture, as illustrated in figure 13(a). In figure 13(b) it is demonstrated that, in the case of a diffuse reflection (on an inclined surface), such as that caused by a surface with irregularities or with a certain level of roughness, some incident light returns within the acceptance cone of the imaging system. However, this comes at the expense of a diminished intensity of the captured reflection, as a significant amount of light also falls outside the acceptance cone.

2.4.4 Summary

While OCT systems have found diverse applications in various laser material processes, no specific studies were identified regarding its application in laser cladding with powder feed. Also, a research trying to capture the characteristics of the melt pool in laser cladding using an OCT system has not been earlier conducted. Nevertheless, useful insights regarding the behaviour of OCT-like systems were gained from its application in other laser material processes.

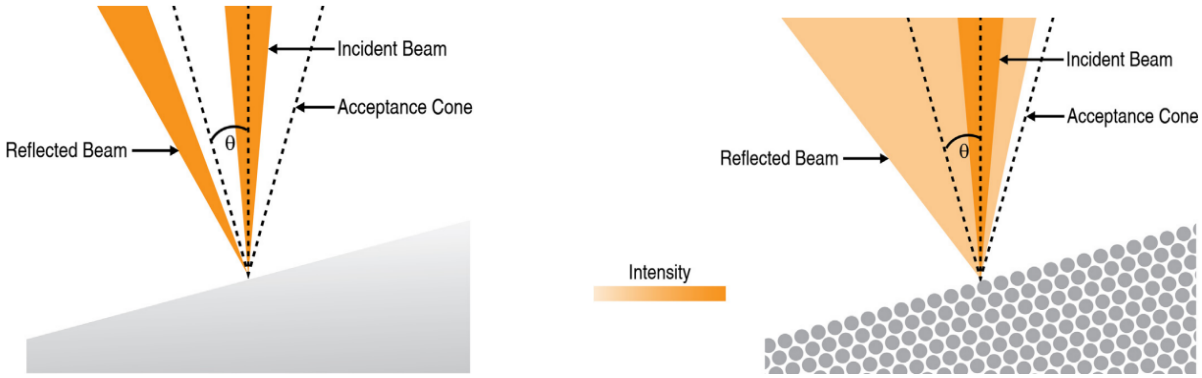

(a) (b)

Figure 13: Schematic comparison of specular (a) and diffuse reflections (b) [50].

Year	**Author**	**Application (Focus of Work)**	**Process**	**OCT Type**
October 2010	Webster et al.	Automatic real-time guidance through ICI in Laser drilling process	Laser Drilling	Unspecified SD-OCT system
April, 2014	Bautze and Kogel-Hollacher	Keyhole depth monitoring in a Laser Welding process using IDM	Laser Welding	Precitec IDM (In-Process Depth Meter)
December, 2015	Kanko et al.	In-situ morphology-based defect detection through ICI in Selective Laser Melting Process	L-PBF	SD-OCT from Laser Depth Dynamics (LD-600-AL)
September, 2017	Dupriez and Denkel	Advances of OCT Technology for Laser Material Processing, specifically Laser welding. Seam tracking and in-process quality control capabilities are discussed	Laser Welding	Lessmüller Lasertechnik OCT on Trumpf BEO 70D
May, 2018	DePond et al.	Quality monitoring, specifically surface roughness, of a L-PBF process	L-PBF	SD-OCT from Laser Depth Dynamics (LD-600)
December, 2019	Fleming et al.	Monitoring powder pack density and consolidation using OCT in a L-PBF process	L-PBF	SD-OCT from Laser Depth Dynamics (LD-600-AL)
December, 2020	Sokolov et al.	Application of OCT for weld depth monitoring in Laser Welding of battery tab connectors	Laser Welding	Precitec IDM
March, 2022	Stehmar et al.	Process monitoring using OCT in a coaxial LMD-w process	Laser Cladding	Precitec IDM
January, 2023	Will et al.	Prediction of electrical resistance using surface topography as measured from application of in-line OCT	Laser Welding	Lessmüller Lasertechnik OCT on Trumpf PFO PFO 33-2
May, 2023	Xie et al.	Laser welding depth determination using OCT	Laser Welding	Unspecified SD-OCT system

Table 1: Chronological overview of appearances of OCT in laser material processing techniques.

3 Experimental Setup and Methodology

3.1 Experimental Setup

3.1.1 Laser Cladding Equipment

The experimental setup for laser cladding features a Yb:YAG disk laser (TruDisk 10001, TRUMPF SE + Co. KG, Germany), utilizing a 600 µm circular core fiber to generate a top hat intensity profile at a wavelength of 1030 nm. Following a beam profiling measurement carried out at 800 W, the following is found. The laser source produces a beam which has a beam parameter product (BBP) of roughly 27.5 mm · mrad. The beam has a beam quality factor M^2 of approximately 83.7. The laser beam is focused using a 425 mm focal length lens, resulting in an approximate spot size of 1.20 mm in focus. The beam profiling measurement is shown in Appendix A.

The system is operated with an IRB-2600M2004 robot (ABB, Switzerland), which provides six degrees of freedom and is equipped with a BEO-D70 optical head mounted on the end-effector. Powder is delivered by a Twin 150 feeder (Oerlikon Metco AG, Switzerland) and introduced into the laser-induced melt pool via an off-axis nozzle (Fraunhofer ILT, Germany) with an inner diameter of 1.5 mm. Argon is used as both the carrier gas at 2.5 NLPM and the shielding gas at 20 NLPM, supplied by separate off-axis nozzles (Fraunhofer ILT, Germany).

Monitoring is achieved with a co-axial thermal camera system, E-MAqS (Fraunhofer IWS, Germany), which operates at a frame rate of 60 fps with a resolution of 640 x 480 pixels. The video captures from this camera system are analyzed using Kinovea software. To determine the camera's field of view in this setup, a broadband Thorlabs lamp was employed as an illumination source, with a sheet of metal featuring cut-out millimeter markings placed above it. To visualize these markings, the lamp must be activated, and the E-MAqS thermal camera's pneumatic long-pass filter should remain disengaged. This configuration enables assessment of both the field of view and a suitable position for the focusing optic, a confocal lens with a focal length of 40 mm, along the beam path towards the camera, ensuring it is capturing in focus. The resulting camera frames are presented in figure 14.

(a) (b)

Figure 14: Colorized E-MAqS camera frames showing illuminated millimeter markings: (a) out of focus, and (b) in focus.

Figure 14 demonstrates that the 640 pixels across the camera frame correspond to approximately 10 mm in width, resulting in a resolution of 15.625 µm/pixel.

The optical head, as shown in figure 15, comprises, among other components, a collimator, mirrors, a dichroic mirror, and a beamsplitter. Also, a crossjet air flow is integrated into this optical head. This component redirects, using pressurized air, contaminants and metal splashes, thereby extending the lifespan of the protective glass, that is protective of the focusing lens. Additionally, the optical head features a CCD camera (TRUMPF SE + Co KG, Germany), which is connected to a display outside the cell the laser operates in. For clarity, power cables, data cables, the powder tube, gas channels, and water cooling channels are not shown.

Using this setup, laser-cladded tracks were laid on a substrate of standard 316L steel using the powder named Micro-Melt 23. The specific content of this powder can be found in table 2. The OCT system deployed in the setup is manufactured by Lessmüller Lasertechnik (Germany), specific details regarding the OCT will be covered in the next section.

Material	Chemical composition (wt.%)									
	Fe	C	Cr	Ni	Tu	Mo	Si	V	Mn	S / N
Micro - Melt 23	Balance	1.30	4.20	-	6.30	5.00	0.35	3.10	0.30	-
Standard 316L	Balance	0.03	16.50-18.50	10.00-13.00	-	2.00-2.50	1.00	-	2.00	≤ 0.1

Table 2: Chemical composition of powder and substrate material.

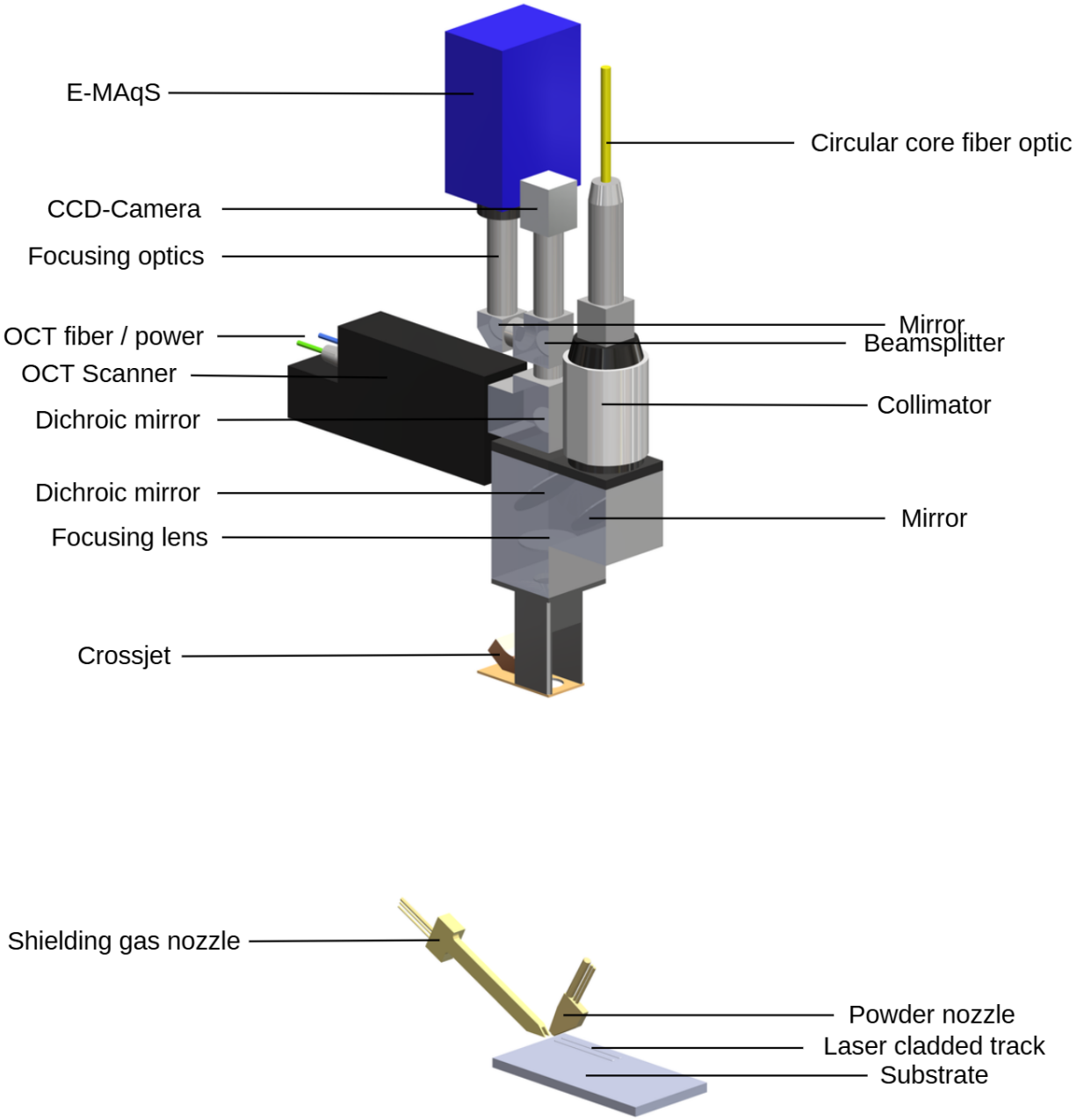

Figure 15: Schematic overview of the laser cladding setup.

3.1.2 Nozzle Alignment

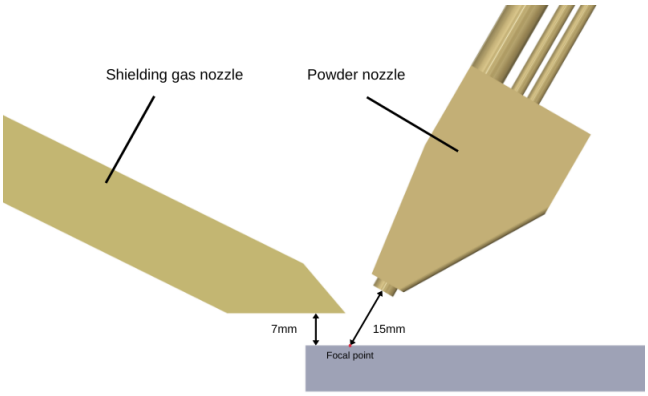

Figure 16: Schematic overview of the nozzle positions.

The shielding gas nozzles are positioned as illustrated in figure 16. The powder nozzle is angled at 60 degrees relative to the substrate. The laser is focused on the substrate surface, positioned 425 mm below the focal lens. During cladding, the substrate is securely fixed in place.

3.1.3 Lessmüller Lasertechnik OCT system

Having delved into the fundamentals of OCT systems and their (basic) signal processing in section 2.3 and 2.4, the focus now shifts to a specific OCT system developed by Lessmüller Lasertechnik (Germany). This particular system, which is used in this research, is manufactured for integration on a TRUMPF laser welding optic (BEO D70). This OCT system is primarily engineered for seam tracking during a (keyhole) laser welding process. There, it is also used to determine the maximum keyhole depth. Furthermore, the system is used to capture the surface profile of the cooled seam, thereby providing insights into the quality of the seam. A schematic setup, representative of the entire OCT system, is shown in figure 17 .

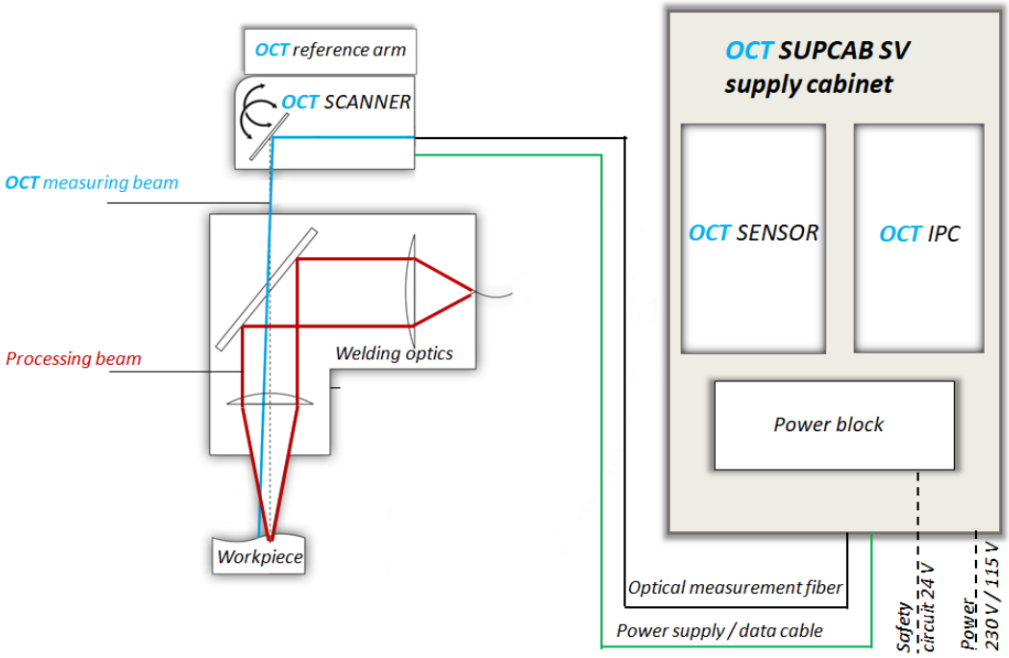

Figure 17: Schematic overview of the OCT system of Lessmüller Lasertechnik mounted on a laser welding optical head [54].

The OCT system consists of two main components: the OCT SCANNER and the OCT SENSOR. The OCT SCANNER is a galvo scanner equipped with two 7 mm mirrors. This scanner offers an angular resolution of 12 µrad, repeatability of 2 µrad, and drift of 10 µrad per degree Kelvin. Its step response time for small angles is 0.2 to 0.25 ms, with a jump velocity of approximately 10 m/s. The OCT SENSOR, an interferometer, is equipped with a light source and a spectrometer. Together, these components qualify the system as a Fourier domain OCT, specifically the spectral domain type (SD-OCT).

The light source in the OCT sensor is a broadband superluminescent light emitting diode (SLED), this source exhibits a Gaussian spectral distribution with a central wavelength of at 840 nm, as is shown in figure 18. This distribution shows a spectral bandwidth of ± 20 nm at full width half maximum (FWHM), that is at a normalized intensity value of 0.5, and a power output of 30 mW.

The radiation of the light source is transmitted to the OCT SCANNER through a polarization-maintaining fiber with a core diameter of 5.5 µm. The interference of the reference arm and sample arm beams takes place within the OCT SCANNER, and this is captured in the spectrometer of the OCT SENSOR. The OCT spectrometer features a 2048-pixel line camera with a lines rate of up to 250 kHz. The exposure time, as used across experiments, is 2 µs. It has an axial measurement range of approximately 12 mm and provides an axial resolution of approximately 12 µm. Integrated within the OCT SCANNER is a folded reference arm with a variable optical length. This design is purposeful, aiming to prevent measurement errors arising from temperature variations between the sample and reference arms. The OCT SUPCAB SV supply cabinet houses the OCT SENSOR and OCT IPC as well as the power block and all different connections. Standard fieldbus connections can be used to facilitate communication between the OCT IPC and the robot.

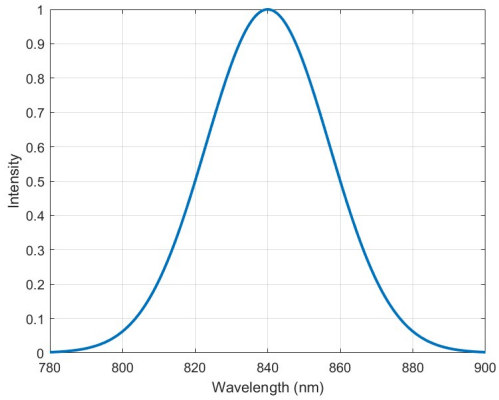

Figure 18: Normalized spectral distribution of a Gaussian SLD centered around 840 nm with spectral bandwidth of ± 20 nm at FWHM.

The OCT system's lateral scanning area covers a ±15 mm radius on the substrate around the center point (0,0), which is large enough to accommodate various stages of a welding or cladding process, including the substrate pre-track, melt pool, and the cooled seam or deposit. The lateral resolution is, at best, 3.18 µm. In this system, axial and lateral resolutions are not coupled, meaning that decreasing the lateral resolution does not have any effect on the axial resolution. Notably, reflections of the process beam during welding or cladding are claimed to not impact the OCT measurement. Also, the OCT system is claimed to be insensitive to dust in the processing environment.

3.2 Methodology

Performing OCT Measurements

3.2.1 Scan Lines

The OCT system by Lessmüller Lasertechnik, equipped with their own software packages (LLT-CLIENT, LLT-TESTER, LLT-PLAYER), allows for a flexible construction of a measurement configuration. The most conventional method being the configuration of a scan pattern using multiple scan lines. This method is also used in the industrial applications as seen earlier, such as precise seam tracking in laser welding.

A scan line represents a specified number of points arranged in a linear fashion, which can be oriented horizontally, vertically, or diagonally at any angle. Curved scan lines are not supported. In this work, scanning refers to the sweeping movement of the galvo scanner as it steers the measurement beam of the OCT along the points of a specified line. A single line can include a maximum of 1000 points. The lateral resolution along a scan line is limited to 3.18 µm. Therefore, a line with the best resolution would span 3.18 mm, if it includes 1000 points.

When configuring multiple scan lines, up to four can be defined. However, the total number of points remains capped at 1000. If a second scan line is added, possibly with a different orientation (horizontal, vertical or any angle in between), the total 1000 points must be divided between the two lines. The galvo scanner sweeps along a line and jumps between lines. Since these jumps to new positions require a brief stabilization time, extend points are used. These are, the first points along a scan line that are not measured or are excluded from evaluation.

A scan pattern can be customized in a 2D window where each line's start and end points are specified, as shown in figure 19(a). Within this window, the tool center point (TCP) is located at the coordinates (0,0). In the context of seam tracking in laser welding, a typical scan pattern consists of three scan lines: one vertical line positioned in front of the TCP (green), which inspects the substrate before welding, one horizontal line crossing the TCP (red), which monitors the weld and melt pool and one vertical line located after the TCP (blue), which examines the freshly laid weld. A similar setup can be deployed on a laser cladding setup, of which a schematic is shown in figure 19(b).

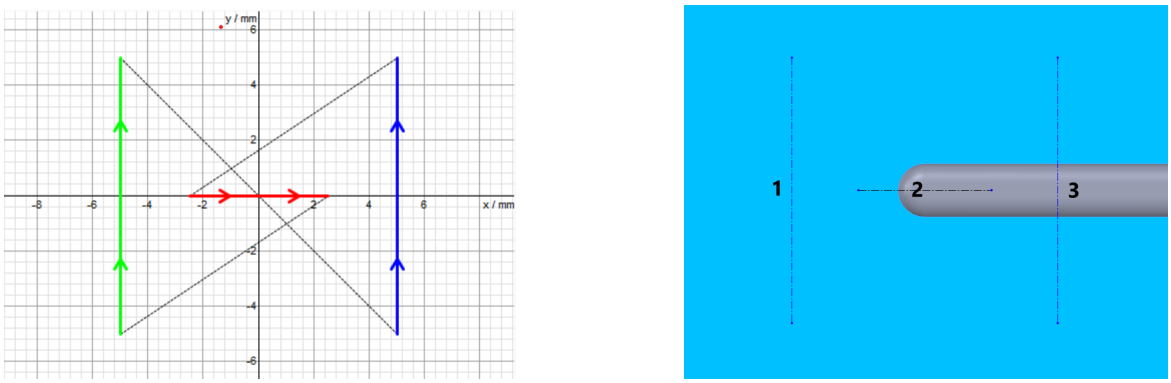

(a) (b)

Figure 19: (a) Scan lines and transition path in configuration mode; (b) schematic showing (1) pre-, (2) in-, and (3) post-process scan lines positioned on a clad track.

Now assume a fictive measurement with only one active scan line containing 500 measurement points, this measurement can be initiated either through fieldbus connection or manual activation. The measurement begins by sweeping the galvo scanner along the specified line. Once 500 points have been measured, a single frame of a video is completed. In this specific case, where only a single scan line is active, the galvo scanner performs a flyback returning to the first position, scanning the same line in the same direction and thereby completing another frame. This process continues, constructing a video frame by frame, until the measurement is stopped. An example of the resulting frames obtained by applying the scan lines during the deposition of a clad track, following the pattern in figure 19, is shown in figure 20. The

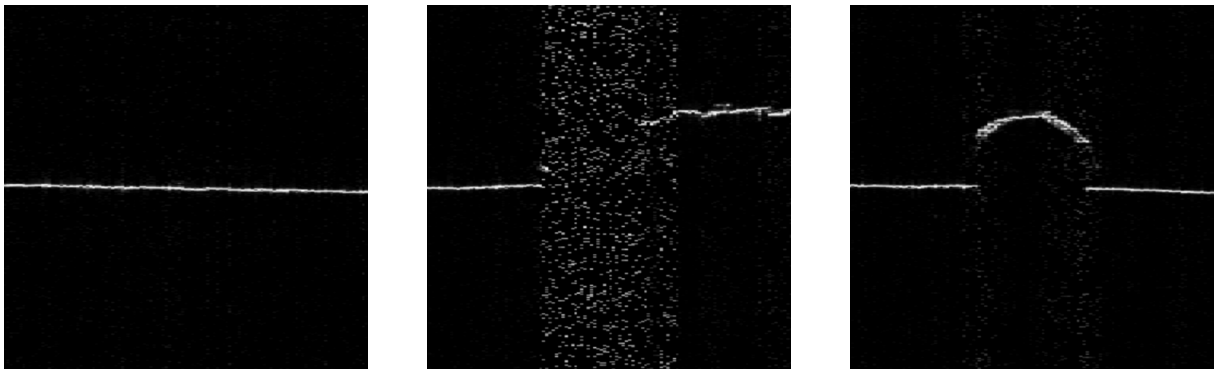

(a) (b) (c)

Figure 20: OCT images made during laser cladding resulting from (a) pre-process, (b) in-process, and (c) post-process scan lines.

video, from which these frames are extracted, alternates between different scan lines, showing a frame corresponding to scan line 1, followed by scan line 2, then scan line 3, and then returning to scan line 1, and so on.

The software enables real-time evaluation during processing using evaluation algorithms. Since the software is primarily designed for laser welding applications, it includes a variety of algorithms specifically made for different weld configurations. These algorithms typically define limits or bounds within which a measurement must remain for the process to continue. If the real-time evaluation detects an issue, such as the weld going off track or exceeding specified limits, the welding process can be automatically halted, and the resulting video of the measurement will be flagged as "NOT OKAY". Using the evaluation algorithms can help in minimizing costly errors.

3.2.2 Raster Scan

Another method for performing measurements is the raster scan. This technique involves measuring a grid of points, like in a raster, hence the term "raster scan". The process begins by defining a scan line, similar to previous methods. The configuration then determines how this scan line is moved to create a 2D grid of measurement points, rather than continuously updating the same line as in the previous method.

Typically, a vertical or horizontal scan line is used, which is then moved linearly to form a square or rectangular grid of measurement points. The configuration allows for specifying the distance between the scan lines. Scan lines can also be rotated to create a circular grid of measurement points. Additionally, a "step wait time" can be specified, which is the time the scanner waits before moving from the end of one scan line to the start of the next. In this research, this has not been used.

Similar to continuous scan line measurements, the measurement can be initiated and terminated either through a fieldbus connection or manually. A significant difference between raster scans and conventional scan line measurements is that, under current software support, raster scans do not utilize evaluation algorithms. Consequently, they cannot be used for direct process control. Unlike continuous scan line measurements, a raster scan operates as a one-time process. It performs the measurement, captures a frame for each scan line in the raster, and then concludes the operation.

Summarizing, the raster scan generates a video containing frames belonging to the scan lines at different positions and ultimately also constructs a 3D point cloud from this data. Yet it does not provide any evaluation during processing.

3.2.3 Frame Information

A single frame, whether obtained from a scan line measurement or a raster scan, results in a 2D grayscale image. In this image, each column of the image corresponds to a single measurement point, while the rows represents the actual relative height position. The height is represented by 1024 pixels, which span a measurement window of approximately 12 mm. This provides a resolution in the image of roughly 12 µm/pixel (12 mm / 1,024 pixels) along the height of the image. The 1024 pixels correspond to the 2048-pixel line camera integrated within the spectrometer, as the Fourier Transform of a real-valued signal generates a symmetric output, with the second half being the complex conjugate of the first, leaving only the first 1024 pixels containing unique frequency information. The captured intensity values are scaled and assigned to the corresponding pixels in the image. Now revisiting the running example where 500 points are defined along a single scan line, a single frame will then produce an image with dimensions [500 x 1,024] pixels. Each column in this image thus contains 1024 pixels, with intensity values normalized to scale proportionally between 0 and 1024. As a result, the limit values of 0 and 1024 will be present in every column. In the visualization, intensity values are mapped to greyscale colors, with 1024 representing white and 0 representing black.

Initially, the resulting image may appear to have a distorted aspect ratio, which is expected due to the different resolutions along the width and height. Along the width of the image, each pixel represents the lateral resolution, calculated as the scan line length divided by the number of points. Along the height, each pixel represents approximately 12 µm. The software does offer an option for aspect ratio correction. However, this is not recommended, as it involves cropping the image and averaging pixel intensities, which can distort the dataset and thereby compromises the accuracy of the measurement. Greyscale images of a clad track profile, both with and without aspect ratio correction, are shown in figure 21.

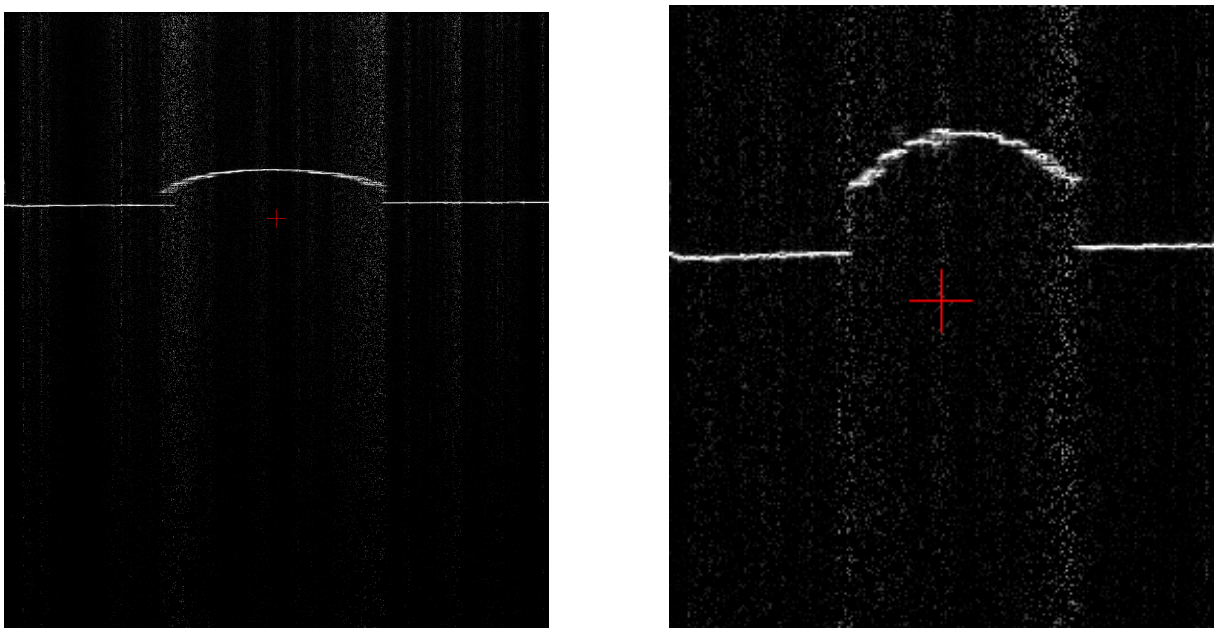

(a) (b)

Figure 21: Greyscale OCT images (a) without and (b) aspect ratio correction.

3.2.4 Point Clouds

3D point clouds can be generated using either continuous scan lines or raster scanning methods. The raster scan method is generally more straightforward and convenient. As already mentioned, once a raster scan is completed, the resulting measurement includes both the images corresponding to each scan line and the generated 3D point cloud. This data is saved as an *.HDRZ* file, which can be opened in the LLT Player software. From this software, the point cloud can be exported as a *.pcd* file for further processing.

Alternatively, continuous scan lines can also be used to construct a 3D point cloud. In this approach, the software constructs a point cloud based on an the speed that is specified. However, the software is designed to handle only straight paths. If the end-effector of the robot follows a curved or angled trajectory, the point cloud will inaccurately represent the 3D geometry, spacing the points according to the specified speed but failing to account for the curvature of the path.

When visualizing a point cloud of a laser-cladded track in the LLT Player software, the need for post-processing becomes evident when analyzing the surface profile. Figure 22 shows a 3D point cloud obtained through a raster scan over a distance of 10 mm and a width of 4 mm. While the surface profile of the clad track can be distinguished, it is not clearly visualized, as many other points are plotted both above and below the substrate and clad track profile. Later, these points will be classified as outliers and filtered out. The rectangular red box is included solely for visualization purposes to highlight the clad track profile.

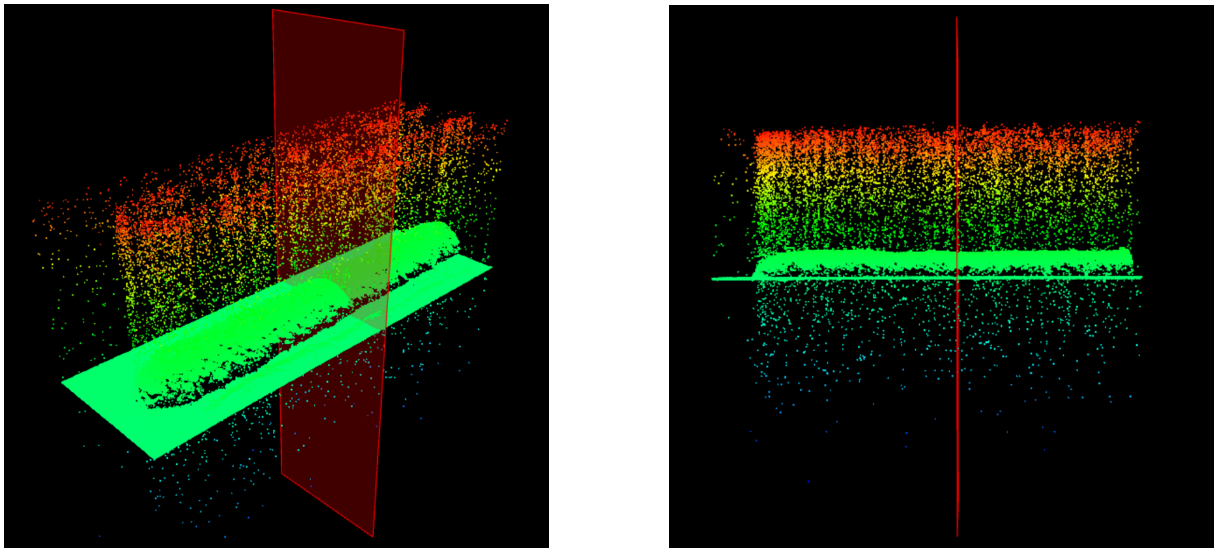

(a) (b)

Figure 22: (a) Corner view and (b) side view on the OCT point cloud, created using an ex-situ raster scan (10 mm x 4 mm), of a clad track (700 W - 5mm/s).

Open3D

Open3D is a Python library designed for handling point cloud files, such as .pcd or .ply formats. The primary goal of using Open3D in this research is to visualize the clad track surface profile more clearly by removing unnecessary points above and below the substrate surface and clad track profile. The process begins by cropping the point cloud, which involves introducing a bounding box to isolate the region of interest. A new point cloud is then created, containing only the points from the initial cloud that fall within this bounding box. Afterward, outlier removal is applied using either one of two methods, namely Statistical Outlier Removal or Radius Outlier Removal [55].

Statistical Outlier Removal

Statistical Outlier Removal (SOR) is a technique that evaluates the Euclidean distances between each point and its neighboring points and removes points that deviate significantly from their local neighborhood. It starts by specifying the amount of neighbors, $nb - neighbors$, to consider. These are the closest points to the point in question. The method calculates the average absolute distance between the given point and its neighbors as well the standard deviation of these distances. For every neighbor, the deviation to the mean is divided by the standard deviation in the local neighborhood to obtain a ratio. This ratio is compared to a standard deviation threshold, $std - ratio$. Neighbors with a ratio greater than the threshold are considered to be outliers and are removed from the point cloud. The $std - ratio$ parameter sets the sensitivity of the filter; a lower ratio results in a more aggressive filter that removes more points as outliers, while a higher ratio is more lenient. Once a point is removed, it will not act as a neighbor for other points.

Radius Outlier Removal

The other method for filtering out points based on their local density is Radius Outlier Removal (ROR). The process works by specifying the minimum number of points $nb - points$ that must be found to the point in question within a specified radius, r_{sphere}, of a spherical region. Points with fewer neighbouring points than the specified $nb - points$ within the sphere with radius r_{sphere}, are classified as outliers and removed from the point cloud. To make the filter more aggressive, one should decrease the $nb - points$ threshold or reduce the $radius$. Vice versa to obtain a more lenient filtering.

Both ROR and SOR methods were tested and deployed on a variety of point clouds containing the surface profile of a clad track. A visual analysis showed no significant differences in their effectiveness. Consequently, the SOR method was arbitrarily chosen for further use. The point cloud shown in figures 23 and 24 may appear as a surface due to the size of the plotted points. However, this is not a surface but a still visualization of all the points. The colorscale is representative of the relative height of the plotted points.

(a) (b)

Figure 23: (a) Corner view and (b) side view of point cloud visualized using Open3D after cropping.

(a) (b)

Figure 24: (a) Corner view and (b) side view of point cloud visualized using Open3D after removing outliers.

3.2.5 Noise

Within this OCT system, a 2048-pixel line camera captures the interference pattern of the signal. The captured height of each measurement point along a scan line, as explained earlier, is represented by 1024 pixels, with each pixel assigned an intensity value normalized to a range of 0 to 1024. Now, two different scenario's are described that are distinguishable in the resulting images.

A strong signal: indicated by a large SNR value. This happens when a large part of the intensity of the measurement beam is reflected back to the sensor.

A large presence of noise: indicated by low SNR value. This happens if the captured intensity of the reflection of the measurement beam of the OCT is very low.

Thus, the apparent noise is quantified by SNR values. Sadly, within the images or point clouds obtained from the OCT measurement, the SNR per measurement point is not stored. This can however still be evaluated from the images. Upon normalization of the intensity values, points that are captured with a large SNR value only show high intensity values and the limit value of 1024 at the correct height position. All the other pixels exhibit very low intensity values. This can e.g. be seen in figure 25(a) in between pixels 400 and 600 (x-axis).

In the case of a point captured with a low SNR value, the correct height position is still shown by an intensity value of 1024, but the intensity of all the other pixels is increased (as a result of normalization). The larger the intensity values of all the other pixels, the lower the SNR value. This can e.g. be seen in figure 25(a) in between pixels 650 and 750 (x-axis). Using the same reasoning, it can also be seen that the SNR at 650 is higher than at 750.

In the case that there is no reflection captured at all, the OCT sensor detects only the reference beam, resulting in a signal without the interference pattern that is needed to retrieve the correct depth position. This leads to intensity values across all height positions, which is essentially noise, as no reflection from from the sample is captured. Since the brightness of the pixels are automatically scaled, or normalized, the highest value is scaled to 1024 and the lowest to 0.

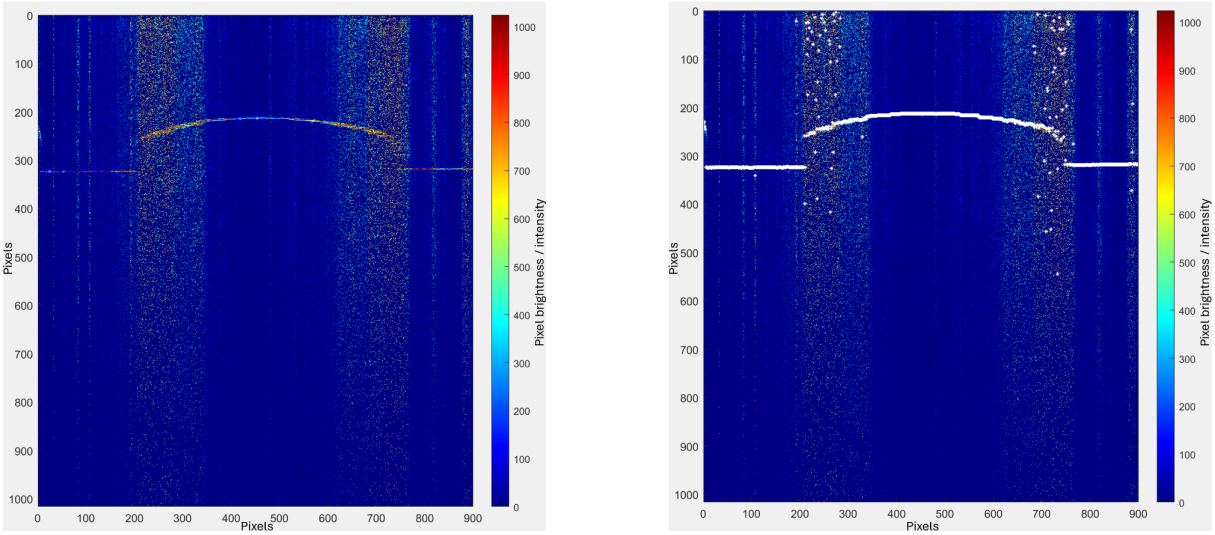

(a) (b)

Figure 25: (a) Colorized frame according to pixel brightness and (b) the same frame with an additional indication of maximum pixel brightness per column (white asterisks).

Figure 25(a) displays a colorized version of the frame obtained by the OCT system, showing the profile of a clad track. In this image, the steep regions of the clad track, particularly along the sides of the track, exhibit significant pixel intensities across entire columns. Figure 25(b) displays the same image, with the pixel of highest intensity in each column highlighted by a white asterisk. The plotting of the maximum intensity values clarifies the construction of a 3D point cloud, as it is the position of these pixels that are plotted as points in the point cloud.

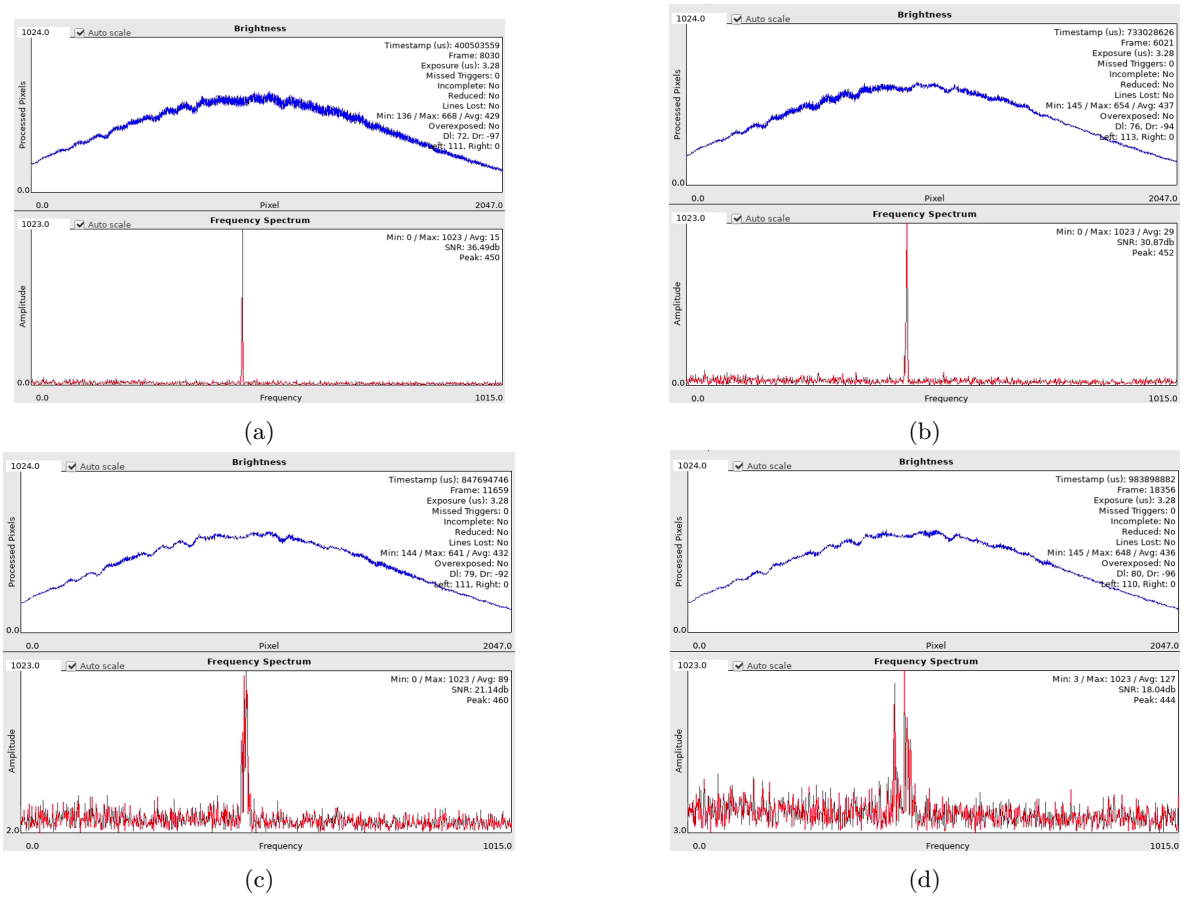

Figure 26: Spectral interferogram and resulting frequency spectrum shown for different substrate angles: (a) flat substrate, (b) 30° angled substrate, (c) 60° angled substrate, and (d) 75° angled substrate.

Building upon previous findings, an experiment was conducted to investigate the relationship between steep regions and noise levels. In the first scenario, as shown in figure 26(a), the OCT measures a single point on a flat steel substrate, resulting in very sharp peak. A singular peak in the frequency spectrum indicates a single depth is clearly determined. Although intensity values at other frequencies are also present, they show a much lower amplitude than the peak, hence yielding a high signal-to-noise ratio of 36.49 dB. In this instance, when considering only a single measurement point, it is possible to retrieve the SNR values using the LLT software.

The experiment is repeated with the substrate inclined at different angles. Figure 26(b) shows that the SNR on a 30° inclined surface has decreased to 30.87 dB and it is observed that the peak has a widened appearance. Figure 26(c) shows a similar effect where the SNR on a 60° inclined surface has decreased to 21.14 dB and the peak has become even broader. Further inclination, up to 75°, as shown in figure 26(d) follows the same pattern, where again a decreased SNR is observed, now 18.04 dB. Also the peak has again broadened as opposed to the lower degree inclinations.

An explanation for this phenomenon could be the influence of the spot size of the OCT measurement beam as it strikes the substrate. When the substrate is flat, the entire measurement spot interacts with a relatively consistent depth, resulting in a sharp and isolated peak in the frequency spectrum. However, when the substrate is inclined, different regions of the circular measurement spot engage with varying depths due to the angle of the surface. This variation leads to a broader peak in the frequency spectrum, as contributions originating from different depths are captured simultaneously, making it more challenging to accurately determine a single depth position. Consequently, the peak becomes less distinct. Additionally, as the illuminated area increases (which is the case when striking an inclined surface), the captured signal intensity of the reflection decreases due to diffuse reflection of the OCT beam over a larger surface. Also, a portion of the reflected light might fall outside the acceptance cone, thus reflecting beyond the numerical aperture of the OCT, thereby decreasing the signal strength and thus also decreasing the SNR ratio. Figure 27 provides a schematic illustrating this behaviour.

(a) (b)

Figure 27: Schematic illustration of a diffuse reflection of the OCT measurement beam on a flat substrate (a) and on a 45° angled substrate (b).

To validate the preceding explanation, a beam profiling measurement was conducted on the OCT measurement beam. The result is displayed in figure 28. The beam profile, as in figure 28(b), appears to exhibit a Gaussian intensity distribution.

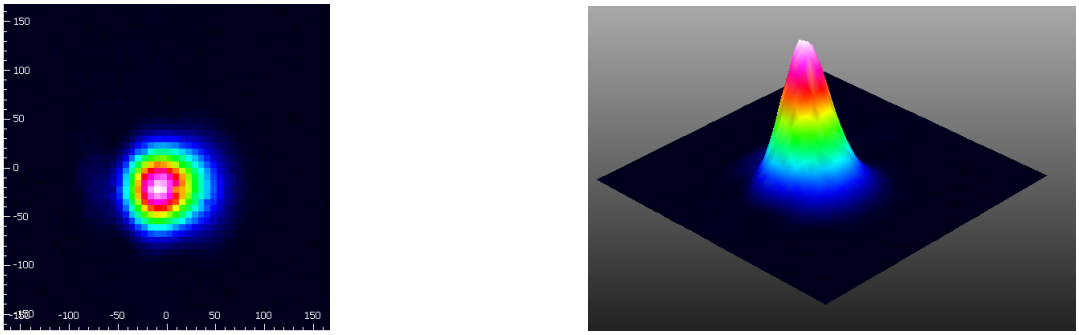

(a) (b)

Figure 28: Beam profiling measurement of the OCT measurement beam in focus, depicted in (a) 2D with scaling in µm and (b) as a 3D surface.

The scaling shown in figure 28(a) indicates that the beam width along both axes measures slightly over 90 µm in diameter. Now, the example scenario as depicted in figure 27 is revisited, where the substrate is inclined at a 45° angle. When the OCT measurement beam strikes this inclined surface, this implies that the OCT measurement beam also covers a vertical height of 90 µm (assuming no divergence of the beam over this small range for simplicity).

Now, if each position on the inclined surface reflects a portion of the incident light back to the sensor, then, given the system's axial resolution of 12 µm, more than 11 pixels (90 µm / 12 µm) will appear in the frequency spectrum, each showing increased intensities or amplitudes. Due to the Gaussian intensity distribution of the beam, the highest amplitude will occur at the beam's center, marking this as the position that is actually measured.

Keep in mind that the maximum lateral resolution is 3.18 µm. This implies that when the OCT measurement beam focuses on a single point, its diameter covers nearly 30 measurement points (90 µm / 3.18 µm) along a line, although it is only measuring at one specific point. Therefore, it is crucial for the

intensity distribution of the beam to exhibit a distinct peak. This ensures that the intensity, at the center of the beam, at the actual position being measured, is the highest. As a result, it is more likely that the reflection at this position will also be at its peak intensity and thus retrieving a correct measurement.

If the substrate surface exhibited perfectly uniform roughness and the beam was ideally Gaussian and again assuming no divergence when out of focus, the amplitudes in the resulting frequency spectrum when directed at an inclined surface would also reflect a Gaussian shape. However, these ideal conditions are not met in practice. Localized variations in surface geometry and roughness can cause certain positions of the OCT beam, even those not at the center and thus not illuminated with the greatest intensity, to exhibit the greatest reflection of intensity and thus the highest amplitude in the frequency spectrum. This effect can also be seen in figure 26(d), where the observed peak in the frequency spectrum deviates from this shape significantly. The situation becomes more complex when considering that the relatively large OCT measurement beam, when measuring the approximately parabolic shape of a cladded track, does not measure a surface with a constant surface inclination. Rather, it is a continuously changing surface inclination. In this case, a larger portion of the intensity of the incident beam is expected to be reflected back to the sensor from positions where the surface is less inclined.

The beam profiling measurement was also indicative of a different effect. That is, an astigmatism in the OCT measurement beam was observed. Above the focus position, the spot size is not circular but exhibits a larger diameter in say e.g. x-direction than it does in the y-direction. Thus, the spot size is not circular but appears to be elliptical. Roughly 10 mm above the focus position, the largest diameter was found to be 160 µm, instead of 90 µm in focus. Beneath the focus position, this is reversed. The spot size has a smaller diameter in x-direction and a larger diameter in the y-direction, also yielding an elliptical spot size. Roughly 10 mm beneath the focus position, the largest diameter was also found to be 160 µm, but in the other direction.

4 Results

4.1 Ex-Situ

This section presents results from ex-situ measurements using the OCT system in laser cladding, focusing on tracks that have already been deposited prior to measuring with the OCT. Therefore, ex-situ refers to measurements taken after the cladding process has been completed, providing a stable environment to evaluate the surface geometry of the clad track. The goal is to assess the OCT system's ability to accurately capture the geometry and to identify the limitations and accuracy when measuring after deposition of a cladded track. First, the 2D surface geometry is analyzed. Second, the accuracy of the OCT system is quantified by benchmarking the OCT measurements results against confocal microscopy. By first understanding the measurement behavior ex-situ, the analysis lays the groundwork for more complex in-situ measurements, where data will be collected during the actual deposition process.

4.1.1 Assessment of Surface Geometry

With a detailed understanding of the OCT system, now finally laser cladded tracks are investigated. It is evaluated whether or not the OCT system can accurately capture the 2D surface geometry of a clad track. By doing so, a general understanding of how the OCT measurement behaves when measuring the geometry of the clad track is gained. The 2D surface geometry is obtained by only considering the points measured from an individual scan line. Clad tracks were laid down according to the main process parameters as shown in table 3. The resulting clad track height, width and aspect ratio are shown. Figure 29 depicts the measured points corresponding to these same experiments.

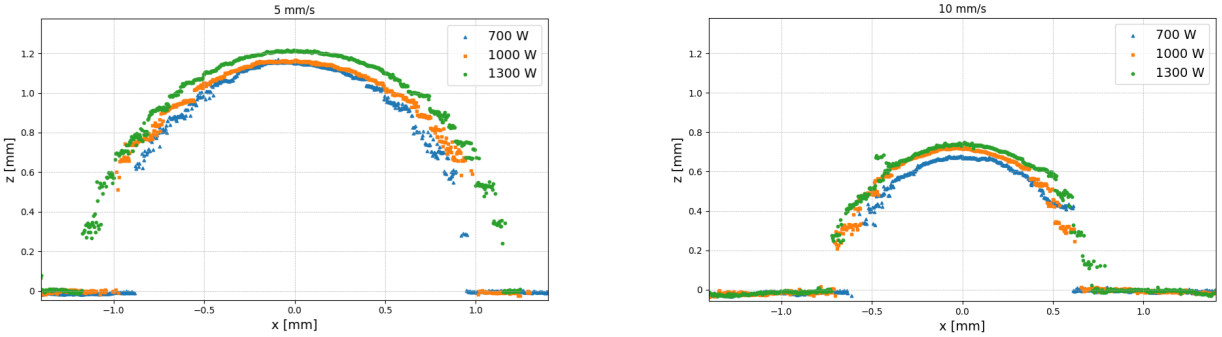

(a) (b)

Figure 29: Points of single scan line extracted from point cloud made after laying down a clad track at a speed of (a) 5 mm/s and (b) 10 mm/s.

Power [W]	Speed [mm/s]	Powder Feed Rate [g/min]	Height [mm]	Width [mm]	Aspect Ratio
700	5	4,8	1,16	1,79	1,54
1000	5	4,8	1,18	1,98	1,68
1300	5	4,8	1,21	2,28	1,88
700	10	4,8	0,66	1,21	1,83
1000	10	4,8	0,72	1,30	1,81
1300	10	4,8	0,75	1,44	1,92

Table 3: Clad track height, width and aspect ratio for laser cladding experiments with a variety of process parameters.

Regarding the figures in Chapter 3, i.e. figure 25, challenges were indicated, particularly with steep track edges. In this study, three cladding experiments were conducted at different power levels (700 W, 1000 W, and 1300 W) while maintaining a constant scanning speed (either 5 mm/s or 10 mm/s). A single scan line from each measurement, from a section belonging to a region beyond the start-up phase, was extracted. Outliers were removed from the point cloud prior to extracting the data per scan line of the clad track.

It is observed in figure 29 that the geometry of the cladded tracks resemble a parabola-like shape. When comparing figures 29(a) and (b) or by looking at the dimensions in table 3, it is seen that there is large decrease in the height and the width of the cladded track whenever a larger speed is used. An increased power level, across different speeds, yields wider and only very slightly, higher cladded tracks. The shape of the cladded track appears to be quite similar for both figures 29(a) and (b), yet the aspect ratio appears to be slightly bigger in the case of a larger cladding speeds.

Regarding the points that are plotted, two observations were made. First, due to the parabolic shape of the clad track, the height difference between consecutive data points naturally increases along the steeper edges as a result of the parabolic-like geometry of the track. However, beyond this expected spacing, an additional spread in the height of the points was observed at the edges. Here it is meant that if the curvature (of the approximately parabolic shape) were to be removed from the data, a larger spread in height will be observed in the points that correspond with the inclined regions along the track. This suggests that the OCT system struggles to capture a single height position in the inclined areas. Also, although hardly visible in figure 29 due to the high lateral resolution of points along a scan line, there are a few points not measured at all. These are located, at the most steep part of the cladded track.

Summarizing, the OCT system appears to be capable of capturing the 2D surface geometry. Differences in the dimensions of the cladded tracks, with the current variation of process parameters, are clearly observed. Next to that, the OCT shows consistent difficulties in capturing the steep edges of the clad track, with an increased spread of the captured height in these regions. Also, a few missing points are observed. To better quantify these issues, a comparison with reference measurements using confocal microscopy will be made.

4.1.2 Benchmarking OCT against Confocal Imagery

In this section, a comparative analysis is presented between point clouds generated by OCT and via confocal microscopy. The point clouds contain the surface geometry of cladded tracks. Similar to OCT, confocal microscopy is an imaging technique that is able to create point clouds. Aside from the difference in their measurement technique, there are variations in resolution, the resulting point cloud density, and acquisition speed. For example, the point clouds generated by the OCT are unable to achieve the same amount of points measured in a certain region as the point clouds obtained from confocal microscopy. The objective of this comparison is to evaluate the accuracy of the OCT system relative to the confocal microscope. By using the confocal point cloud data as a reference, the accuracy can be assessed.

Specifications

The instrument used in this research for confocal imaging is the Sensofar S Neox (Sensofar Metrology, Spain). In this study, the confocal mode of the microscope was utilized. The Sensofar S Neox includes a stitching feature in its software (SensoSCAN / SensoVIEW), which allows for the measurement of consecutive areas on a substrate with overlapping regions. The software then stitches these overlapping regions together, creating a larger area that is captured in a single file.

Confocal microscopy operates by focusing a light source with a narrow spectral distribution laser through a pinhole aperture to illuminate a sample. Reflections of the incident light beam from the position where the light is in focus, reaches the detector [56]. Reflections from height positions that are out of focus are not captured. Thus, at a certain focus position, a single plane is in focus and is captured. By changing the focus position along the height with a specified step size in the order of µm, the microscope reconstructs a 3D representation of the surface. In this research, a part of a clad track was captured using a 10X objective lens by scanning an area consisting of 24 sections arranged in an 8-column by 3-row configuration. The total scanned area was 10.96 x 3.30 mm^2, with a pixel resolution of 8500 x 2560 pixels, yielding a spatial resolution of 1.29 µm/pixel. A z-range of 1850 µm was covered, with a step size of 2 µm, requiring 926 measurement planes. The obtained surface profile, after a measurement is completed, is initially saved as a *.plux* file. Ultimately, for comparison with point clouds generated by the OCT, the confocal data is also exported as a point cloud file, just as the OCT data, in *.pcd* format. The resulting point cloud, following the specifications above, contains roughly 22 million points.

Procedure

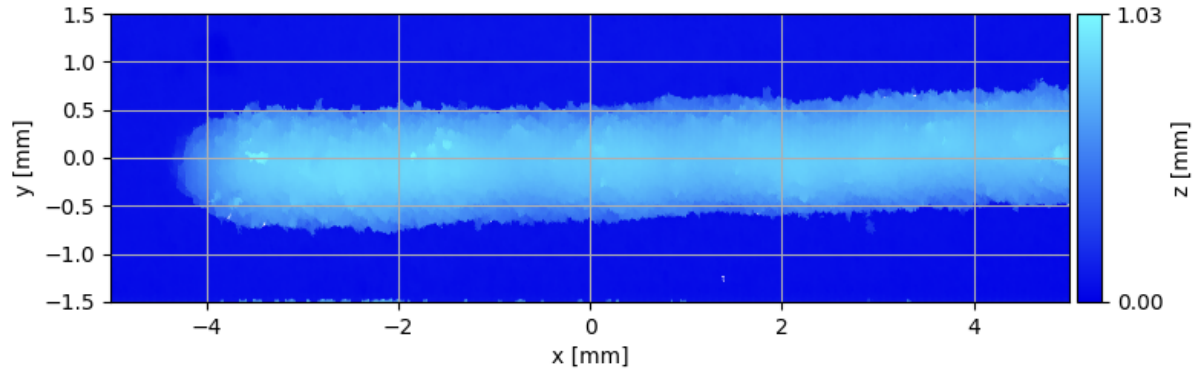

(a)

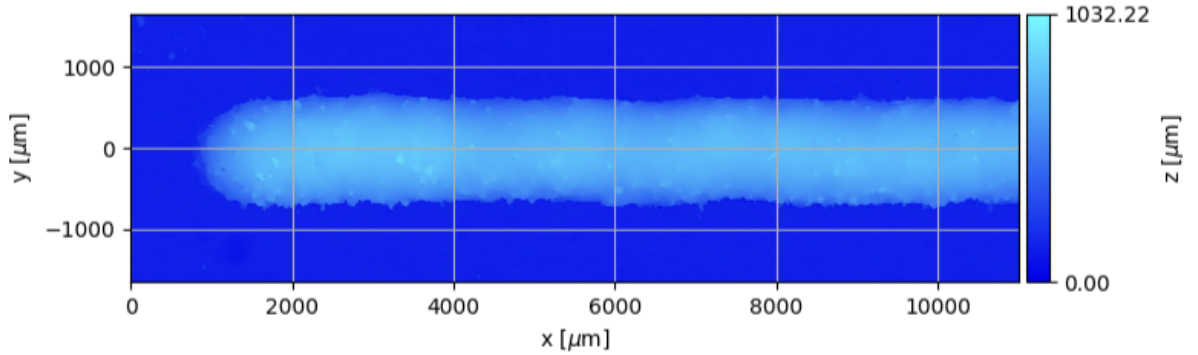

(b)

Figure 30: Point cloud obtained of a clad track laid down at a laser power 700 W and a speed of 10 mm/s by utilizing (a) OCT and (b) confocal microscopy.

In this experiment, the Open3D library was used to process and analyze two point clouds derived from the two different measurement techniques. An example originating from a clad track that was measured using both techniques is displayed in figure 30(a) and (b). Open3D is a Python library designed for working with 3D data structures, including point clouds. By leveraging Open3D, both point clouds were imported into the Python environment for further analysis. Once the point clouds were imported, a registration process was applied to align them. Registration here refers to a step in the analysis where two point clouds are aligned as close as possible in the same coordinate system, thereby allowing for a direct comparison. The method used for registration in this experiment was a iterative transformation, including translation, rotation, and scaling, using a point-to-point strategy. This approach computes the optimal transformation matrix that minimizes the distance between corresponding points in the two point clouds. Correspondence refers to the identification of pairs of points, one from each point cloud, that are ultimately found to be closest to each other. Upon iterating, with a different transformation matrix, the set of corresponding points is changing. The point clouds are typically referred to as the source and target, with the source being transformed to align with the target. Within this analysis, the point cloud stemming from the confocal microscope is considered to be the source, and the point cloud from the OCT is the target.

The point-to-point registration method relies on an iterative approach to minimize the differences or ensure accurate alignment between the two point clouds. For each point in the source point cloud, the algorithm searches for the nearest point in the target point cloud to establish a correspondence. This nearest point is identified based on the Euclidean distance between the points. However, not all points in the target point cloud will find a correspondence in the source point cloud. That is due to differences in point cloud density. The denser point cloud (confocal) will have more points than the sparser point cloud (OCT), meaning many points in the denser cloud may not have corresponding points in the sparser cloud as there no points left to form a correspondence with. These unmatched points are excluded from the registration process. Also, a maximum allowable distance, referred to as a correspondence threshold, is defined. If the closest point in the target point cloud is farther away than this threshold, the point in the source point cloud is considered to have no valid correspondence, and will be ignored. In the

registration, this value has been set to 1 mm. This, to ensure that only meaningful correspondences are considered. Thus, the registration method works by iteratively trying to minimize an objective function that quantifies the total difference between corresponding points by altering the transformation matrix in each iteration. The objective function looks as follows,

$$E(T) = \sum_{i=1}^{N} \|T(\mathbf{p}_i) - \mathbf{q}_i\|^2 \tag{14}$$

Here, T represents the transformation (which includes translation, rotation, and scaling), $\mathbf{p}_i$ are the points in the source point cloud, $\mathbf{q}_i$ are the corresponding points in the target point cloud, and N is the total number of correspondences found. In the iterative point cloud registration process, the algorithm starts with an initial estimate of the transformation parameters (translation, rotation, and scaling). In each iteration, the source point cloud is transformed using these parameters, and correspondences with the target point cloud are identified. The value of the objective function is computed. Thereafter, the transformation parameters are adjusted and the process repeats itself. Again, the value of the objective function is calculated. This process is repeated for a finite number of iterations or until the changes in the value of the objective function fall below a convergence threshold, indicating that the alignment has stabilized. In the experiments a maximum number of iterations was set to 500, yet the value of the objective function appeared to stabilize before reaching this number of iterations.

After the registration process has completed, resulting in the alignment of the two point clouds, the next step involves partitioning both the source and target point clouds in different sections along the entire length and width of the clad track. This partitioning allows for an assessment of the alignment across different sections of the track. Then a function is applied to these partitions to quantify the Root Mean Squared Error (RMSE) within each section. The RMSE provides a measure of the average distance between corresponding points in the source and target point clouds for each partition. However, as the point clouds are partitioned into different sections, there might be correspondences (earlier found in the registration process) where the point from the OCT is now in a different partitioned section than the corresponding point from the confocal point cloud. Consequently, new correspondences need to be identified in order to compute the RMSE. This is easily done by identifying the closest points to the points of the target point cloud. As registering has already been carried out, this is no iterative process with transformation, but simply determining the point that has the shortest Euclidean distance to the point looking for a correspondence. Thus, corresponding points are again identified and the RMSE in a partitioned section is computed as follows,

$$\text{RMSE} = \sqrt{\frac{1}{N}\sum_{i=1}^{N}(d_i)^2} \tag{15}$$

where d_i represents the distance between corresponding points in the source and target point clouds, and N is the number of point pairs or correspondences in this partition. The resulting RMSE values are expressed in millimeters [mm].

By computing the RMSE for every partition, an overview is obtained of where the correspondence between the point clouds is particularly good and where there are larger discrepancies. The partitioning process involves choosing the number of sections along both the length and width of the track. The result is a 2D map where each block represents a specific partition of the clad track. In this map, each block is color-coded based on its RMSE value, which visually indicates the alignment accuracy in that section. Areas with lower RMSE values are shown in a dark blue color, representing better correspondence, while blocks with higher RMSE values are shown in a red color, highlighting regions with larger distances between correspondences. For this, the width is partitioned into 50 different sections, and the length is partitioned into 150 different sections. Hence, the RMSE values is computed for 7500 different regions along the track. Every region contains roughly 60 correspondences.

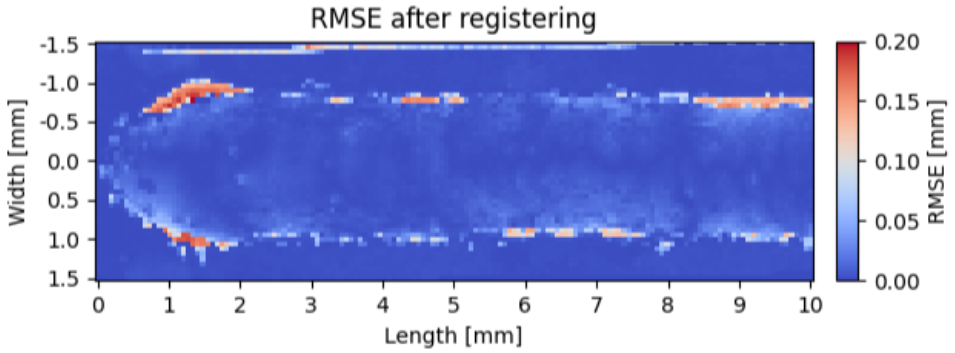

(a)

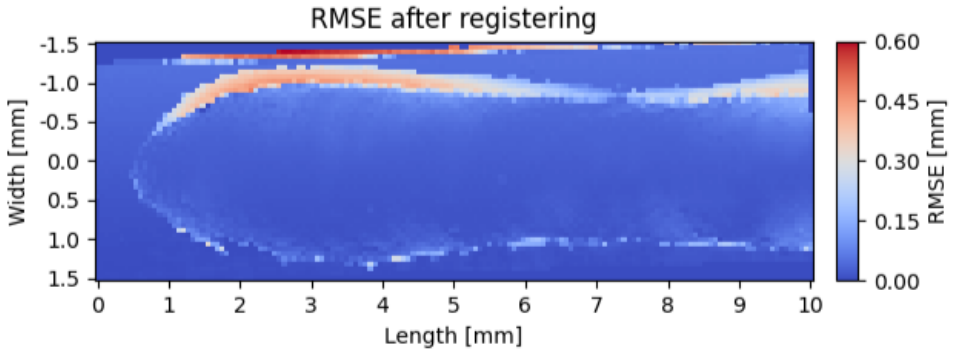

(b)

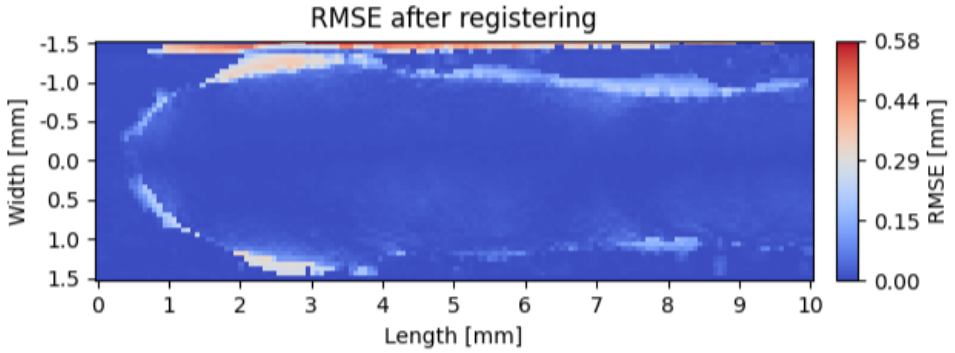

(c)

Figure 31: RMSE after registering OCT point clouds to their corresponding confocal microscopy point clouds containing clad tracks laid down at a speed of 5 mm/s and a laser power of (a) 700 W, (b) 1000 W, (c) 1300 W.

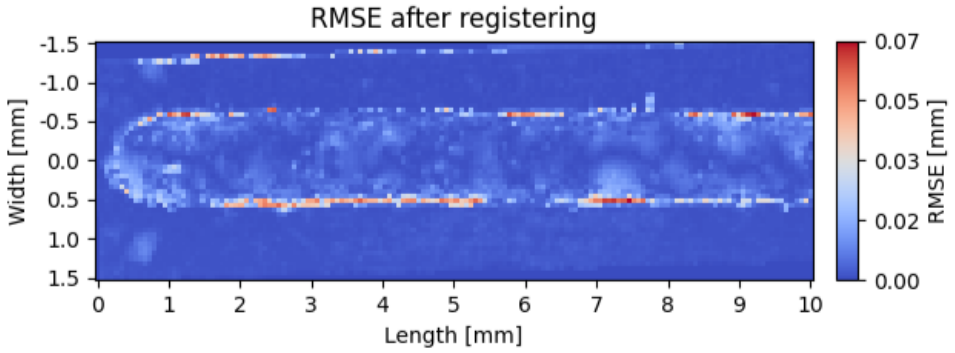

(a)

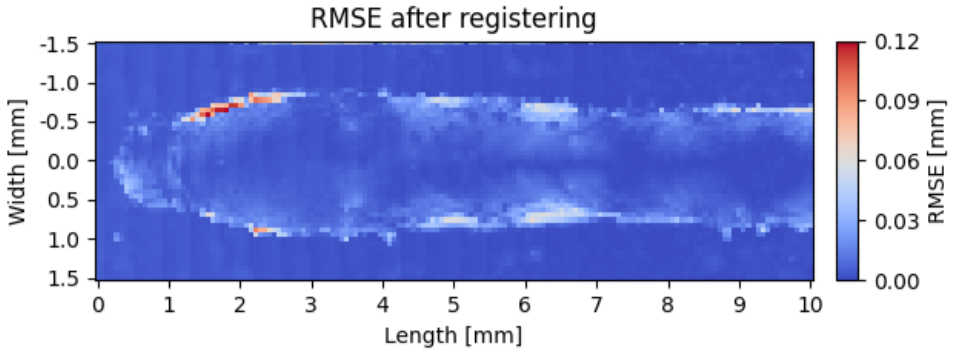

(b)

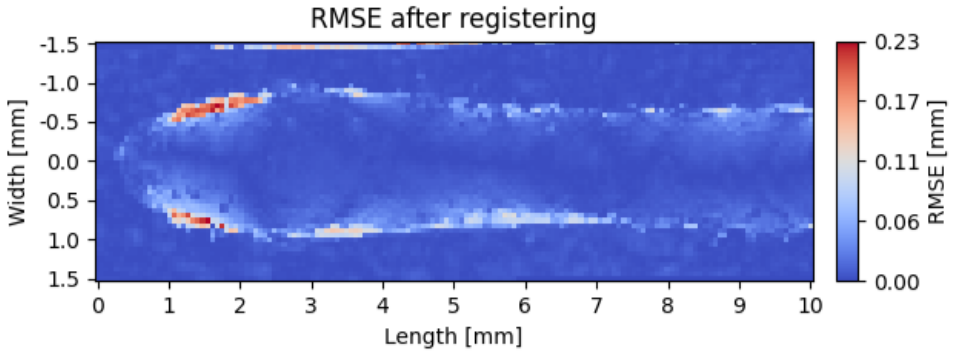

(c)

Figure 32: RMSE after registering OCT point clouds to their corresponding confocal microscopy point clouds containing clad tracks laid down at a speed of 10 mm/s and a laser power of (a) 700 W, (b) 1000 W, (c) 1300 W.

The resulting RMSE values along the clad track are illustrated in figures 31(a), (b), (c) and 32(a), (b), (c). The figures utilize color codes, which, as previously discussed, are shown as such that the highest RMSE value in each figure is represented by the darkest shade of red, while the lowest value is depicted as the darkest blue. Note that this scaling is applied individually to each figure. Consequently, the color gradients are not directly comparable across the different figures, as the range of RMSE values varies from figure to figure. A key observation in figures 31 and 32 is that the highest errors, across al figures, consistently occur along the boundaries of the clad track. Thereby outlining the contour of the deposited track. Consequently, the 2D RMSE plots unmistakably depict the shape of the track from a top view. Also, it is observed across the different figures that RMSE values tend to increase when going towards the edges.

In figures 31(b), (c), it is seen that the highest RMSE value is not part of the actual clad track but appears at the top of the figure, near -1.5 on the y-axis (width). This trend is consistently visible across all figures and represents a phenomenon that has not been previously observed or discussed. The elevated RMSE value originates from the OCT measurement, as illustrated by the example OCT image shown in figure 33. In this figure, the left side of the image shows an increased height, even though this position corresponds to a flat substrate. It indicates that the OCT fails to accurately capture the surface geometry at this position. It remains unclear why this effect is apparent in the OCT measurement.

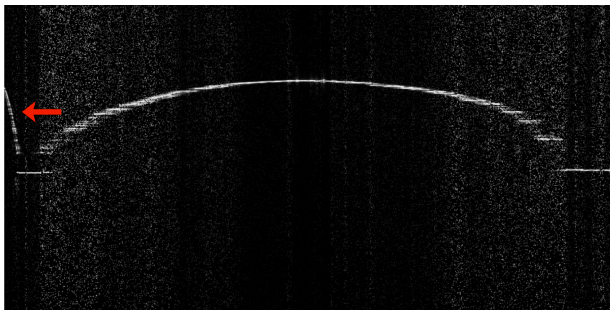

Figure 33: OCT image showing bump on the side of the image as indicated by the red arrow.

Following the understanding gained in Chapter 3, higher RMSE values are expected at steep surfaces or at surfaces where the surface inclination is continuously changing, such as the approximately parabolic shape of a clad track.

In the results of section 4.1.1 it is observed that the shape of the clad track, using different process parameters, is fairly consistent. That is, although the height and width change a lot, the maximum observed difference in aspect ratio is only about 0.3. Due to the spread of points at steep sections, it is difficult to determine the exact surface inclination angle at different points along the curvature of the track. However, it could be argued that tracks with a lower aspect ratio exhibit greater surface inclination angles. This would translate in the expectancy of greater maximum RMSE values for tracks with a lower aspect ratio.

However, it is seen from the figures 31(b), (c) and 32(b), (c), that the width of the track is not stable across the length of this section. Also the height of the cladded tracks is not stable along the length of this section. As a result, it is observed that also the aspect ratio does not exhibit a constant value along this section of the track. This is due to the fact that the captured region is actually the start of the clad track that is subjected to start-up effects of the cladding process. Hence, the captured geometry in the point cloud is not representative of the geometry of the clad track that is observed further along this track. Thus, in this comparison, the relation between the RMSE values and the processing parameters is not clear anymore.

When the OCT measurement beam strikes a steeply angled surface, the intensity of the reflection that is captured is reduced. This reduction occurs because, at steep angles, a portion of the reflected light is directed outside the acceptance cone of the sensor, as illustrated in figure 13. Although some light does manage to return to the sensor due to diffuse reflection, the overall signal intensity is diminished. Consequently, the signal-to-noise ratio (SNR) decreases. This effect is evident in our findings from Chapter 3, particularly in figure 25, where increased noise is noticeable in the steep regions of a clad track and in figure 26, where this is confirmed.

The broadening of the peak in the frequency spectrum, as shown in figure 26(b), likely explains the deviations from the reference point cloud obtained through confocal microscopy. On inclined surfaces, the OCT's circular measurement spot encompasses multiple depth positions rather than a singular one. The depth plotted in the point cloud corresponds to the position that returns the highest intensity reflection. Essentially, the retrieved height could represent any depth within the spot size, depending on which position reflects the most light. Yet, following the intensity distribution of the OCT measurement beam, it is likely that the largest reflection is yielded by the position that is struck by the center of the beam. However, it could be that due to the very localized variations in surface geometry or roughness, a position other than the one directly struck by the center of the beam may produce the strongest reflection. Hence, this would result in a plotted point within the point cloud with a height that does not align with the height of the intended measurement position. Thus, making use of such a large beam spot size (compared to the lateral resolution), it has become challenging to accurately identify a precise depth as it actually captures multiple depths where it is likely that at some position a depth position is retrieved that is not representative of the position that is being measured. This results in increased RMSE values between the OCT and the reference measurement.

Beyond this effect and SNR considerations, the accuracy of the reference confocal measurement can also be a limiting factor. The confocal system, used as a baseline for comparison, may not perform optimally at steep angles, leading to potential inaccuracies in the reference data.

In summary, the primary observation is that OCT measurements exhibit the most significant deviations from confocal measurements in steep regions. This discrepancy arises primarily from the broadened peak in the spatial domain following the FFT of the spectral interferogram, which complicates determining an accurate height position. Additionally, the reduced intensity of the reflected light that is captured on inclined surfaces leads to diminished signal strength and a lower signal-to-noise ratio (SNR). At some positions, points are not measured at all as there is no effective means to differentiate the true signal from the noise due to the low intensity of the reflected light. Lastly, inaccuracies in the confocal reference measurements may also contribute to these observed discrepancies.

4.2 In-Situ

After capturing surface geometries ex-situ with the OCT system on clad tracks, the OCT system will now be applied in-situ to measure during processing, as ultimately this is the area of interest. Before using the OCT system in an in-situ laser cladding environment, experiments are conducted in an in-situ laser welding environment before moving on to the more complex laser cladding experiments.

Laser Welding

Conductive laser welding, which avoids keyhole formation, is a simpler process than laser cladding, making it a suitable starting point for classifying the in-situ behaviour of the OCT system. In conductive laser welding, the laser moves at a constant speed over a fixed substrate, with no material build-up since no powder is introduced into the melt pool.

4.2.1 Evaluating the Impact of Shielding Gas and Powder Stream on OCT Measurements

In the context of a lateral powder supply cladding setup, the OCT measurement beam is steered by galvo scanners to scan the region surrounding the focal point of the processing beam. During this scanning process, there are instances where the OCT measurement beam path is obstructed by the lateral powder flow. To better understand the implications of this on the resulting OCT measurement, an experiment is conducted with an intersecting powder flow in a laser welding setup.

To effectively isolate and demonstrate the influence of an intersecting powder stream on OCT measurements, it is essential to eliminate other variables that could affect the results. Therefore, the experiment is designed in two phases to ensure that any observed effects are solely due to the intersecting powder stream.

First, an experiment is conducted where the laser is moved across a fixed substrate while the OCT system performs a raster scan. No powder stream is introduced during this phase, allowing us to establish a baseline measurement of the substrate's surface without any obstruction in the beam path.

Second, a similar experiment is conducted, but this time, a powder stream is introduced that passes through both the processing beam and the OCT measurement beam, close to the substrate. However, the powder is directed in such a way that it does not actually strike the melt pool, preventing the formation of a clad deposit. The resulting OCT measurements are compared. This approach allows for the assessment of the effects of the powder flow without the additional variables introduced by cladding. As the powder is not directed into the melt pool this is essentially a (conductive) laser welding experiment. Similar experiments are then repeated with additional shielding gas applied from the side. This enables the assessment of the effect of shielding gas on the OCT measurement, with or without intersecting powder flow.

The four different experiments are conducted at a laser power of 1000 W and a scan speed of 10 mm/s. In the two experiments using Argon shielding gas, a flow rate of 20 NLPM is applied. For the two experiments involving a powder stream intersecting the measurement beam, 4.8 g/min of powder is used, matching the powder density in the cladding experiments. This powder is delivered with Argon gas at 2.5 NLPM. A schematic overview of the experimental setup of the four experiments is shown in figure 34, illustrating the shielding gas nozzle (left), powder nozzle (right), powder stream (dark grey), Argon shielding gas (light blue), processing beam (yellow), and OCT measurement beam (orange), along with the welding direction.

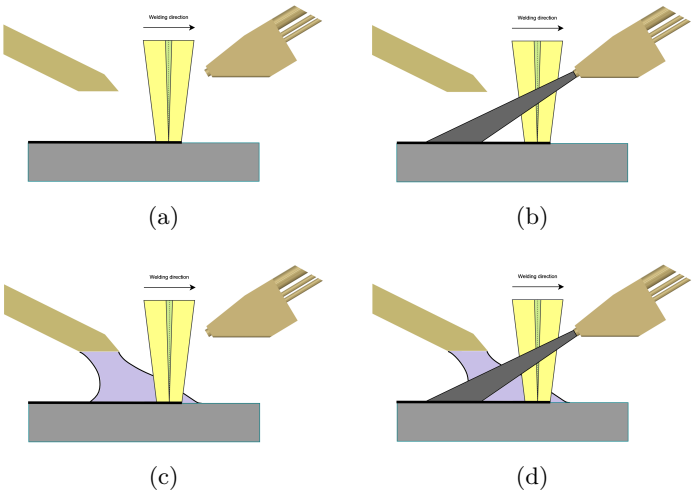

Figure 34: Schematic of laser welding experiments with (a) no powder, no shielding gas, (b) powder, no shielding gas, (c) no powder, shielding gas, (d) powder, shielding gas.

When powder is introduced into the OCT measurement beam, several effects are hypothesized to have an influence on the measurement. These are the following:

- Scattering: Powder particles, corresponding to their shape, are expected to scatter light in various directions. This scattering results in a decreased light intensity reaching the substrate, as a portion of light is diverted away. Additionally, some of the scattered light may be redirected back towards the sensor. These reflections are essentially noise to the measurement, thereby making it more difficult to retrieve the actual height position.
- Absorption: The powder particles might absorb some of the light that would otherwise reach the substrate. The absorption also reduces the intensity of the light reaching the substrate, leading to a weaker interference signal and a decreased SNR value.

Scattering and absorption of light by powder particles contribute to a reduction in the intensity of the OCT measurement beam that strikes the substrate. Consequently, the reflected measurement beam, which interferes with the reference beam, also has decreased intensity. As said, this reduction in intensity might make it more challenging to accurately retrieve the correct height position. Alternatively, if the density of the powder stream is low, the impact of these effects may be minimal, leading to only minor decreases in intensity. This would result in negligible alterations in the SNR values of the points that are measured.

A limitation of the current experiment is that neither the position of the relative height or the angle of powder nozzle with respect to the substrate has been alternated in the experiments. This is significant because the position where the powder stream intersects the laser beam could influence the resulting amounts of scattering and absorption. Specifically, if the powder stream were aimed at the region of the beam where it is focused, the higher light intensity might lead to more pronounced effects of light scattering and absorption. Conversely, powder in the wider, less intense part of the beam would likely have a lesser impact. Thus, the vertical placement of the powder stream could affect the accuracy and interpretation of the measurements by altering the degree of absorption and scattering. Additionally, the powder stream is characterized by a particle density distribution. This is also not considered in this experiment.

The resulting point clouds stemming from the four different experiments were cropped and outliers were removed following the procedure outlined in Chapter 3. 2D representations of the raster scans are displayed in figure 35. To visualize the relative height of the points, a color scaling was applied, where dark blue represents the lowest positioned points and light blue indicates the highest positioned points. The welding direction within the figures can be interpreted as proceeding upwards.

In general, the raster scans presented in figure 35 reveal consistent patterns across all four experiments. Each figure displays a prominent central region, roughly circular in shape, where no points were measured,

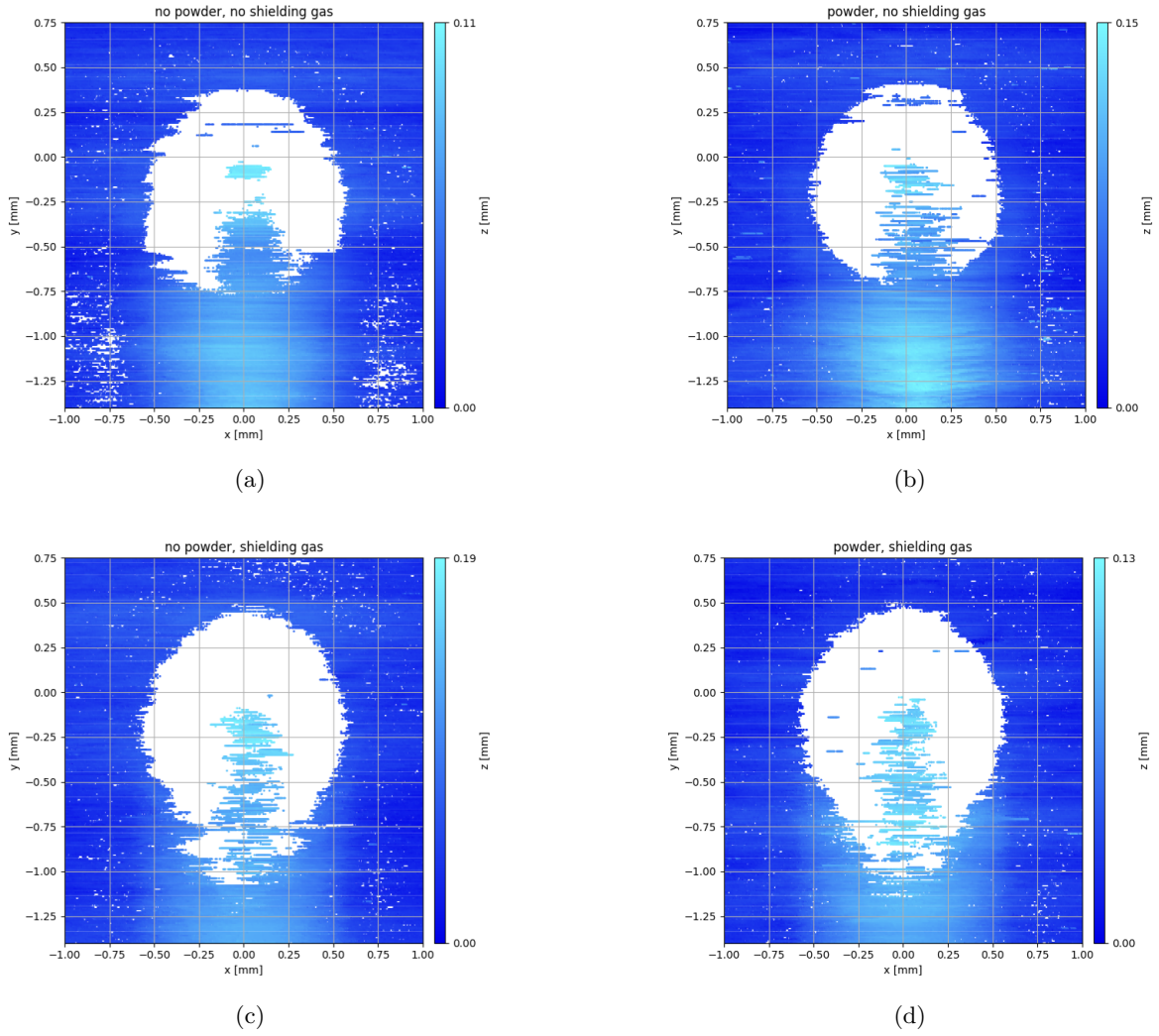

Figure 35: Raster scan made during laser welding utilizing an (b,d) intersecting powder stream and (c,d) shielding gas and (a) neither of both.

resulting in a white area. Despite this, along the x-axis at 0.00 mm (width), measurement points are visible, extending approximately halfway through the circular area. Additionally, near the presumed edges of the track, at approximately -0.75 mm and 0.75 mm (width), as well as above the circular region between 0.50 mm and 0.75 mm on the y-axis (length), there are areas where no points were measured. Each subplot also indicates a slight elevation in the trailing region beyond the white circular area, as shown by the applied color scale. In all figures, the highest relative position is observed along the centerline, nearest to the center of the circular shape.

When comparing figures 35(a) and (b), where no shielding gas is used, with figures 35(c) and (d), where shielding gas is applied, it is evident that the introduction of shielding gas affects the measurement result. The number of unmeasured points increases with the use of shielding gas, and the previously circular shape now more closely resembles a teardrop. These figures also show that the number of unmeasured points along the presumed edges of the track is reduced when shielding gas is applied. This effect is more pronounced in the absence of an intersecting powder stream.

When comparing figures 35(a) and (c), where no powder stream is applied, with figures 35(b) and (d), the impact on the measurements is less pronounced compared to the effect of shielding gas. In the absence of shielding gas, the number of unmeasured points along the track edges is higher when no powder is applied. Furthermore, in figure 35(b), the unmeasured region more closely resembles a neat circle compared to figure 35(a). figures 35(c) and (d) show very similar results, with no significant differences observed.

An explanation for the circular region of unmeasured points is suggested to be as follows: when the laser

beam strikes the surface, the substrate melts due to the laser-induced heating. Molten surfaces exhibit very low surface roughness because surface tension in the liquid phase smooths out irregularities.

As discussed earlier, the OCT system relies on the reflection of light from the surface to take measurements. When the surface is molten, specular reflection dominates, causing most of the incident OCT light to reflect at angles outside the sensor's acceptance cone. Following this explanation, it must be that the area of unmeasured points is slightly inclined, which appears to be the case when looking at the color scale. Specular and diffuse reflections, along with the acceptance cone concept, have already been discussed in Chapter 2. Along the centerline of the x-axis (width), although specular reflections occur, the geometry remains nearly flat, allowing the reflected light to still reach the sensor. The overall explanation for the unmeasured circular region is further supported by the fact that its diameter closely matches the laser's approximate spot size (in focus) of 1.2 mm.

An explanation for the teardrop-shaped region of unmeasured points during laser welding with shielding gas is not yet determined. It is hypothesized, based purely on the OCT measurement, that the shielding gas might extend the melt pool that is created during welding. As a result, the area where measurements are difficult to capture due to specular reflections on inclined surfaces is extended. In the next section, thermal imagery will be used to provide further insight into this phenomenon.

The experiments indicate that the effect of the intersecting powder stream does not significantly impact the measurements. This is because the resulting shape of unmeasured points appears very similar in the different scenarios. However, in the absence of shielding gas, unmeasured points along the edges of the track are observed, and the cause of these missing points remains unexplained. Therefore, further experimentation is necessary to investigate this phenomenon. Overall, it can be concluded that the powder, even at its greatest density used in the actual cladding experiments, does not hinder measurements. The powder particles do not obstruct the OCT measurement beam significantly, as they do not scatter or absorb light to an extent that would weaken the reflection unable to produce a distinguishable interference pattern with the reference beam. Consequently, the OCT system continues to retrieve the relative height position, similar to conditions without the intersecting powder stream.

Thus, two aspects require further analysis based on the posed results. First, an examination of the track is needed to determine the reasons for the missing points along the edges in the absence of shielding gas and without the influence of the intersecting powder stream. Second, thermal imagery may aid in understanding the the teardrop shape of unmeasured points that appears in the OCT measurement when shielding gas is applied.

Non-measured Points

To reproduce the effect of missing or unmeasured points along the edges, the same experiment was repeated as depicted in figure 34(a). Two experiments were conducted, one at 700 W and the other at 1000 W, both at a speed of 5 mm/s. The resulting raster scans are presented in figure 36(a) and (c), where the recurrence of missing data points is clearly visible. Aside from this effect, the figures show a different phenomenon in the point cloud data. That is, entire scan lines are repeatedly omitted at specific positions along the raster scan. It was found that this occurs when the resolution or distance between scan lines drops below a certain threshold. In that case, the galvo scanner appears to skip a scan line. Although this behavior is unexpected, it does not impact the accuracy of the points that are measured and thus does not require further investigation.

To emphasize the region of unmeasured points, the grid of the raster scan, which has a known size and resolution, was analyzed and plots were created to display only the unmeasured points, as shown in figures 36(b), (d). Obviously, for these points, only the grid positions *(x, y)* are known, as the z-values are not measured. Figures 37(a), (b) present overlays of the unmeasured points on a brightfield image of the weld track. In these figures, the unmeasured points from the OCT measurement are positioned at the end of the track. The end position of the track resembles the last position where a melt pool was still existent. As the OCT performs its measurement during processing and takes a few seconds to complete, it is noted that the missing points will not perfectly correspond to this end of the track. Yet, it still makes sense to place the overlay as such as it is the best fit that can be achieved.

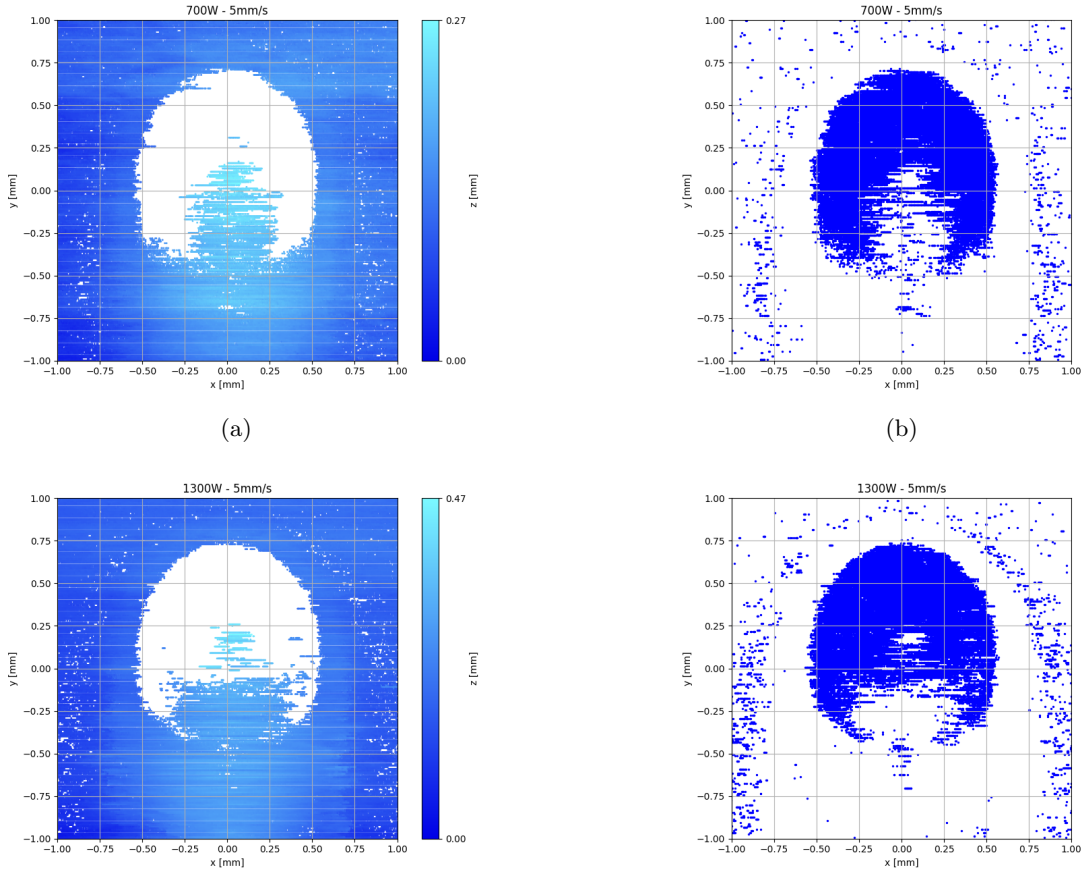

Figure 36: Raster-scan during laser welding at a speed of 5 mm/s at a laser power of (a) 700 W and (c) 1300 W (c). The non measured points of these raster-scans are shown in (b) and (d) respectively.

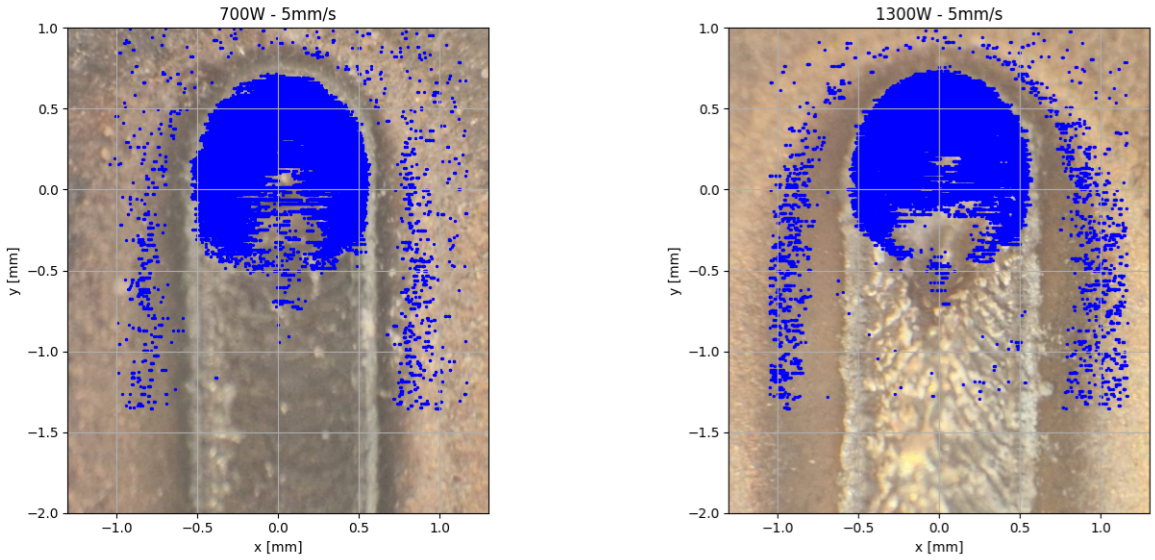

(a) (b)

Figure 37: Overlay of non-measured points during laser welding at (a) 700 W and (b) 1300 W on bright field images of the resulting track.

From the brightfield images, two key observations emerge. First, the approximately circular region of missing points closely matches the actual width of the weld track. Second, the missing points previously labeled as occurring on the sides of the track are, more precisely, not located on the track itself but along the edge of a surrounding black region. This black region indicates oxide formation on the surface, as no shielding gas was applied during the process. At higher power levels, such as 1300 W, this oxidized region is larger compared to the 700 W case. This suggests that the transition between the oxidized surface and the surrounding substrate does not reflect the incident OCT measurement beam.

The link between oxide formation and missing points along the track edges corresponds with earlier findings. In previous experiments where no shielding gas was used, missing points were more frequent, as shown in figure 35(a). However, when a powder stream was introduced without shielding gas, the occurrence of missing points decreased, as shown in figure 35(b). This suggests that the carrier gas from the powder stream may provide partial shielding, reducing oxide formation and potentially explaining the reduction in missing points.

4.2.2 Comparative Analysis of OCT and Thermal Imaging during Laser Welding

The experiments, as shown in figure 34, were repeated to evaluate how well the results from OCT align with thermal imagery. During the process of laying down a 10 cm track, a thermal camera captured images at 60 frames per second, with an exposure time of 10 ms and a gain of 1.0 (effectively no gain). The thermal camera used in the experiments captures pixel intensities with 8-bit resolution, thus ranging from 0 to 255. In the case of laser welding at a laser power of 1000 W and a speed of 10 mm/s, the pixel intensities approached saturation but remained below it. The camera settings were kept consistent for all measurements, ensuring the results from the four different experiments are directly comparable. Thermal images were collected along the entire duration of the welding process.

The OCT raster scan, which took less than two seconds to complete, was manually started about two seconds after the welding began to minimize the impact of start-up effects. As a result, the scan finished roughly four seconds into the welding process. To compare the OCT data with the thermal imagery, a frame from the thermal video was selected at around three seconds into the welding process, ensuring the capture was taken in the same window the OCT system was measuring.

It is important to note that the camera is not a calibrated thermal camera; the pixel intensities are not directly tied to specific temperatures. However, as the temperature rises, the emitted radiation increases, resulting in higher pixel intensities. Pixels with similar intensities represent isothermal regions, with higher intensities corresponding to higher temperatures, although the exact relationship between intensity and temperature is not calibrated.

The 8-bit greyscale captures of the camera are shown in figure 38(a),(c),(e) and (g). The colorized plots, as shown in figure 38(b),(d),(f), and (h), display contour lines, which represent specific pixel intensity levels. These contour lines, following what was just discussed, are representative of isotherms, indicating a line on which temperature is similar. Six different contour lines are drawn in each plot, all set at the same intensity levels across the figures, ensuring direct comparability between the images.

In figure 39, the contour lines from figure 38 are Gaussian-smoothed and overlaid onto the OCT raster scans for the four experiments. These contour lines display normalized intensity values (0 to 1), corresponding to the original 8-bit intensity range (0 to 255). In figures 39(a,b), one contour line is omitted because, after smoothing, the lowest intensity level becomes too small to be clearly represented.

The drawn contour lines in figure 38 reveal a noticeable trend. In cases where an intersecting powder stream is applied, there is a slight reduction in intensity at the center of the circular shaped region, indicated by the reduction of the area enclosed by the two highest level contour lines. This effect is observed consistently, both with and without the application of shielding gas.

In the case where no shielding gas is applied, the lowest level contour line deviates from its circular shape, extending slightly in the negative y-direction. This distortion is consistent whether or not an intersecting powder stream is present. The effect of shielding gas on the intensity within the higher-level contour lines is less pronounced, as there is no clear difference in the areas they encapsulate.

Summarizing, the shape of the contour lines remains relatively unchanged with the application of the intersecting powder stream, although a slight decrease of the encapsulated area within the higher level contour lines is observed. Conversely, the introduction of shielding gas significantly modifies the shape of the lower level contour lines, resulting in a more circular region enclosed by them.

The plots in figure 39, displaying the smoothed contour lines overlaid on the OCT raster scan, reveal that in the case of shielding gas applied, in figures 39(c),(d), the unmeasured circular region is most closely represented by the 0.16 normalized contour line value. When no shielding gas is applied, this region corresponds more closely to the 0.22 value in figure 39(a), and falls between 0.16 and 0.22 in figure 39(b).

Additionally, something unexpected is now clearly seen. That is, from just the OCT measurements it is suggested that the melt pool is elongated upon using additional shielding gas, yet the thermal images suggest the occurrence of an opposite effect. From just the thermal images it appears as if the melt pool must be shorter in length when no shielding gas is applied. From just these results, it is not clear what happens here.

As seen in figure 37, and also visible in figure 35, the width of the region of unmeasured points in the OCT scan remains relatively consistent, which is found to be just a little over 1 mm in size. However, based on the results from figure 39, the isotherm corresponding to this unmeasured region is not the same across all experiments. If the unmeasured area is aligned with the melt pool boundary, it is expected to see the same level contour line, representing the liquidus or solidus temperature, around the edge of the unmeasured region, across the different experiments. This is not the case. The isotherm that best fits this area varies between experiments, this suggests that the unmeasured region in these experiments can not be confirmed to represent the melt pool.

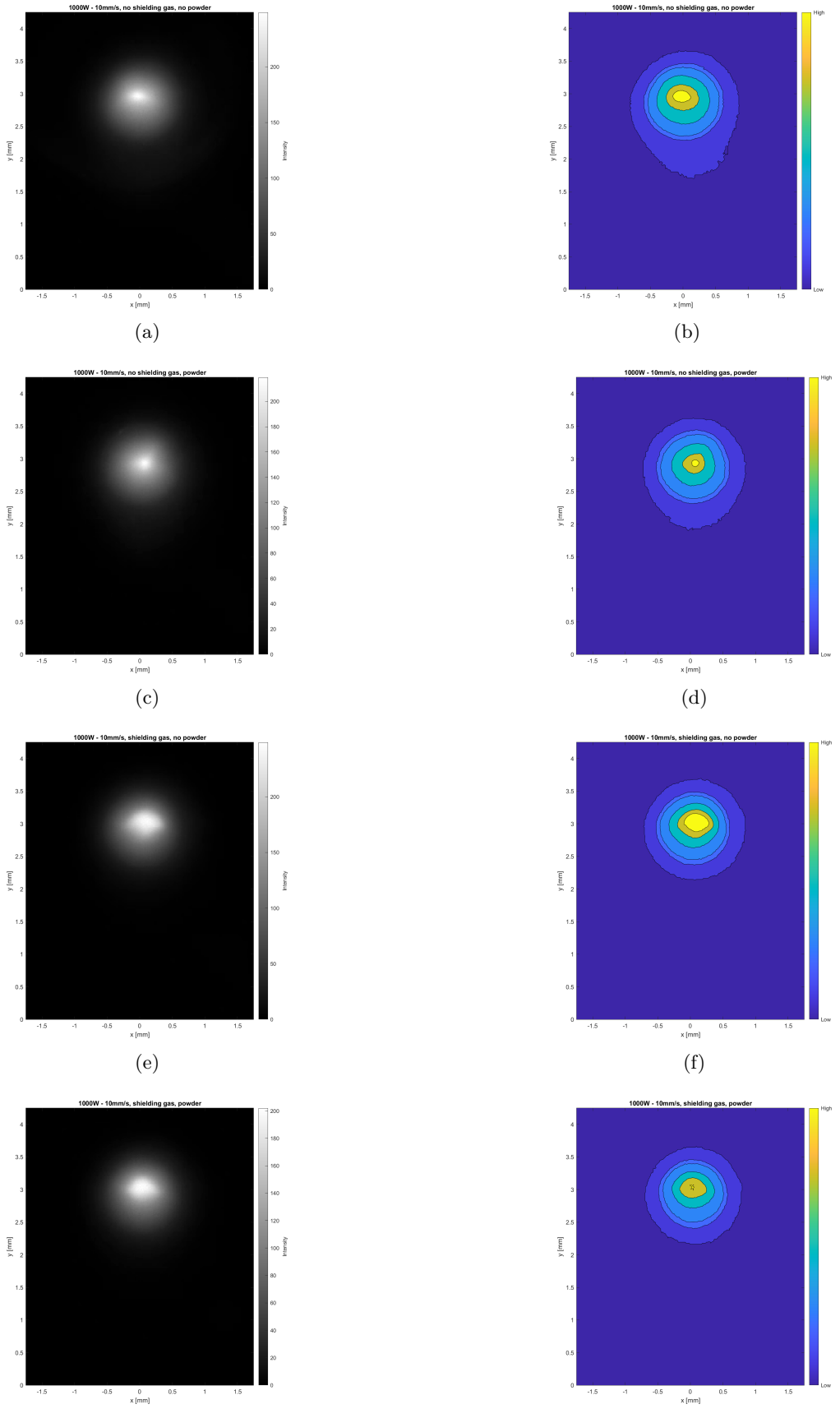

(a) (b) (c) (d) (e) (f) (g) (h)

Figure 38: Greyscale E-MAqS snapshots and their corresponding contour lines, using (a,b) no shielding gas, no powder, (c,d) no shielding gas, powder, (e,f) shielding gas, no powder, (g,h) shielding gas, powder.

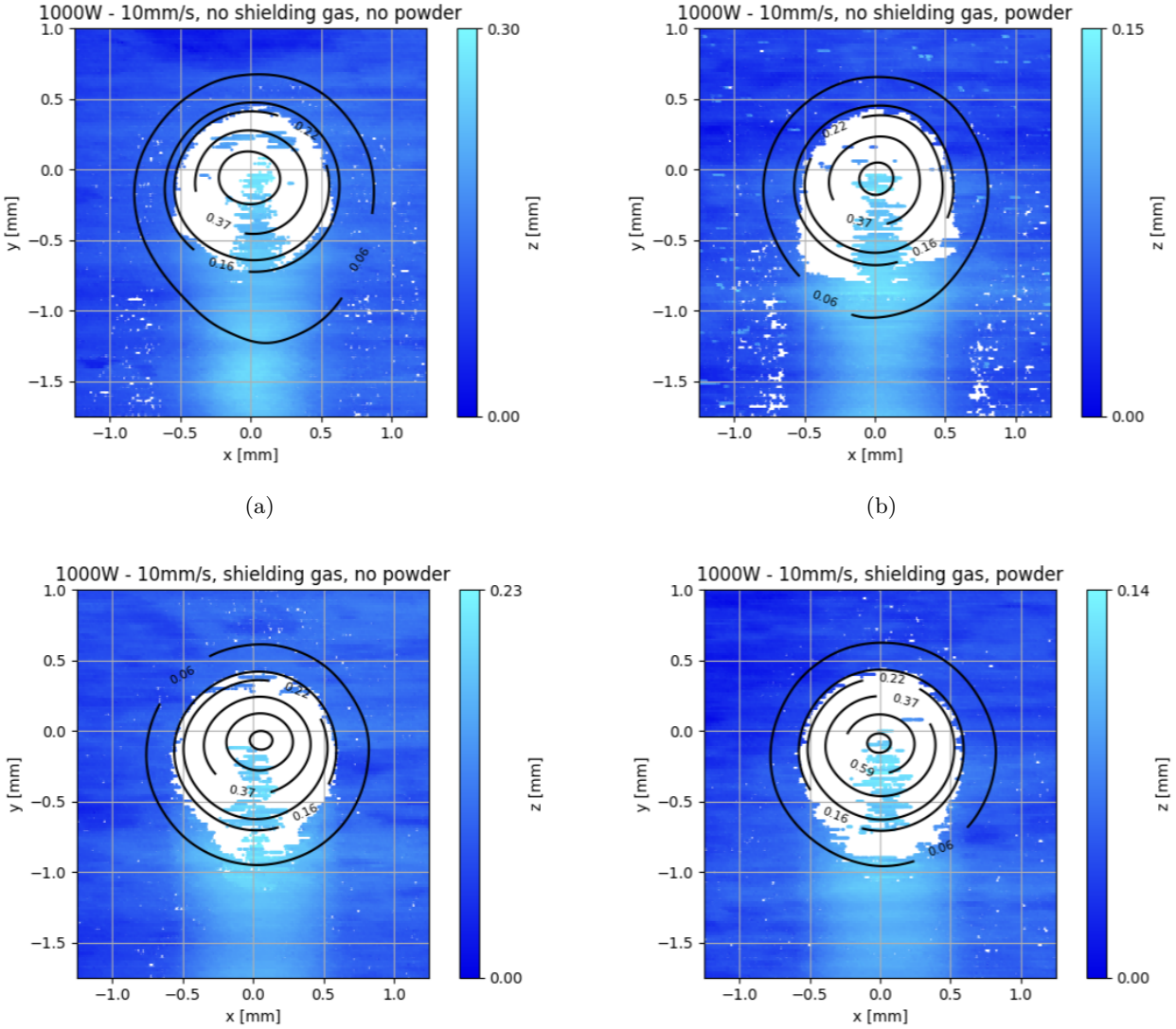

Figure 39: Overlay of Gaussian smoothed contour lines on raster scan made during laser welding at a laser power 1000 W and a speed of 10 mm/s employing (a) no shielding gas, no powder, (b) no shielding gas, powder, (c) shielding gas, no powder, (d) shielding gas, powder.

Laser Cladding

After evaluating the effects of shielding gas and intersecting powder streams in the simpler conductive laser welding environment, the focus now shifts to in-situ OCT measurements in a laser cladding setup. A procedure similar to that used in laser welding is followed, where a raster scan is initiated approximately two seconds after the process begins, to mitigate start-up effects. The OCT raster scan is then manually activated using the LLT Software. The measurement concludes multiple seconds before reaching the end of the clad track. Initially, solely the OCT measurements will be analyzed. In the subsequent section, the OCT measurement will also be compared with thermal imagery. Throughout all upcoming experiments, the powder feed rate injected into the melt pool is kept constant at 4.8 g/min.

4.2.3 Assessment of OCT measurement during Laser Cladding

Figure 40 shows the OCT measurement taken during laser cladding at a laser power 1100 W and a speed 5 mm/s. The measurement was obtained by vertically moving horizontal scan lines. The raster was performed in a negative y-direction, with horizontal scan lines consisting of 900 points spaced over 3 mm. The vertical spacing between scan lines was 0.02 mm, covering a vertical length of 5 mm. In total, 250 horizontal lines are measured, resulting in 225,000 measurement points in the resulting point cloud. The entire measurement process took a little over three seconds to complete.

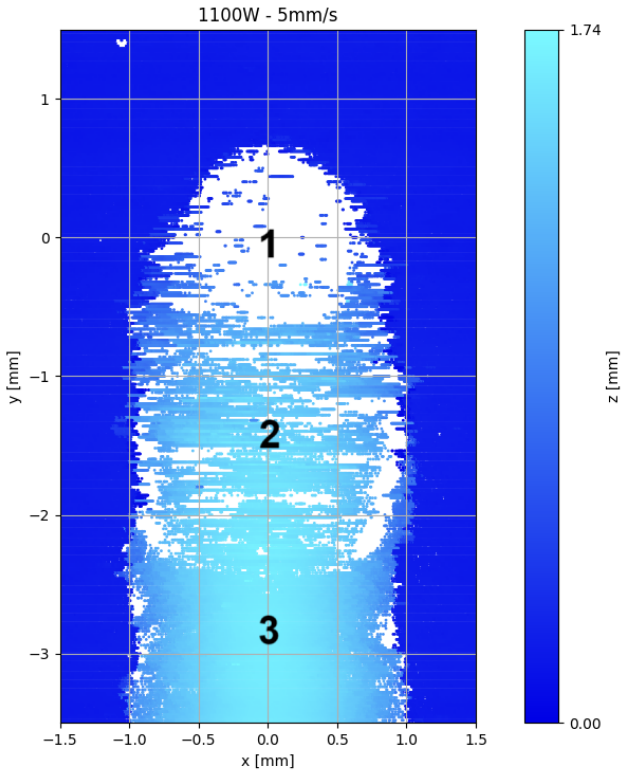

Figure 40: Point cloud obtained from the raster scan during laser cladding at a laser power of 1100 W and speed of 5 mm/s, indicative of three visually distinguishable zones by point cloud density.

When examining the image of the point cloud in figure 40, three distinct zones can be visually distinguished, each characterized by the density of the measurement points within these areas, these are marked as Zone 1, Zone 2 and Zone 3. In the top view, certain characteristics of the zones become visible. The transition from Zone 1 to Zone 2 appears to have a sharply defined boundary. In contrast, the transition from Zone 2 into Zone 3, particularly along the center of the track is more difficult to pinpoint. Whereas at the sides of the track, the boundary is again characterized by a distinct and sharply visible boundary.

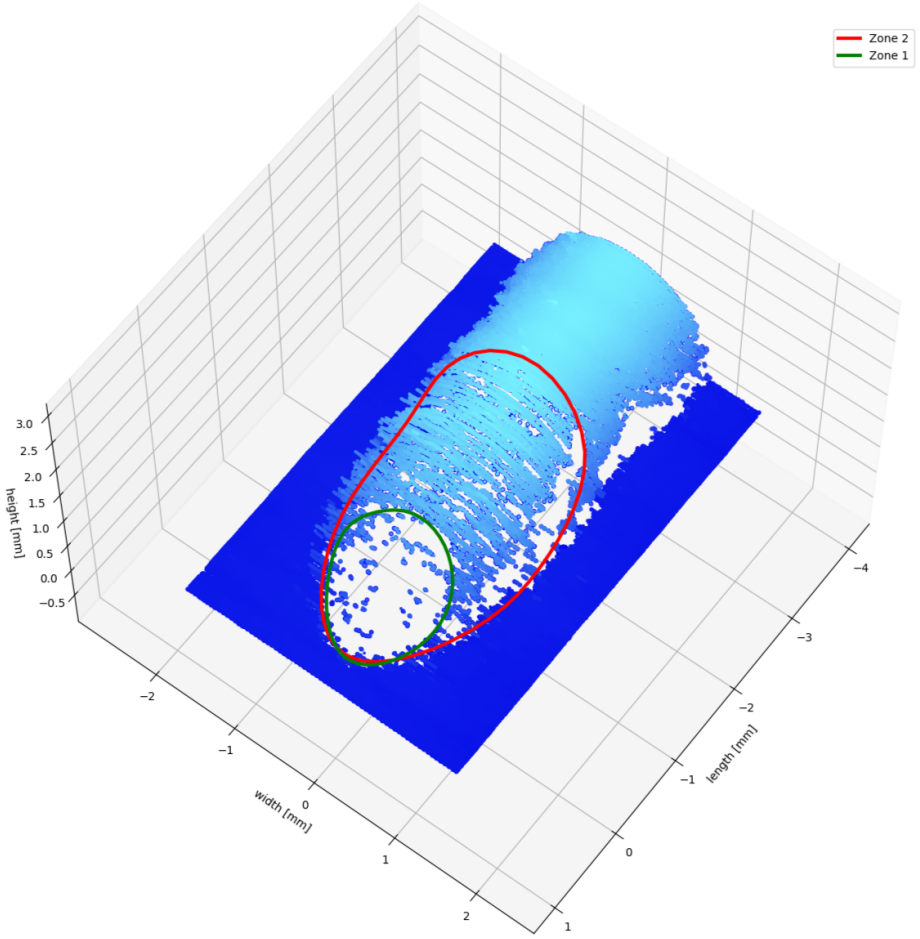

Figure 41: OCT measurement made during cladding at a laser power of 1100 W and a speed of 5 mm/s indicative of visually distinguishable zones by means of point density.

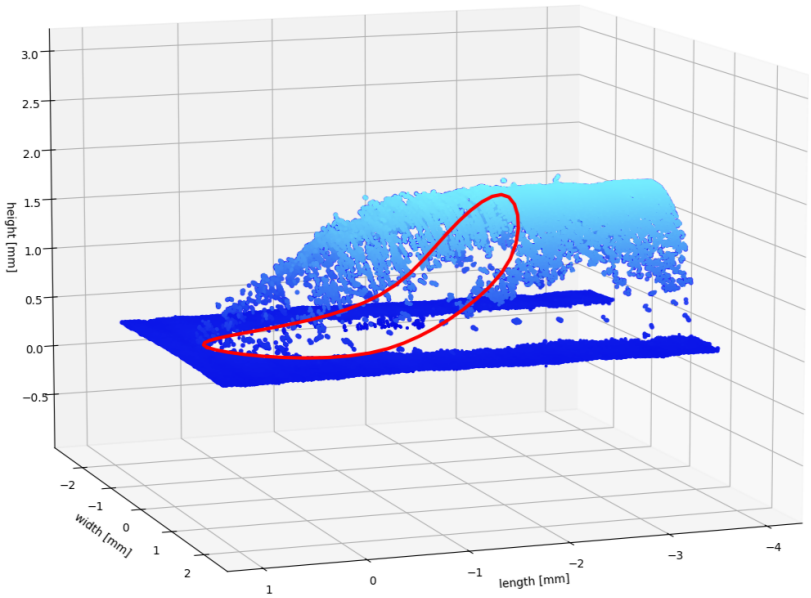

Figure 42: OCT measurement during cladding at a laser power of 1100 W and a speed 5 mm/s indicative of zone 2.

Figures 41 and 42 attempt to visualize and define the boundaries of these distinct zones more clearly. These figures specifically highlight the boundary of Zone 1 and Zone 2. Zone 2 is defined as an area that encompasses Zone 1, but when referencing to Zone 2, it refers to the region that excludes Zone 1 itself, which is effectively the outer portion surrounding Zone 1. The size of Zone 1 is found to closely resemble the approximate spot size of the processing beam. Zone 3, while not explicitly marked, covers the remaining trailing section of the track, located in the lower region along the vertical axis and not included in Zone 1 or Zone 2. This was achieved by fitting a B-spline curve through points manually identified as lying on the boundary. Despite numerous efforts to systematically pinpoint the boundary points using scripts, the resulting scripts were insufficiently accurate, falling short of the clarity that is visually distinguishable in the measurements.

The total time to complete this single raster scan, as stated before, is approximately 3 seconds, with the optical head moving at a speed of 5 mm/s. Consequently, the measurement covers a distance of 15 mm along the clad track. Hence, it is important to note that this measurement is not a true snapshot of the melt pool and its surrounding region. Instead, the data reflects changes occurring over the 3-second scan duration. For example, variations in the melt pool size and shape due to process fluctuations as a result of flow of material in the melt pool during the cladding process.

The observation of visually distinguishable zones based on point cloud density is confirmed by the data in table 4. Zone 1 exhibits the lowest point density, while Zone 2 shows more than an 8-fold increase in density compared to Zone 1. In Zone 3, the point density is nearly 1.5 times higher than that of Zone 2, further highlighting the variation across the zones.

	Area [mm^2]	**Amount of points**	**Point density [Points / mm^2]**
Zone 1	1,20	962	802
Zone 2	3,82	26266	6876
Zone 3	3,67	37683	10268

Table 4: Point density in different zones presented as point per mm^2

In summary, the measurements reveal the presence of three distinct zones, where the transitions from Zone 1 to Zone 2 and from Zone 2 to Zone 3 are clearly distinguishable. Additionally, the size of Zone 1 aligns closely with the approximate spot size of the focused processing laser beam. To further explore the reasons behind the formation of these zones, the next section will incorporate thermal imaging to compare with the OCT results, as an attempt to enhance our understanding of these zones.

4.2.4 Comparative Analysis of OCT and Thermal Imaging during Laser Cladding

To enhance the understanding of the in-situ OCT measurements in laser cladding, further experiments are conducted using the same DoE as outlined in table 3. Similar to the welding experiments, both the thermal camera and OCT are used simultaneously in the setup. Although a comparable procedure is followed, the camera settings are adjusted for these experiments. An exposure time of 16.7 ms and a gain of 3.0 is applied. To ensure comparability among all thermal captures, this is the same for all the cladding experiments. However, due to the differences in camera settings compared to the welding experiments, direct comparisons cannot be made with those results. As with the welding experiments, the cladding direction is interpreted as moving upward, or in the positive y-direction.

The 8-bit greyscale captures from the thermal camera are presented in figure 43(a), (c), (e), recorded during cladding at various power levels with a cladding speed of 5 mm/s. Figure 44(a), (c), (e) display similar captures at different power levels but with a cladding speed of 10 mm/s. The colorized plots in figure 43(b), (d), (f) and figure 44(b), (d), (f) illustrate the corresponding contour lines, which again represent isotherms. The contour lines are drawn at equal levels across all figures, thus ensuring comparability. In figure 45, following the approach used in the laser welding experiments, smoothed contour lines are overlaid onto the top view of the raster scans from the various laser cladding experiments. Smoothed contour lines are obtained by replacing each pixel in the image with a weighted average of its neighboring pixels, where the weights are determined by a Gaussian function. The parameter σ directly controls the spread of this function, with larger σ values causing the function to cover a wider area, incorporating more neighbors and ultimately producing smoother contour lines.

The exposure and gain settings for the thermal camera are optimized to ensure clarity in the captured frames. In all greyscale images from figures 43 and 44, a trailing region is visible just behind a nearly circular white spot. To enhance the visibility of this trailing region, a high exposure is used, and gain is applied to further increase the pixel brightness. These settings are adjusted to ensure that even the dimmest trailing region, such as in figure 44(a), remains clearly visible. However, this results in a large, fully white area in the greyscale capture, indicating pixel saturation. As a consequence, isotherms within this saturated region cannot be distinguished.

A clear trend emerges from the thermal images in both figure 43 and figure 44. As laser power increases, the size of the saturated pixel region expands. Simultaneously, the length of the trailing region, marked by increased pixel intensity, extends in the negative y-direction with higher power levels. This trend is visible in the greyscale images, but becomes even more pronounced in the corresponding colorized contour plots. Additionally, the width of this trailing region increases with power in both the 5 mm/s and 10 mm/s experiments.

The scan speed also significantly affects the trailing region's characteristics. At a lower speed of 5 mm/s, the trailing region becomes notably wider compared to the images captured at 10 mm/s. Similarly, at a laser power of 700 W, the size of the central saturated white spot appears to be influenced by speed, with a slower scan speed producing a larger bright white spots. However, this effect is not seen at higher laser powers.

When examining the OCT measurements from figure 45, several trends emerge in the resulting clad tracks. The width of the clad track increases with higher power and slower scan speeds. Also the height of the clad tracks, indicated by the maximum value on the color scale, is found to increase very slightly with higher power levels and a lot with slower scan speeds. The size and shape of the unmeasured region, referred to as Zone 1, remains fairly consistent across all figures, measuring just over 1 mm in width. This closely aligns with the approximate spot size of the processing beam used in the experiments. An exception is seen in figure 45(b), where Zone 1 is less distinguishable due to the unclear boundary between Zone 1 and Zone 2. However, the width of Zone 1 still appears consistent with that observed in the other experiments. The length of Zone 2, represented along the y-axis, increases with higher laser power, while its width (x-axis) also expands. Higher scan speeds, however, reduce the length of Zone 2, a trend consistent across all power levels.

Additionally, point density within the zones varies between experiments. As laser power increases, fewer points are measured, particularly in Zone 1. This effect is less pronounced in Zone 2. Increased cladding speed leads to more points being captured in Zone 1, especially at 700 W and 1000 W. Whereas at 1300 W, the point density in Zone 1 does not appears to change much. At 700 W, figures 45(a), (b) show that the boundary of Zone 1, the area with missing points, is most closely represented by the contour line at a normalized level of 0.63. At 1000 W, figures 45(c), (d), this same area shifts to a higher contour

level, around 0.78. Finally at 1300 W, figures 45(e), (f), the unmeasured region is associated with an even higher contour level of 0.96, approaching pixel saturation.

The transition from Zone 2 to Zone 3 is most distinct at 1300 W and 5 mm/s, and remains clearly visible at 1000 W for both 5 mm/s and 10 mm/s. However, at 700 W, this transition is less defined at both speeds, making it more challenging to pinpoint. At 700 W, the boundary between Zone 2 and Zone 3 varies with scan speed, being found slightly above the 0.13 contour line at 5 mm/s, while at 10 mm/s, it lies between normalized values of 0.08 and 0.13. At 1000 W, this boundary is similarly located at around 0.13 for 5 mm/s and close to 0.08 for 10 mm/s. At 1300 W, the transition appears again at approximately 0.13 for 5 mm/s and between 0.13 and 0.08 for 10 mm/s. Also, it is observed that the contour line at a value of 0.13, rises slightly in +y-direction around the center of the x-axis. This effect is visible in the experiments that use cladding speed of 5 mm/s but is not present in the experiments that use a cladding speed of 10 mm/s.

Across experiments with varying power levels, the contour line corresponding to the unmeasured region Zone 1 differs slightly, indicating that this zone cannot represent the melt pool. If it did, the same contour level would approximately match this region in all experiments. Instead, the size and shape of the unmeasured Zone 1 are more closely aligned with the spot size of the processing beam (in focus), as noted earlier.

The measurements indicate that point densities in Zone 1 vary across experiments, with fewer points recorded at higher power levels and slower cladding speeds. The latter can be explained as follows, as the resulting height of the cladded tracks is greater for slower scan speeds but the size of Zone 1 remains the same, the surface inclination along the y-direction in Zone 1 is assumed to be steeper in these cases. This would lead to more specular reflections that do not return to the sensor.

However, this explanation does not hold for the same effect that is observed with increasing laser powers. As for solely increasing the laser power, the observed clad track height is not changing much. Hence, the surface inclination in Zone 1 along the y-direction is expected to not change much either. From these results, it does not become clear why the decreased point density in Zone 1 appears with increasing laser power.

Across experiments, the transition from Zone 2 to Zone 3 is approximately resembled by a small range of lower-level contour lines, indicating a region that has an elevated temperature and continues to radiate with greater intensity as compared to the trailing region. This pattern is consistent across all measurements, where contour levels ranging from 0.08 to 0.13 correspond to the transition between Zone 2 and Zone 3.

Finding a single thermal image that corresponds perfectly to the OCT measurement is not possible, as the OCT system completes the raster scan measurement over a three second period. When capturing snapshots from the thermal camera at different times, the appearance of the bright spot and the trailing region may vary, appearing slightly longer, wider, or brighter. While these changes are minimal, they are expected to contribute to the observed deviations of the contour lines from the OCT measurements.

Previously, it has been suggested that the melt pool reflects the OCT beam specularly due to its smooth surface, a result of surface tension effects in the molten state. As a result, points are not measured. Within Zone 2, it is observed that most points are measured along the center of the track. This is attributed to the surface exhibiting an almost flat surface along the center. Moving away from the center of the track, considering the clad track exhibits a parabola-like shape, the surface becomes more and more inclined, thereby yielding more specular reflections outside of the acceptance cone.

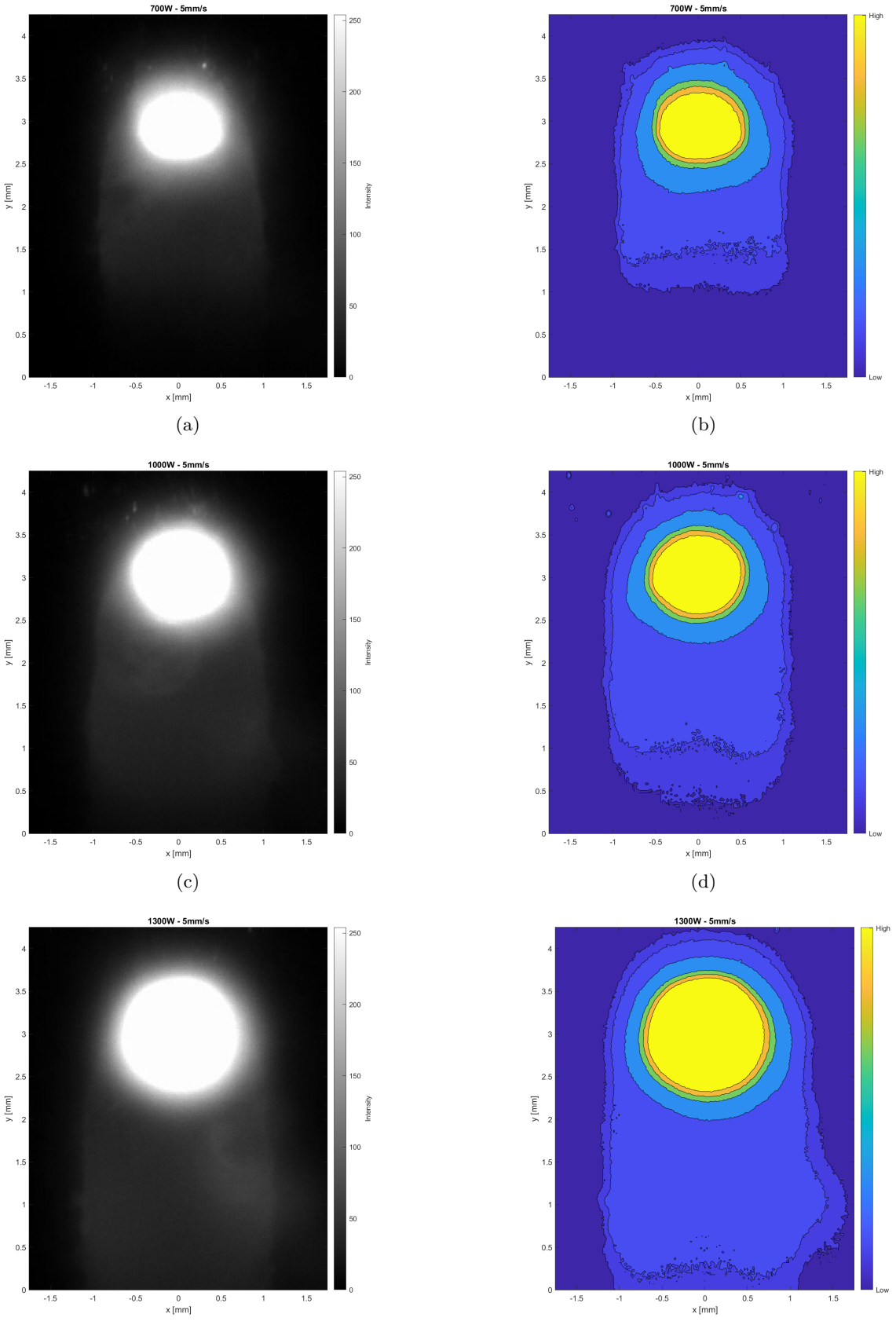

Figure 43: Greyscale E-MAqS snapshots during laser cladding at a speed of 5 mm/s and their corresponding contour lines at a laser power of (a,b) 700 W, (c,d) 1000 W, (e,f) 1300 W.

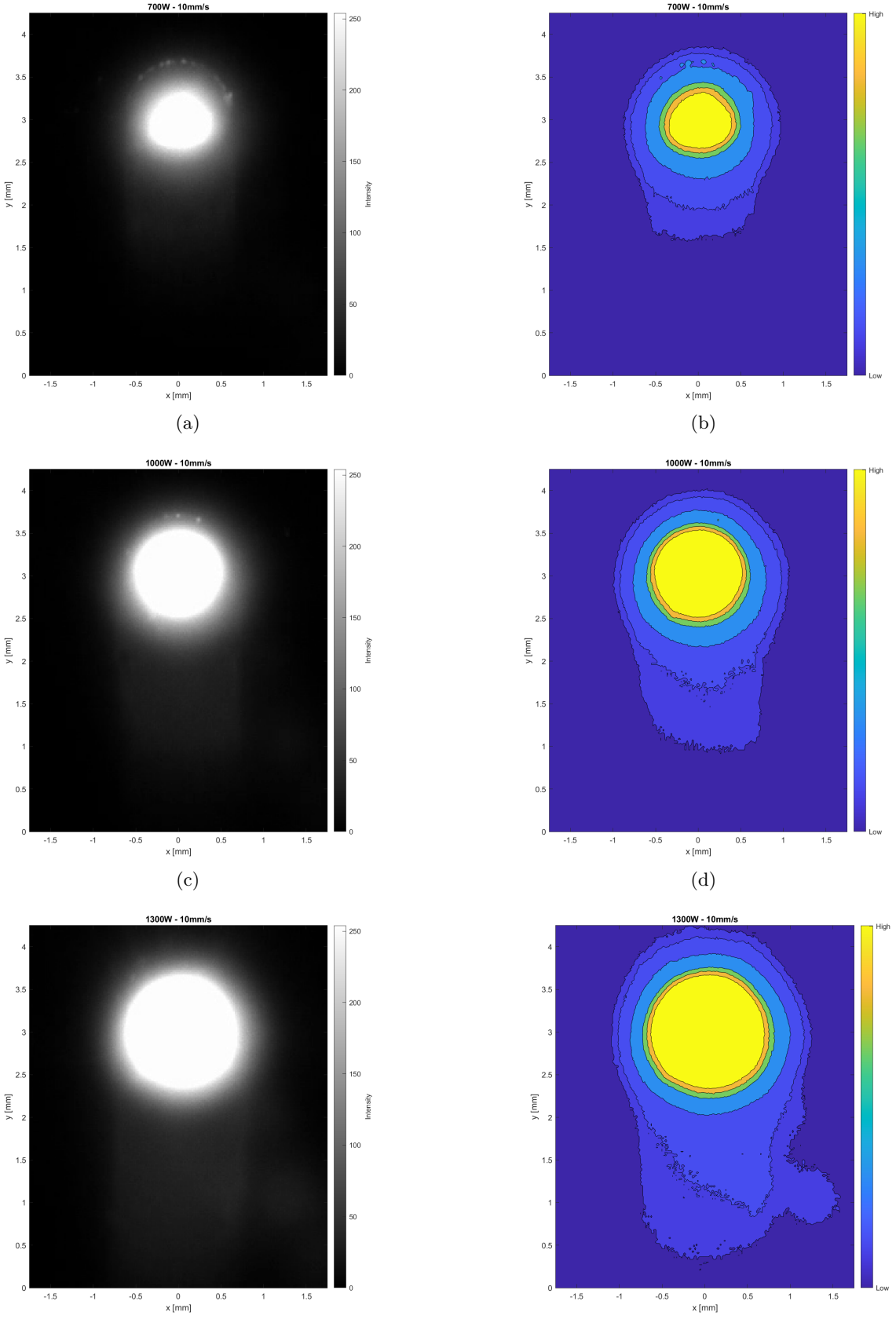

Figure 44: Greyscale E-MAqS snapshots during laser cladding at a speed of 10 mm/s and their corresponding contour lines at a laser power of (a,b) 700 W, (c,d) 1000 W, (e,f) 1300 W.

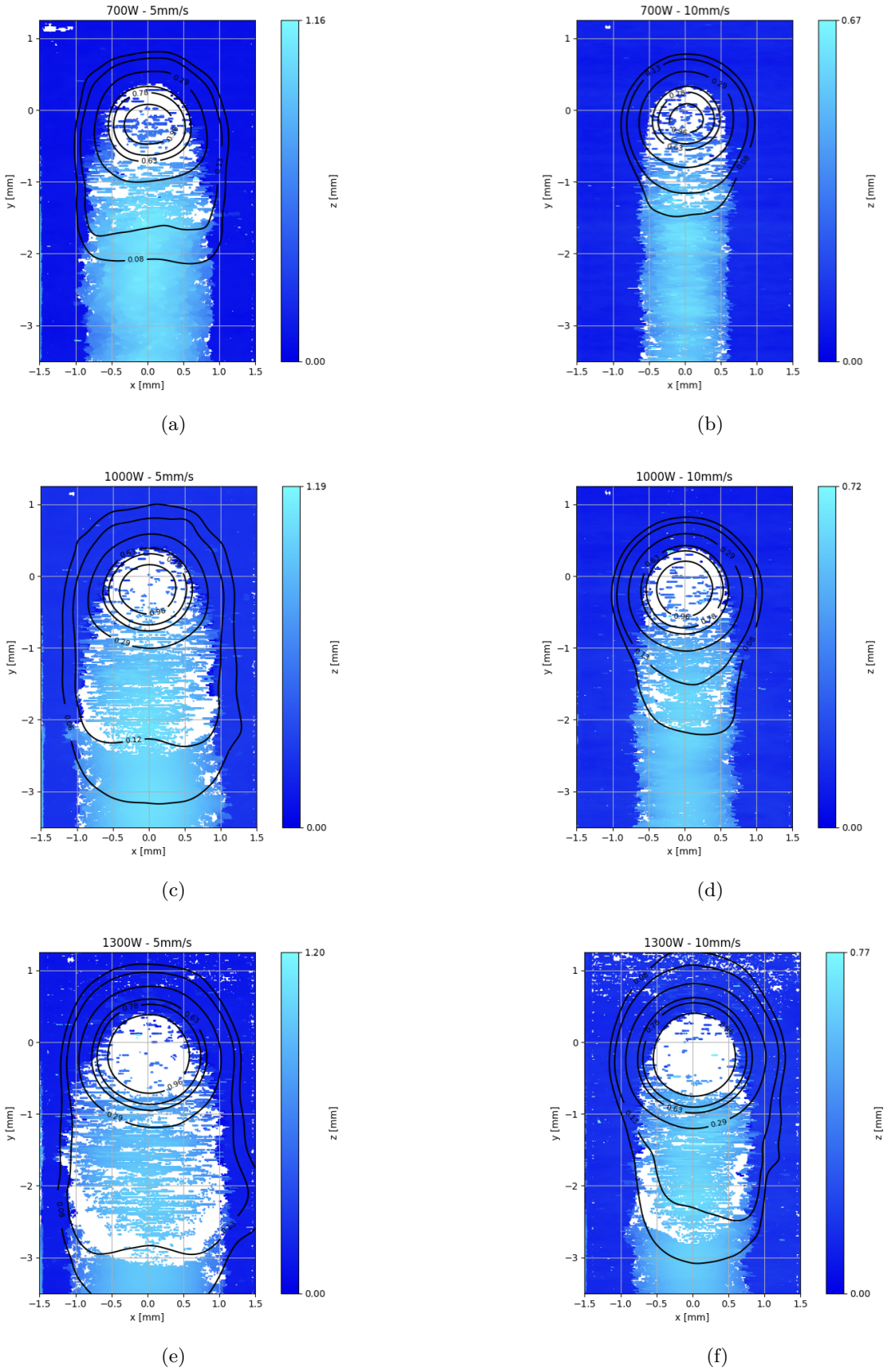

(a) (b) (c) (d) (e) (f)

Figure 45: Overlay of Gaussian smoothed contour lines on a raster scan made during laser cladding conducted at various power levels of (a,b) 700 W, (c,d) 1000 W, and (e,f) 1300 W at a speed of (a,c,e) 5 mm/s and (b,d,f) 10 mm/s.

4.2.5 Process Fluctuations

This section explores the fluctuations inherent to the laser cladding process, as obtained in the measurements from the E-MAqS camera. Despite visible similarities in figure 45 between the OCT measurement and the thermal image, a significant deviation is seen between the different contour lines and the OCT measurement. It is suggestive of non-steady behavior of the process over time.

To quantify the process fluctuations, the coaxial video captured using the E-MAqS camera was analyzed. Building on previous results, a tool was developed using python, as displayed in figure 46(a) to visualize the contour lines at specified pixel intensity levels for each frame of the video. The areas that are encapsulated with the contour lines are chosen such that they to some extent resemble the different zones that were identified in the OCT measurement. The number of pixels encapsulated within these contours then serves as the area size. By computing this area for every frame, a representation over a three second duration of processing was generated, as shown in figure 46(b).

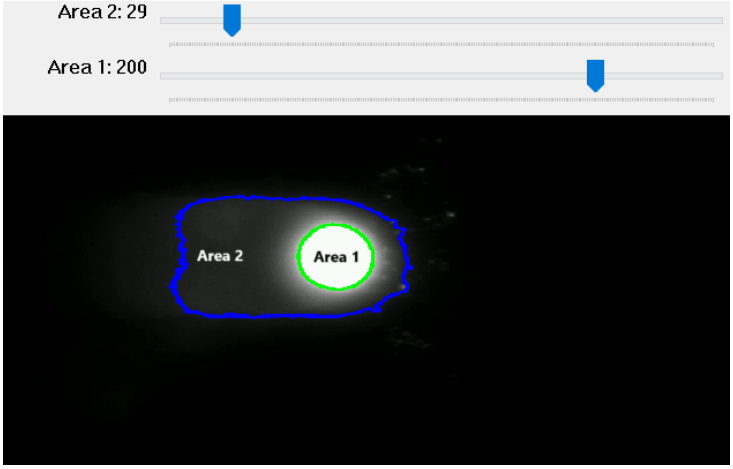

(a)

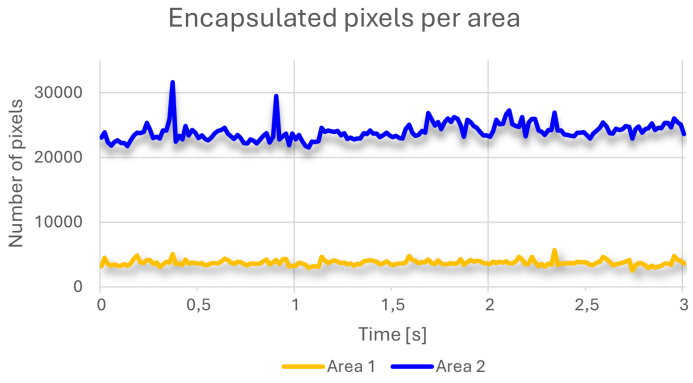

(b)

Figure 46: (a) E-MAqS video analysis and (b) resulting encapsulated pixels per area over time.

The results in figure 46 reveal that the cladding process is in fact characterized by (thermal) fluctuations. The mean absolute deviation from the mean area encapsulated by the lower level contour line, indicated as area 2, is roughly 8%. For the higher level contour line, area 1, this is slightly over 4%. These fluctuations help to explain the observed deviations of the thermal image and the OCT measurement. The latter is captured in a approximately three second duration while the thermal image merely represents a single snapshot of the process at a certain time. Consequently, the (thermally) dynamic nature of the cladding process results in the OCT measurements not being directly comparable to the thermal capture.

4.2.6 Reconstructing Surface using Interpolation

Despite the sparse data in Zone 1 and the incomplete measurements in Zone 2, the available data can be leveraged to approximate the missing points and estimate the surface in these regions. Thereby making use of a surface reconstruction technique, that is interpolation using a radial basis kernel function. The purpose of applying interpolation to the incomplete dataset is to approximate the measurement in the different zones at points where direct measurements were failed to acquire. By utilizing the surrounding data points, the surface is estimated, providing a continuous representation of surface that offers insight into the shape of this region. Obviously, this approach is not replacement of actual measurements.

An attempt was made to reconstruct the surface from the OCT measurement points by fitting an interpolated surface. Radial Basis Function (RBF) surface plotting was employed using a Quintic radial basis kernel function.

The quintic radial basis kernel function used is defined as:

$$\phi(r) = -r^5 \tag{16}$$

ϕ represents how the weight of the z-value of a known data point in the interpolation rapidly decays with distance as you move further away from the position for which you are interpolating. Here r represents the (absolute) Euclidean distance between the position for which a z-value is estimated and actual measurement points. Additionally also a smoothing parameter is introduced that acts as maximum distance a known measurement point may deviate from the interpolated surface. A higher smoothing parameter results in a smoother surface.

Figure 47(a) and (b) present only the part of the reconstructed surface, made using the quintic kernel function, within the bounds of the previously defined zones, providing a visual representation of the surface characteristics in these regions.

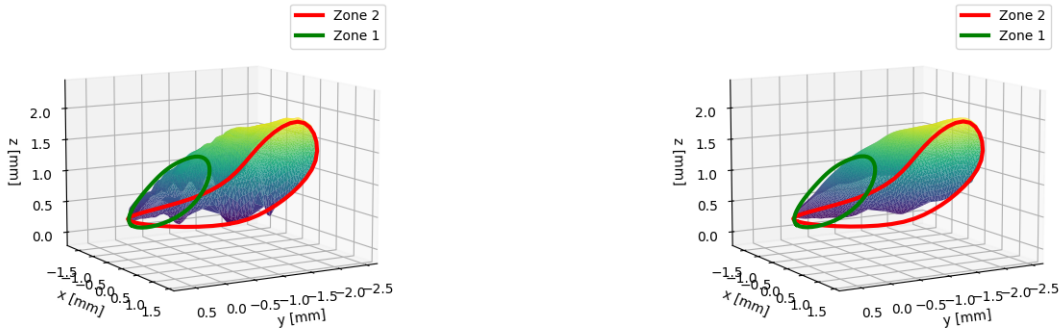

(a) (b)

Figure 47: Interpolated surface using mulitquadric kernel function, (a) non-smoothed, (b) smoothed.

The results presented in figure 47 reveal distinct variations in surface inclination across the defined zones. Within Zone 1, along the center of the melt pool ($x = 0$), the surface exhibits an approximately linear inclination in negative y-direction. Beyond the boundary of Zone 1 a similar inclination is seen for a short distance. Thus, after Zone 1 the height keeps increasing along the negative y-direction. It appears to already reach an approximate maximum slightly before the end of Zone 2. Ultimately reaching a maximum height as Zone 2 progresses into the region beyond, not visible in this figure. When comparing figure 47(a) and (b) it becomes apparent that the ongoing rise of height along the y-axis, beyond the boundary of Zone 1, is apparent in both the smoothed and non-smoothed interpolated surface, thereby ensuring this effect is not solely caused by the smoothing of the surface.

5 Discussion

In this study, the deployed OCT system effectively captured (ex-situ) the surface geometry of the clad tracks to such an extent that distinguishable profiles that correspond to variations in process parameters have been revealed. However, the axial resolution of 12 µm is insufficient for measuring exact surface roughness. It does however remain adequate for detecting the waviness and form of the clad surface.

The results, from comparing with confocal microscopy (section 4.1.2), are indicative of a limitation in the OCT's ability to accurately measure the surface topography at the edges of the track. This limitation manifests as missing data points as well reduced accuracy as compared to confocal microscopy. That is, points that are measured at the steep edges of the track exhibit increased RMSE values. Relating the RMSE values to the used processing parameters proved to be difficult, as the sections that contain the start-up effects of the process were compared. It was found that the geometry of this part of the track is not representative of the more stable geometry of the clad track further along this same track. That is because the aspect ratio was found to fluctuate along the first section of the track. Yet, it still makes sense to do the comparison on this part of the track, as it ensures that the registering of the OCT point cloud to the confocal microscopy point cloud belongs to the same portion of the clad track. Larger point clouds that also contain a part of the stable geometry could have been used. However, further increasing the size of the point cloud resulted in repeatedly crashing the software, as it exceeded available memory.

Previous literature established the concept of the acceptance cone, within which reflections from an angled surface must fall in order for the OCT to capture the signal [50]. Reflections falling outside this cone inherently result in missing data points. It is revealed that similar effects are present in the results from this research. It is shown that diffuse reflections, arising from the roughness of the surface of the solidified deposit, encounter similar limitations at the edges of the track (section 4.1.1). Here, much of the diffusely reflected light, is reflected beyond the acceptance cone. As a result, either the SNR is reduced or no point is measured at all.

The OCT measurement beam, having a diameter of 90 µm (in focus), covers about 5 to 10 % of the clad track's width while trying to measure the height of only a single point. Following this, the surface measured by the OCT probing beam cannot be considered to exhibit a constant surface inclination. Considering this, measuring the height at the correct position is even more challenging. To understand this, first consider the scenario where the surface inclination is perfectly constant and the roughness is uniform. In that case, the highest intensity reflection is obtained from the center of the beam, as this is where the surface was irradiated with the greatest intensity of the probing beam. Hence, the height is retrieved at the correct position. Now consider the scenario where the surface inclination is changing within the area irradiated by the OCT measurement beam, as on the sides of a clad track. In this scenario, a larger part of the incident light is reflected back into the acceptance cone from the part of the surface that has a less steep incline. Even though the largest intensity is hitting the surface at the position where it is trying to measure, it does not mean this yields the largest reflection as well. Because the same measurement beam simultaneously also hits a surface that is less inclined and returns more of the incident light back into the system. An attempt to visualize this effect is shown in figure 48. The resulting effect in the OCT image, also visible in the point cloud, is referred to as a stepping effect, as shown in figure 49.

Additionally, the situation becomes even more complex when considering that the beam is converging up until the height of the substrate. This is relevant because at the edges of a clad track different parts of the measurement beam strike at significantly different heights. This means that the intensity distribution of the beam is different for the different height positions that are simultaneously irradiated by the beam when measuring a single point. Add to this that the convergence of the beam is characterized by an astigmatism. In the end, it is assumed that this will have negligible effect on the resulting measurement. As the different heights irradiated by the beam, at the very steep surfaces at the edge of the track, will still be relatively close to each other, in the order of at most a few hundred m.

The underlying hypothesis for applying OCT in a laser cladding environment is based on the effect of nearly specular reflections from smooth surfaces. It is expected that the melt pool created during laser cladding exhibits significant smoothness, resulting in strong nearly specular reflections of the OCT measurement beam. However, this strong signal is only picked up on if the reflected beam remains within the acceptance cone. Thus, the OCT encounters a problem whenever it tries to measure a smooth inclined surface. This results in specular reflections beyond the numerical aperture of the OCT system. Thus, this study aimed to determine whether this effect can be leveraged to gain a more detailed understanding

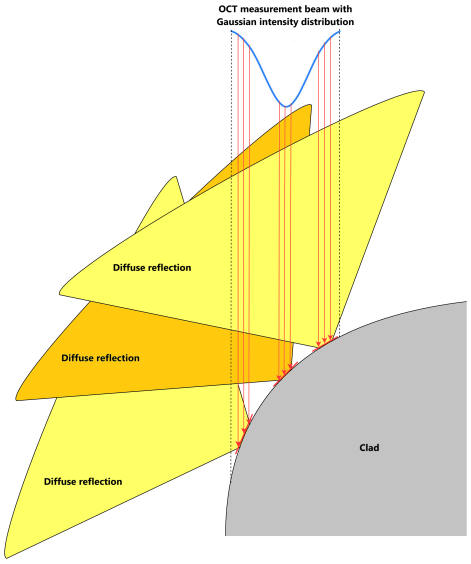

Figure 48: Simplified schematic overview of diffuse reflections on different surface inclinations.

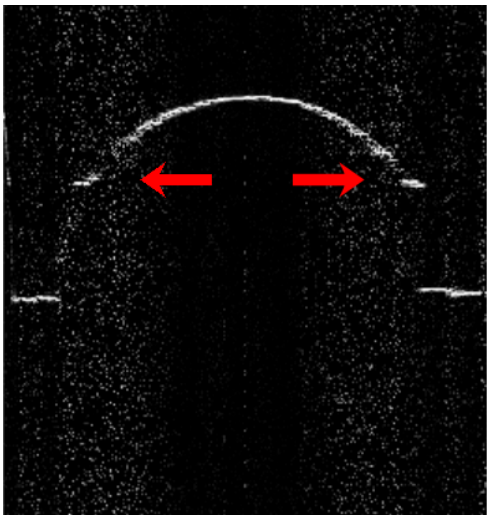

Figure 49: OCT image showing stepping effect along the edge of the clad track as indicated by the red arrows.

in the shape and size of the melt pool created during laser cladding. The results were analyzed to see if the shape of the melt pool can be inferred from areas in the OCT measurements where no or very scarce amount of data points are captured.

Initially, measurements were carried for a laser welding process. Within the welding experiments (section 4.2.1), a large and approximately circular region of unmeasured points is observed. However, points are measured along the x-axis centerline passing through its center. These measurement points extend only up to half the length of the region along the y-axis. To explain why this happens, the aforementioned effect of specular reflections on inclined surfaces is revisited. In such a scenario, this would mean that unmeasured points are due to a smooth and inclined surface in this region.

The approximate width of the unmeasured region is slightly over 1 mm. The elevation of the measured points along the x-axis centerline, as opposed to the surrounding substrate, is at most 0.3 mm. The surface angle, when for simplicity assuming the surface in the region where points are missing is straight,

is close to 31°, as shown in figure 50.

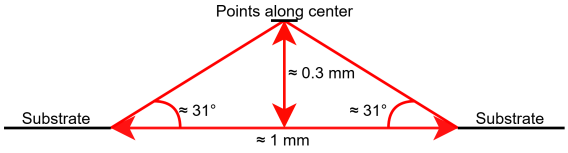

Figure 50: Simplified schematic of surface inclination in laser welding.

This suggests that in a laser welding environment also an inclination is observed in the melt pool. This inclination, although small as compared to the inclinations on the sides of a cladded track, is sufficient to yield a specular reflection to reach beyond the acceptance cone. Thus, resulting in missing points. A simplified schematic overview of a specular reflection reaching beyond the acceptance cone is shown in appendix B, in figure 53. Dependent on the divergence of the OCT beam, surfaces angled at only a few degrees could already yield specular reflections beyond the acceptance cone.

Another possibility of missing points in the point cloud is saturation of the pixels in the line camera. That is, if a specular reflection is yielded from a flat or nearly flat surface. In that case, the entire incident measurement beam is reflected back into the sensor. At the used exposure of the line camera of the OCT, this might result in the saturation of its pixels. This would mean that there are no interference fringes visible as the pixels are saturated. As a result, no height position can be determined. If this were indeed the case, this would result in missing points in the corresponding point cloud as well.

However, the OCT results suggest this is not the case at the used exposure. That is, because there are points measured close the x-axis centerline. These consecutive points are on a almost flat surface, which is seen by the fact that consecutive points along a line have similar height values. These same points are assumed to be in a position where the melt pool is existent. This is reasonable, as it is the position of the center of the processing beam. From this it could be said that measuring an approximately flat and assumed molten surface yields a reflection that does not saturate the camera pixels at the used exposure of the camera. This is because the system still retrieves a height value that is plotted in the point cloud. To determine whether this effect exists at greater exposure times, a mirror providing a surface for a specular reflection could be placed beneath the OCT sensor. By adjusting the exposure, it can then be verified when the pixels of the line camera become saturated.

Then there is the introduction of shielding gas that appears to have a clear impact on the shape of the region of unmeasured points. This region is elongated along the y-direction and resembles the shape of a teardrop. This would be interpreted as an elongated inclined smooth surface. That, on its turn, can be interpreted as an elongated melt pool.

However, the overlay of thermal contour lines (section 4.2.2), immediately pose a contradiction. From just the OCT measurement, the region of unmeasured points is elongated in the y-direction, when shielding gas applied. From the thermal image, the contour lines appear elongated in the y-direction, when no shielding gas is applied. The latter is a phenomenon confirmed by literature as well, where fast cooling right after the location of the melt pool is induced by the trailing shielding gas [57].

It leaves to wonder why the OCT measurements shows a elongated area of unmeasured points when shielding gas is applied, when the thermal images suggest the melt pool is actually shorter in length. From the measurement results at hand, this does not become clear.

Finally, the OCT was used in in-situ experiments in laser cladding (section 4.2.3 and 4.2.4). The OCT results indicate the appearance of different zones that show consistent characteristics across the different cladding experiments. The different zones are identified on the basis of point density. The size of Zone 1 remains approximately the same throughout all experiments with different process parameters. Yet, the point density that is observed differs across experiments. It is observed that lower laser power and a higher scan speed, yield more points measured in Zone 1. Processing at a lower laser power and higher scan speed also yield a less high clad track.

As the width and length of Zone 1 are approximately the same size across experiments but the height varies, it is suggested that the inclination of the surface in Zone 1 is different across experiments. This would explain why there is more points being captured within Zone 1 at higher scan speeds, as the surface

in Zone 1 for these process parameters is less inclined. However, as posed in the results, this does not explain why higher laser powers yield the same effect, as in these experiments no change in height larger than 0.1 mm is observed.

Across experiments, it is seen that the width of the clad track is increasing along the negative y-direction. However, along the approximately circular boundary of Zone 1 more points are measured than within Zone 1. Interestingly, as along this boundary, as visible in the surface reconstruction (section 4.2.6) there is no apparent change of the inclination along this boundary. Thus, the abrupt change in point density, or really the existence of Zone 1, can not be explained by solely considering the effects of different surface inclinations. Add to this that size almost perfectly resembles the size of the processing beam. It is suggested that fewer points are measured in the area where the processing beam is continuously irradiating the melt pool during the process. From just these results it is not clear why this is the case.

It can be seen from just looking at the OCT measurements that the track width, especially at higher laser powers and slower scan speeds, approaches nearly twice the width of Zone 1. Intuitively, this means that Zone 1 is not representative of the melt pool shape. The same is concluded from the thermal overlay (section 4.2.4), as different level contour lines correspond to this zone. This is not caused by process fluctuations. Because, the higher level contour lines are found to be relatively stable (section 4.2.5). Also, from the OCT measurement and the resulting surface reconstruction (section 4.2.6), it becomes apparent that the height of the track is still increasing beyond Zone 1. It is suggested that the increase in height that is observed beyond the boundary of Zone 1 requires the material to be in a molten state. Thereby, the claim that Zone 1 is not the shape of the melt pool is strengthened.

Looking at the points measured in Zone 2, it is seen that most of the points are measured closer to the x-axis centerline of the cladded track. In Zone 2, the actual loss of measurement points occurs going towards the edges of the track. As apparent from the surface geometry of the clad track (section 4.1.1) this is understood because along the x-axis centerline the surface is less inclined than than towards the edges. A similar effect was found in the welding experiments (section 4.2.1). However, when comparing the cladding experiments with the welding experiment, more points are measured farther from the center of the track in the cladding experiments than in the welding experiments. This effect is notable, as the clad track, with its approximately parabolic shape, exhibits greater surface inclination away from its center as opposed to the welding tracks. Thus, the question arises, why are there are still relatively much points measured in Zone 2, away from the center of the track?

A possible explanation for this comes from an effect observed in the study of Syed et al. [58]. In their work, involving a lateral powder supply, it was noted that solid powder particles that are heated during flight but strike the trailing region of the melt pool, so behind the position of continuous laser irradiation, take longer to melt or may not melt fully at all and become embedded in the surface due to the lower temperature in the trailing region of the melt pool. Translating this to the OCT measurement, it suggests that in less hot regions of the melt pool, which are still directly impacted by the powder, more points could be measured. Solid particles in these regions, taking longer to melt or those that have become embedded in the surface, yield diffuse reflections of the OCT probing beam that even at greater surface inclinations are captured by the OCT system. Such a region exists, as the spot size of the processing beam is only 1.2 mm, the inner diameter of the powder nozzle is 1.5 mm, and the powder stream is diverging. This would explain the difference between the cladding and the welding experiments, as no powder was directed at the melt pool in the welding experiments. Following this explanation, it would also clarify the existence of Zone 1, which corresponds to the area where the process beam continuously irradiates, making it the hottest region of the melt pool. As a result, powder particles melt the quickest in this zone. The surface then produces specular reflections, which exceed the numerical aperture of the system.

Now, consider again the thermal images overlaid on the OCT measurement (section 4.2.4). The hypothesis is that if a single value contour line (or isotherm) is found to be at the same position as the boundary of Zone 2, the boundary of Zone 2 could be the boundary the of the melt pool. To confirm this, it must be verified that the contour line represents the liquidus temperature of the material. However, since the thermal camera used is not calibrated, it remains unclear which contour line accurately represents this liquidus temperature. However, in the results it is observed that the transition from the second to the third zone does not correspond to any single contour line across the different experiments. Nevertheless, following the way this result is obtained, it cannot be disregarded either. That is because the OCT takes multiple seconds to complete the measurement and the thermal images fluctuate over the course of this duration.

In previously addressed literature, Kanko et al. have seen a similar transition that was suggested to be indicative of a liquid-solid phase transition [50]. In their findings, this transition was based on a decrease of the signal intensity when crossing this boundary. In this research, the transition is based on the point density of the points in a point cloud. Essentially, they amount to the same effect. In their research, the presumed molten area produces a specular reflection, hence a high intensity is captured. When transitioning across the boundary, they presume a diffuse reflection of a solidified surface causes a decreased intensity. In this research, the presumed molten area also produces a strong reflection, resulting in points plotted along the centerline (width) of the clad track. However, further away from the x-axis centerline of the cladded track, the angled surface makes it that no specular reflection is captured. Then, across the Zone 2 boundary, all points are plotted. Similar to the work of Kanko et al., it is suggested that here reflections with lesser intensity are captured, again due to the effect of a diffuse reflection. Yet, there is a reflection captured, meaning the height can be retrieved. As a result, the point density, across the Zone 2 boundary, is bigger than within Zone 2.

Additionally, the OCT measurements, and specifically the reconstructed surface (section 4.2.6), reveal that the height of the deposit continues to increase until just before the transition from Zone 2 to Zone 3. At this point it appears to reach close to the maximum observed height. This observation suggests that the material in Zone 2 remains in a molten state, as again it is assumed that the height increase requires some degree of fluidity or flow for additional build-up to occur. If the material were fully solidified, no further reshaping or height accumulation would be possible. For the same reason, it was earlier argued that Zone 1 is not a resemblance of the melt pool.

Now, consider again the possibility of a single contour line that corresponds to the Zone 2 boundary. Following the results (section 4.2.4), this could e.g. be the contour line with value 0.08 - 0.13. If such a contour line was indeed confirmed to represent the liquidus temperature, following it toward the leading edge ($+y$-direction) reveals that it extends wider than the width of the deposit width. This suggests that, at the leading edge, the heat distribution may be causing the substrate surrounding the deposit to reach temperatures at the liquidus temperature. This would suggest that there is region of molten substrate material immediately adjacent to the clad deposit. If there were indeed a region adjacent to the deposit that is in a molten state, this could also be visible in the OCT measurement. Yet it appears there is no change in the density of points measured. It suggests that this area is flat, and following the retrieved height values in this region, this indeed appears to be the case.

Up to this point, the discussion has treated the melt pool boundary as a distinct transition. However, knowledge of the solidification process indicates that there is actually a temperature range between the liquidus (where the material is entirely liquid) and solidus (where the material is entirely solid), encompassing what is known as the mushy zone [59]. This mushy zone is expected to exist within the OCT measurements, reflecting a gradual transition of the density of points being measured rather than a sharp boundary. Yet if this zone is really small, it might not be distinctly observable at all. For the substrate material (S316L) this temperature difference between the solidus and the liquidus is 25 °C, whereas for the powder (Micro-Melt 23) it is not specified. To be able to see how the mushy zone is represented into the OCT measurement, again the calibration of the thermal camera is a necessity.

Limitations

While the OCT applied in a laser cladding (and laser welding) context during processing provides a unique insight in the development of the deposit, the research does have limitations that warrant further analysis to further explore the revealed phenomena.

Again considering the work of Kanko et al., [50] a very distinct limitation in this research becomes clear. That is, upon only considering the point cloud, the information of with which intensity this point was captured, or with what SNR, is lost. This is a limitation, because the SNR per point captured reveals the boundary from a liquid to solid phase transition more clearly then the density of the points captured. To understand, consider a scenario where there is perfectly flat melt pool and besides there is solidified flat surface, yet with a certain roughness. If the OCT measures both surfaces, the SNR ratio will differ. It will be higher in the case of the molten surface due to its specular reflection and lower in the case of the solidified surface because of its diffuse reflection. Yet one has to consider the point clouds of both surfaces, there would be no difference at all. That is because in both cases light returns to the sensor. When only considering point clouds, the transition from a liquid to solid phase is merely visible due to the surface geometry of the clad. While, if you were to consider the difference in SNR for the points that are captured, the boundary would be visible as well.

The need for a calibrated thermal camera is crucial in determining the temperature distribution and ultimately the two-dimensional shape of the melt pool. Besides that, averaging the thermal captures could potentially help in obtaining a more realistic fit between the OCT measurement and the thermal images. Yet, simply averaging all the frames over the measurement duration is not a guarantee of it being more realistic. Rather, thermal captures that were made in at the start should be more pronounced in the top of this image and captures made almost at the end of OCT measurement should be more pronounced in the end. This is best understood considering that when the OCT measurement completes, after roughly three seconds, the camera has shot (using a frame rate of 60 fps) 180 frames. Within the duration that the camera captures its first frame, the OCT measures 1/180 of the total measurement points, with using the lateral resolutions applied equals 1250 points. For the best possible overlay of a thermal image on the OCT measurement, the pixels in the image spanning the same area as the 1250 points measured with the OCT should be resembled by the first frame captured, and so on.

A parameter that could improve the OCT measurement, yet is not addressed throughout this research, is the exposure time of the line camera in the spectrometer. This was initially set to 2 µs. Increasing it is expected to have an effect on the SNR in the frequency spectrum, but this would come at the cost of longer measurement durations. However, it would have been interesting to observe the effect of an increased exposure time on the measurement results. Experiments with angled substrates showed that even at a 75° angle, the SNR remained above 18 dB (section 3.2.5), which suggests that the exposure is sufficiently long. Additionally, increasing the SNR would not address the broadening of the peak observed on angled surfaces. Therefore, adjusting the exposure time would only be beneficial if the SNR were so low that it became challenging to distinguish the signal from noise. Yet, this is apparently not the case. As mentioned earlier, the possibility of saturation of the pixels of the line camera should be investigated.

6 Conclusions and Recommendations

The research began by developing a strategy for measurement and analysis, followed by carrying out experiments aimed to induce variations in the dimensions of the cladded track and the shape and size of the melt pool. This was done by varying the laser power and scan speed of the robot. Both ex-situ and in-situ measurement results were used to classify the performance of the OCT system in the laser cladding environment. Then, results from the in-situ measurements were again used to determine the effectiveness of the OCT in capturing the characteristics of the melt pool. In terms of the research questions, the main conclusions are as follows:

1. *Given that the OCT sensor is integrated into the laser cladding environment, what is the optimal strategy for measurement and analysis to characterize the system?*

In general, the strategy involved classifying the behavior of the OCT system when measuring clad tracks both ex-situ, after they have been laid down and (in-situ) during the actual cladding process. This comparative approach proved valuable, as it provided a baseline representation of a clad track measured using the OCT and highlights the changes introduced in the OCT measurement by the in-situ conditions, specifically, the presence of a melt pool.

The basis for all the experiments were the OCT measurements made using a raster scan, in order to obtain a point cloud. Whereafter outlier removal, using dedicated python libraries such as Open3D, is implemented to filter out points that are captured as noise.

Ex-situ OCT measurements are compared with confocal microscopy to determine the accuracy of the points captured. RMSE values were calculated along partitioned sections of the point cloud as to obtain an indication of where the highest inaccuracies along a cladded track are found. The strategy further incorporated thermal imaging as a reference for the in-situ OCT measurements. The (non-calibrated) isotherms obtained from the thermal captures were overlaid on the OCT measurements to determine if the boundaries in the OCT data, indicative of transitions between so called different zones, correspond to specific isotherms. By comparing these overlaid plots for the range of process parameters, it could then be confirmed whether or not a similar isotherm consistently represents the same transitional region. Such observation suggests that a transition could lie either on the liquidus or on the solidus isotherm. However, due to fluctuations in the thermal captures and the inherent nature of OCT measurement, achieving a perfect match with the current method of overlaying isotherms on the OCT data was not possible.

The approach for the in-situ measurements was to start with a simpler process involving only the laser, where essentially conductive laser welding was achieved. This proved useful for identifying influencing factors without having to consider effects that solely arise due to the cladding process. Thereafter, in-situ measurements were performed in a laser cladding environment.

Later on, video analysis, of the video's from the thermal camera, was used to capture the process fluctuations. Thereafter, surface reconstruction using interpolation methods was used to approximate the height at positions where the OCT measurement was not possible.

2. *How is the performance of the OCT system characterized in a laser cladding environment when process parameters are varied, leading to changes in clad track dimensions?*

Overall, it was found that the surface geometry of the cladded tracks (ex-situ) is well measurable. However, the comparison with confocal microscopy showed that accuracy of the measurements is negatively affected on the edges of a cladded track. It was found that this is due to effects caused by a changing surface inclination and the relatively large spot size of the OCT measurement beam. This resulted in points that show increased RMSE values as compared to confocal microscopy, or loss of points at all. However, the benchmarking that was performed and the resulting RMSE values did not directly represent or correspond with the process parameters used. This is because the measurements are based on the start section of the clad track. Thereby focusing on the changing width, height and aspect ratio captured during the start-up phase of cladding, rather than a more stable portion of the clad track further on the track.

The effects of the shielding gas and the intersecting powder stream were studied. It was found that the intersecting powder stream showed no significant difference in the OCT measurement, yet it contributed to slight decrease in overall intensity captured with the thermal camera. Next, the use of shielding gas was found to extend the region of points not measured using the OCT, resulting in a teardrop shape.

The OCT measurement result hints towards the elongation of the melt pool when shielding gas applied (in a conductive laser welding environment), yet the thermal images contradicted this.

In-situ experiments in a laser cladding environment revealed three distinct zones on the basis of point density. The effect of specular reflections of the OCT measurement beam is suggested to be the cause of the existence of the different zones. Zone 1 was found to remain in a similar shape and consistent size for the range of process parameters used. This shape and size was found to neatly correspond with the spot size of the processing beam used. Zone 2 was found to increase in length and width, with increasing laser power and decreasing scan speed. Zone 3 was found to appear directly behind Zone 2, yet the boundary was found to be less distinguishable at a lower laser power and higher scan speed. Also, the same effect was seen for the boundary between Zone 1 and Zone 2.

3. How effective is the OCT sensor in capturing the geometric characteristics of the melt pool formed during laser cladding?

The appearance of distinguishable zones in the in-situ measurements, especially Zone 2, suggests that the OCT is capable of capturing the boundary of the melt pool, based on a difference in point density. Yet, this cannot be confirmed as this requires the location of the isotherms (solidus and liquidus). If the boundary is found to correspond with these isotherms, the difference in point density would be explained by diffuse and specular reflections on an angled surface attributed to a change in surface roughness. As it is suggested that the OCT is able to capture points on an inclined solidified surface, that yields a diffuse reflection. Whereas the OCT is unable to capture points on an inclined molten surface, that yields a specular reflection.

In the current way of using the OCT measurement, the presumed boundary of the melt pool is only visible as a difference in point density in the point cloud. Yet, following the effect of diffuse and specular reflections, the OCT would also be able to see this boundary on the basis of the intensity of the reflection that is captured. However, when only considering point cloud data structures, this information is lost. For the OCT to effectively capture the boundary of the melt pool, this information should be combined. Where the surface is inclined, the boundary exists due to a difference in point density. Where the surface is nearly flat, the boundary exists due to a difference in intensity of the reflection, or SNR, that is captured.

The OCT offers a unique insight that current monitoring or control strategies, such as via a thermal camera, cannot provide. With proper calibration, capturing the melt pool could extend beyond a thermal 2-dimensional perspective to now encompass a 3-dimensional geometry. As the OCT measures fast and is able to do so whilst processing, the system shows great potential to help control the laser cladding process either through controlling the size of the different zones, or maintaining specific clad track widths and heights during processing. This, in turn, would allow for influence over the final properties of the clad track.

Recommendations

The OCT system could benefit from an analysis strategy that incorporates both the points captured in the point cloud as well as the SNR of the points that are captured. Right now, this combined approach has not been utilized but this would prove to be useful as per the considerations posed earlier.

Also, the entire laser cladding setup could benefit from integrating the OCT system into the existing fieldbus (DeviceNet / Profinet) network, which already connects the laser, robot, powder feeder, and thermal camera. This integration would simplify linking the section of the clad track corresponding to the OCT measurement to the correct thermal images such that they accurately align with the OCT's measurement window.

Then, this research has focused exclusively on single track deposits, while practical laser cladding applications always involve more than just single track deposits. Understanding the behavior of the OCT in-situ with greater clarity would make it interesting to investigate how the OCT measurement changes in consecutive tracks or when tracks are stacked on top of one another.

References

[1] W. Grzesik, "Machinability of engineering materials," in *Advanced Machining Processes of Metallic Materials (Second Edition)*, second edition ed., W. Grzesik, Ed. Elsevier, 2017, pp. 241–264. [Online]. Available: https://www.sciencedirect.com/science/article/pii/B9780444637116000132

[2] B. Fotovvati, N. Namdari, and A. Dehghanghadikolaei, "On coating techniques for surface protection: A review," vol. 3, 03 2019.

[3] S. Nowotny, L.-M. Berger, and J. Spatzier, "1.18 - coatings by laser cladding," in *Comprehensive Hard Materials*, V. K. Sarin, Ed. Oxford: Elsevier, 2014, pp. 507–525. [Online]. Available: https://www.sciencedirect.com/science/article/pii/B9780080965277000180

[4] D. S. Gnanamuthu, "Cladding," no. US3952180A, 12 1974. [Online]. Available: https://patents.google.com/patent/US3952180A/en

[5] G. M. Eboo and A. G. Blake, "Laser cladding of gas turbine components," in *Proceedings of the International Gas Turbine Conference and Exhibit.* Quantum Laser Corp., 06 1986, presented at the International Gas Turbine Conference and Exhibit.

[6] T. Morgado and C. Valente, "Development status of laser cladding and the new metallic alloys," 05 2018.

[7] J. T. Hofman, "Development of an observation and control system for industrial laser cladding," Ph.D. dissertation, Enschede, 2009.

[8] V. M. Weerasinghe and W. M. Steen, *Laser Cladding with Pneumatic Powder Delivery.* Dordrecht: Springer Netherlands, 1987, pp. 183–211.

[9] M. Schneider, "Laser cladding with powder," Ph.D. Thesis, University of Twente, Enschede, The Netherlands, 1998.

[10] J. Mazumder and J. Singh, "Laser surface alloying and cladding for corrosion and wear," *High Temperature Materials and Processes*, vol. 7, no. 2-3, pp. 101–106, 1986.

[11] D. Bartkowski, A. Bartkowska, and P. Jurči, "Laser cladding process of fe/wc metal matrix composite coatings on low carbon steel using yb: Yag disk laser," *Optics Laser Technology*, vol. 136, 2021. [Online]. Available: https://www.sciencedirect.com/science/article/pii/S0030399220314171

[12] J. del Val, R. Comesaña, F. Lusquiños, M. Boutinguiza, A. Riveiro, F. Quintero, and J. Pou, "Laser cladding of co-based superalloy coatings: Comparative study between nd:yag laser and fibre laser," *Surface and Coatings Technology*, vol. 204, no. 12, pp. 1957–1961, 2010. [Online]. Available: https://www.sciencedirect.com/science/article/pii/S0257897209009864

[13] A. Lamikiz, I. Tabernero, E. Ukar, S. Martínez, and L. Lacalle, "Current designs of coaxial nozzles for laser cladding," *Recent Patents on Mechanical Engineering*, vol. 4, pp. 29–36, 03 2011.

[14] C. Leyens and E. Beyer, "8 - innovations in laser cladding and direct laser metal deposition," in *Laser Surface Engineering*, ser. Woodhead Publishing Series in Electronic and Optical Materials, J. Lawrence and D. Waugh, Eds. Woodhead Publishing, 2015, pp. 181–192. [Online]. Available: https://www.sciencedirect.com/science/article/pii/B9781782420743000088

[15] K. Partes and G. Sepold, "Modulation of power density distribution in time and space for high speed laser cladding," *Journal of Materials Processing Technology*, vol. 195, no. 1, pp. 27–33, 2008. [Online]. Available: https://www.sciencedirect.com/science/article/pii/S0924013607005869

[16] M. Tavish Nanda, F. Michelle C. Liang, MD, and F. Jay S. Duker, MD. (2021) Optical coherence tomography. Milestone essay published in "Milestones in Retina". [Online]. Available: https://retinahistory.asrs.org/milestones-developments/history-of-oct

[17] M. L. Gabriele, G. Wollstein, H. Ishikawa, L. Kagemann, J. Xu, L. S. Folio, and J. S. Schuman, "Optical Coherence Tomography: History, Current Status, and Laboratory Work," *Investigative Ophthalmology Visual Science*, vol. 52, no. 5, pp. 2425–2436, 04 2011.

[18] J. F. de Boer, R. Leitgeb, and M. Wojtkowski, "Twenty-five years of optical coherence tomography: the paradigm shift in sensitivity and speed provided by fourier domain oct," *Biomed. Opt. Express*, vol. 8, no. 7, pp. 3248–3280, 07 2017.

[19] A. Fercher, C. Hitzenberger, G. Kamp, and S. El-Zaiat, "Measurement of intraocular distances by backscattering spectral interferometry," *Optics Communications*, vol. 117, no. 1, pp. 43–48, 1995. [Online]. Available: https://www.sciencedirect.com/science/article/pii/0030401895001195

[20] S. R. Chinn, E. A. Swanson, and J. G. Fujimoto, "Optical coherence tomography using a frequency-tunable optical source," *Opt. Lett.*, vol. 22, no. 5, pp. 340–342, 03 1997. [Online]. Available: https://opg.optica.org/ol/abstract.cfm?URI=ol-22-5-340

[21] S. Sadek and R. Hatata, "Oct from the past to the future," in *Optical Coherence Tomography*, G. L. Giudice and I. Gattazzo, Eds. Rijeka: IntechOpen, 2023, ch. 2.

[22] N. Deyneka Dupriez and A. Denkl, "Advances of oct technology for laser beam processing: Precision and quality during laser welding," *Laser Technik Journal*, vol. 14, pp. 34–38, 09 2017.

[23] Y. Lee, M. Nordin, S. Babu, and D. F. Farson, "Effect of fluid convection on dendrite arm spacing in laser deposition," *Metallurgical and Materials Transactions B*, 03 2014.

[24] M. Mazzarisi, A. Angelastro, M. Latte, T. Colucci, F. Palano, and S. L. Campanelli, "Thermal monitoring of laser metal deposition strategies using infrared thermography," *Journal of Manufacturing Processes*, vol. 85, pp. 594–611, 2023. [Online]. Available: https://www.sciencedirect.com/science/article/pii/S1526612522008507

[25] F. Wirth, S. Arpagaus, and K. Wegener, "Analysis of melt pool dynamics in laser cladding and direct metal deposition by automated high-speed camera image evaluation," *Additive Manufacturing*, vol. 21, pp. 369–382, 2018. [Online]. Available: https://www.sciencedirect.com/science/article/pii/S2214860418300551

[26] N. Ahmed, "Direct metal fabrication in rapid prototyping: A review," *Journal of Manufacturing Processes*, vol. 42, pp. 167–191, 05 2019.

[27] E. Toyserkani, A. Khajepour, and S. F. Corbin, *Laser Cladding*, 1st ed. CRC Press, 2004.

[28] R. Qin, X. Zhang, S. Guo, B. Sun, S. Tang, and W. Li, "Laser cladding of high co–ni secondary hardening steel on 18cr2ni4wa steel," *Surface and Coatings Technology*, vol. 285, pp. 242–248, 2016. [Online]. Available: https://www.sciencedirect.com/science/article/pii/S0257897215304060

[29] W. Ya, J. F. Hernández-Sánchez, B. Pathiraj, and A. Huis in 't Veld, "A study on attenuation of a nd:yag laser power by co-axial and off-axial nozzle powder stream during cladding," *International Congress on Applications of Lasers Electro-Optics*, pp. 453–462, 01 2013. [Online]. Available: https://www.researchgate.net/publication/328321829_A_study_on_attenuation_of_a_NdYAG_laser_power_by_co-axial_and_off-axial_nozzle_powder_stream_during_cladding

[30] W. Steen and J. Mazumder, *Laser Material Processing*, 4th ed. Springer London, 2010.

[31] G. Abbas and D. West, "Laser surface cladding of stellite and stellite-sic composite deposits for enhanced hardness and wear," vol. 143, no. 2, pp. 353–363, 1991. [Online]. Available: https://www.sciencedirect.com/science/article/pii/0043164891901065

[32] U. de Oliveira, V. Ocelík, and J. De Hosson, "Analysis of coaxial laser cladding processing conditions," *Surface and Coatings Technology*, vol. 197, no. 2, pp. 127–136, 2005. [Online]. Available: https://www.sciencedirect.com/science/article/pii/S0257897204004803

[33] M. Erfanmanesh, H. Abdollah-Pour, H. Mohammadian-Semnani, and R. Shoja-Razavi, "An empirical-statistical model for laser cladding of wc-12co powder on aisi 321 stainless steel," *Optics Laser Technology*, vol. 97, pp. 180–186, 2017. [Online]. Available: https://www.sciencedirect.com/science/article/pii/S0030399217304279

[34] G. C. Onwubolu, J. Davim, C. Oliveira, and A. Cardoso, "Prediction of clad angle in laser cladding by powder using response surface methodology and scatter search," *Optics Laser Technology*, vol. 39, no. 6, pp. 1130–1134, 2007. [Online]. Available: https://www.sciencedirect.com/science/article/pii/S0030399206001824

[35] M. Prasad Behera, M. Gopinath, and A. Kumar Nath, "A study on geometrical aspects in laser cladding by lateral powder injection technique," *Materials Today: Proceedings*, 2023. [Online]. Available: https://www.sciencedirect.com/science/article/pii/S2214785323008155

[36] M. Xiao, F. Jiang, C. Guo, H. Song, and T. Dong, "Investigation on microstructure and mechanical properties of fe-based amorphous coatings prepared via laser cladding assisted with ultrasonic vibration," *Optics Laser Technology*, vol. 162, 2023. [Online]. Available: https://www.sciencedirect.com/science/article/pii/S0030399223001871

[37] B. Song, T. Yu, X. Jiang, W. Xi, and X. Lin, "Development mechanism and solidification morphology of molten pool generated by laser cladding," *International Journal of Thermal Sciences*, vol. 159, 2021. [Online]. Available: https://www.sciencedirect.com/science/article/pii/S1290072920310310

[38] L. Bremer, M. Luckabauer, and G. R. B. E. Römer, "Laser intensity profile as a means to steer microstructure of deposited tracks in directed energy deposition," *Materials Design*, vol. 227, 2023. [Online]. Available: https://www.sciencedirect.com/science/article/pii/S0264127523001405

[39] S. Aumann, S. Donner, J. Fischer, and F. Müller, "Chapter 3: Optical coherence tomography (oct): Principle and technical realization," in *High Resolution Imaging in Microscopy and Ophthalmology*, J. F. Bille, Ed. University Heidelberg, 2019.

[40] J. Kalkman, "Fourier-domain optical coherence tomography signal analysis and numerical modeling," *International Journal of Optics*, vol. 2017, 2017. [Online]. Available: https://onlinelibrary.wiley.com/doi/abs/10.1155/2017/9586067

[41] M. Ali and R. Parlapalli, "Signal processing overview of optical coherence tomography systems for medical imaging," *Texas Instrum.*, 2010.

[42] A. F. Fercher, W. Drexler, C. K. Hitzenberger, and T. Lasser, "Optical coherence tomography - principles and applications," *Reports on Progress in Physics*, vol. 66, no. 2, 2003. [Online]. Available: https://dx.doi.org/10.1088/0034-4885/66/2/204

[43] Obel, Optical + Biomedical Engineering Laboratory, "Introduction to oct," University of Western Australia, accessed [6-03-2024]. [Online]. Available: [https://obel.ee.uwa.edu.au/research/fundamentals/introduction-oct/]

[44] J. A. Izatt, M. A. Choma, and A.-H. Dhalla, "Theory of optical coherence tomography," in *Optical Coherence Tomography, Technology and Applications*, 2nd ed., W. Drexler and J. G. Fujimoto, Eds. Springer Reference, 2019, vol. 1, ch. 2.

[45] D. Zhu, M. Shen, H. Jiang, M. Li, M. Wang, Y. Wang, L. Ge, J. Qu, and J. Wang, "Broadband superluminescent diode-based ultrahigh resolution optical coherence tomography for ophthalmic imaging," *Journal of biomedical optics*, vol. 16, p. 126006, 12 2011.

[46] T. Bautze and M. Kogel-Hollacher, "Keyhole depth is just a distance: The idm sensor improves laser welding processes," *Laser Technik Journal*, 2014.

[47] M. Sokolov, P. Franciosa, T. Sun, V. Dimatteo, A. Ascari, A. Fortunato, and F. Nagel, "Applying optical coherence tomography for weld depth monitoring in remote laser welding of automotive battery tab connectors," *Journal of Laser Applications*, vol. 33, 12 2020.

[48] T. Will, J. Müller, R. Müller, and et al., "Prediction of electrical resistance of laser-welded copper pin-pairs with surface topographical information from inline post-process observation by optical coherence tomography," *Int J Adv Manuf Technol*, vol. 125, pp. 1955–1963, 2023.

[49] G. Xie, S. Wang, Y. Zhang, B. Hu, Y. Fu, Q. Yu, and Y. Li, "An efficient method for laser welding depth determination using optical coherence tomography," *Sensors*, vol. 20, no. 19, 2020.

[50] J. A. Kanko, A. P. Sibley, and J. M. Fraser, "In situ morphology-based defect detection of selective laser melting through inline coherent imaging," *Journal of Materials Processing Technology*, vol. 231, pp. 488–500, 2016. [Online]. Available: https://www.sciencedirect.com/science/article/pii/S0924013615302387

[51] T. G. Fleming, S. G. Nestor, T. R. Allen, M. A. Boukhaled, N. J. Smith, and J. M. Fraser, "Tracking and controlling the morphology evolution of 3d powder-bed fusion in situ using inline coherent imaging," *Additive Manufacturing*, vol. 32, p. 100978, 2020. [Online]. Available: https://www.sciencedirect.com/science/article/pii/S2214860419307171

[52] P. J. DePond, G. Guss, S. Ly, N. P. Calta, D. Deane, S. Khairallah, and M. J. Matthews, "In situ measurements of layer roughness during laser powder bed fusion additive manufacturing using

low coherence scanning interferometry," *Materials Design*, vol. 154, pp. 347–359, 2018. [Online]. Available: https://www.sciencedirect.com/science/article/pii/S0264127518304350

[53] C. Stehmar, M. Gipperich, K.-H. Markus, A. Velazquez Iturbide, and R. Schmitt, "Inline optical coherence tomography for multidirectional process monitoring in a coaxial lmd-w process," *Applied Sciences*, vol. 12, 03 2022.

[54] L. Lasertechnik, "System Manual: OCT for TRUMPF BEO D70 Welding Optics," Munich, 05 2022.

[55] Open3D, "Point cloud outlier removal," 2020, accessed: 2024-05-01. [Online]. Available: https://www.open3d.org/docs/0.12.0/tutorial/geometry/pointcloud_outlier_removal.html

[56] A. D. Elliott, "Confocal microscopy: Principles and modern practices," *Current Protocols in Cytometry*, vol. 92, 03 2020.

[57] S. Bannour, K. Abderrazak, H. Mhiri, and G. Le Palec, "Effects of temperature-dependent material properties and shielding gas on molten pool formation during continuous laser welding of az91 magnesium alloy," *Optics Laser Technology*, vol. 44, no. 8, pp. 2459–2468, 2012. [Online]. Available: https://www.sciencedirect.com/science/article/pii/S003039921200148X

[58] W. U. H. Syed, A. J. Pinkerton, and L. Li, "A comparative study of wire feeding and powder feeding in direct diode laser deposition for rapid prototyping," *Applied Surface Science*, vol. 247, no. 1, pp. 268–276, 2005, proceedings of the European Materials Research Society 2004 - Symposium N. [Online]. Available: https://www.sciencedirect.com/science/article/pii/S0169433205001777

[59] L. Liu, Y. Lin, L. Peng, X. Kang, and X. Wang, "Progress in microstructure design and control of high-hardness fe-based alloy coatings via laser cladding," *Coatings*, vol. 14, no. 11, 2024. [Online]. Available: https://www.mdpi.com/2079-6412/14/11/1351

Appendices

A

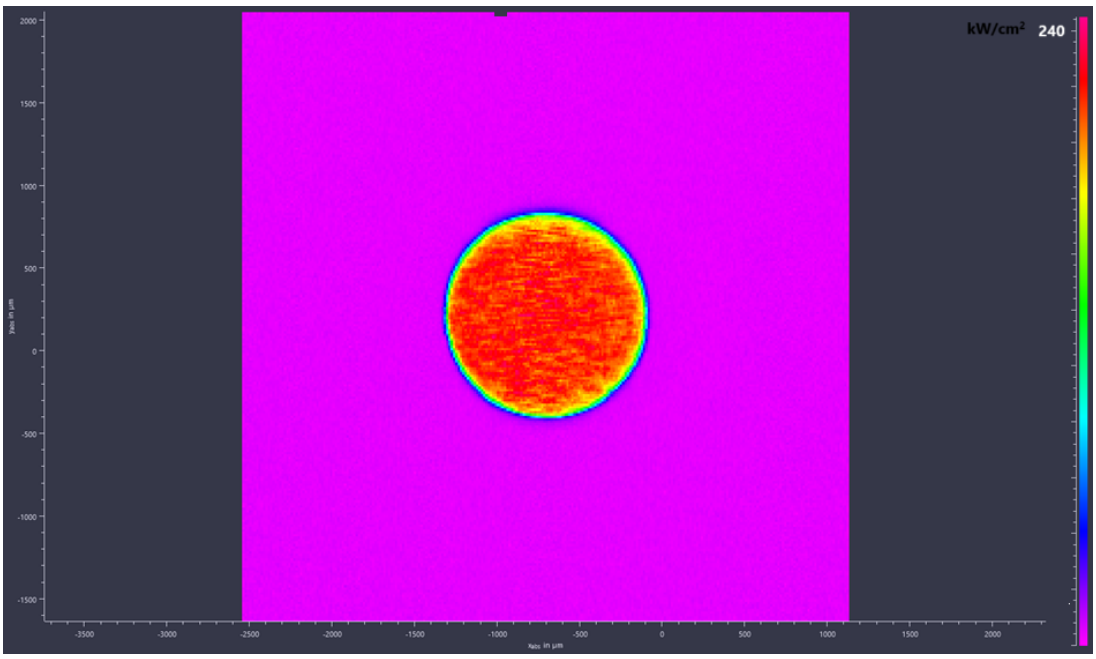

Figure 51: Intensity distribution of processing beam in its focus plane.

	Rot. mom., a	Rot. mom., b
Beam waist position z_0 in mm	60.03	60.99
Beam waist radius w_0 in µm	602.99	603.99
Rayleigh length z_R in mm	13.14	13.39
Divergence angle θ in mrad	91.80	90.21
Beam quality factor M^2	84.42	83.09
BPP in mm*mrad	27.68	27.24
Ellipticity at z_0	1.00	1.00
Astigmatic difference $\Delta z_0/z_R$	0.07	0.07
Misalignment in zx-plane in mrad	-21.44	-21.44
Misalignment in zy-plane in mrad	-4.92	-4.92
Beam direction in mrad	22.00	22.00

Figure 52: Screenshot of full beam profiling measurement.

B

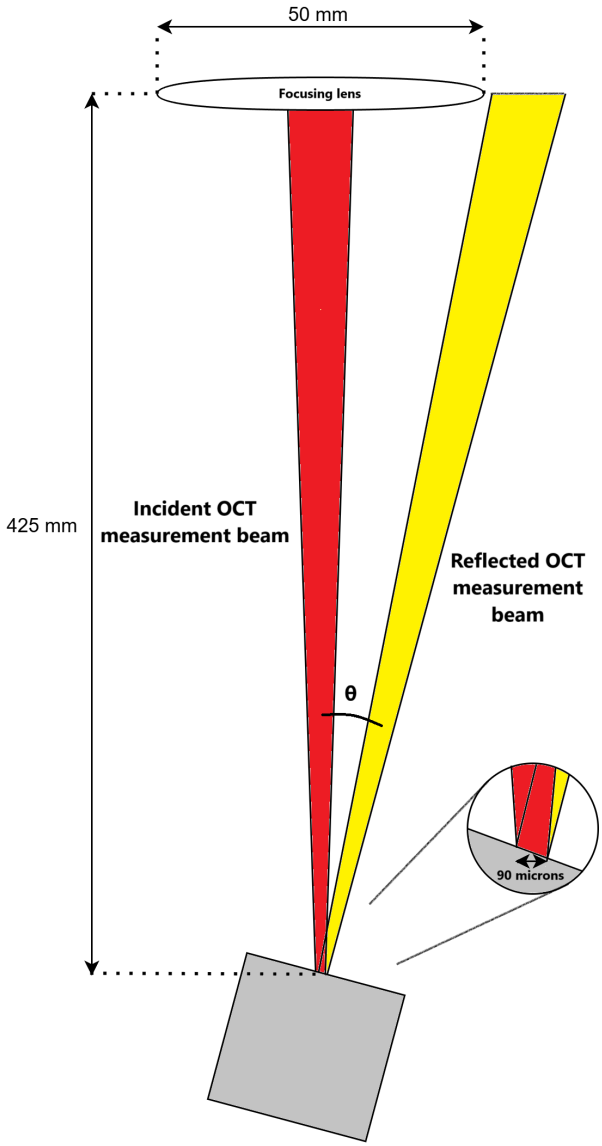

Figure 53: Simplified schematic overview of a specularly reflected OCT measurement beam.